Gas Sensing at Low Temperatures with Different Semiconducting Materials

Dissertation

der Mathematisch-Naturwissenschaftlichen Fakultät

der Eberhard Karls Universität Tübingen

zur Erlangung des Grades eines

Doktors der Naturwissenschaften

(Dr. rer. nat.)

vorgelegt von

Frau Tamara Maria Ruß

aus Breisach am Rhein

Tübingen

2023

Gedruckt mit Genehmigung der Mathematisch-Naturwissenschaftlichen Fakultät der Eberhard Karls Universität Tübingen.

Datum der mündlichen Qualifikation:	23.11.2023
Dekan:	Prof. Dr. Thilo Stehle
1. Berichterstatter/-in:	Prof. Dr. Udo Weimar
2. Berichterstatter/-in:	Prof. Dr. Reinhold Fink

Declaration of Originality

Hereby, I confirm that the submitted doctoral thesis

- Was written by me
- Was written using only the references mentioned where appropriate
- Was not examined before nor has it been published

I also confirm that the electronic and printed versions are identical in content and format.

Place, Date Signature

Acknowledgements

The biggest ‘Thank You’ has to go to my bosses during my time as a doctoral student, Prof. Udo Weimar and Dr. Nicolae Barsan. I appreciate every single opportunity you have given me to grow, both professionally and personally. I will keep the discussions and my time in your group in good memory.

A big ‘Thank you’ also to all my co-workers. Without you guys, I never would have made it. You have always listened to my complaints, whether they were rightful or not. Also, the afterwork beers (always after 5 pm, Nicolae) improved quite a few of my days. Thank you to all of you. A special ‘Thank you’ has to go to Anna who I blame for me ending up in the Weimar/Barsan group. Not only would I probably never have ended up in that group, but I also probably never would have even attempted to get a PhD. We have also had tons of fun times outside the office, although the 48 km hike to Schloss Lichtenstein was probably one of the craziest ones. But how else could we have managed to get 60,000 steps in one day? Also, a huge ‘Thank you’ to Arne, Ugur and Matthias who were quite often pulled into the crazy things Anna and I planned without complaining (too much). I will certainly miss the board game afternoons/evenings with or without a BBQ in my little backyard. I’ve certainly made some great memories with you guys. Also, Arne, thanks for getting me hooked on biking. Makes life just a tiny bit better :)

A massive ‘Thanks’ goes out to all my volleyball team members over the years. You have kept me sane during my PhD! You guys always helped me clear my head whenever I needed it. Much appreciated!

Mom and Dad were always supportive while making sure that I had everything I needed in order to be successful. You have had my back and continue to be my safety net. I cannot put into words how much I appreciate that. But I’m also very grateful for my siblings and their families who were always ready to get my mind off of things. I’m very grateful for my brother’s remodeling work spanning most of my PhD. The tear-down especially was a lot of fun and always an excellent way to work some of the tensions out. Love you all to bits and pieces!

Abstract

Since the late 1960s, chemo-resistive gas sensors have been getting a lot of attention. The materials used for this type of gas sensors have some inherent advantages like their low cost, as well as the ease of manufacture and miniaturization. These sensors, however, also have some inherent drawbacks. These include a lack of selectivity and high power consumption since they are constantly heated to temperatures between 200 and 500 °C. In this Thesis, two different classes of materials were investigated for the use in chemo-resistive gas sensors operated at temperatures below 100 °C. First, with the help of supercritical fluid reactive deposition, WO_3 nanoparticles were surface loaded with metallic Pt clusters. Most publications of Pt or Pd-loaded semiconducting metal oxide materials reported the presence of oxidized noble metal clusters and found a Fermi level pinning mechanism. In this Thesis, experimental proof was found that SFRD results in metallic Pt clusters and a spillover sensing mechanism. The second investigated class of materials for their gas sensing properties below 100 °C were semiconducting metal sulfides. The amount of research on this class of materials for gas sensors is relatively low and when this work was started, there were no publications with experimental proof for sensing mechanisms to any gas. In this Thesis, PbS colloidal quantum dots and Bi_2S_3 nanorods were investigated for their gas sensing properties. The sensing mechanisms to NO_2 for both materials were revealed. For Bi_2S_3, the sensing mechanism to O_3 was investigated as well, in addition to the interference of O_3 with the sensing mechanism to NO_2. It was found that the investigated metal sulfides in this Thesis react selectively with oxidizing gases. For PbS, it was additionally found that the presence of organic ligands used to stabilize the colloidal quantum dots have a significant effect on the stability of the sensor as well as the sensing mechanism to NO_2. It was revealed that NO_2 reacted with the residual organic ligand which resulted in the formation of an insulating organic shell around the CQDs as well as an initial boost of the sensing response due to a byproduct formed during the decomposition reaction of the organic ligand. For Bi_2S_3, it was found that the sensing mechanism with NO_2 changed in dependence on the present concentration. While low NO_2 concentrations resulted in healing of sulfur vacancies, higher concentrations resulted in the formation of nitrates.

Zusammenfassung

Seit den späten 1960ern bekommen chemo-resistive Gassensoren viel Aufmerksam. Die Materialien, die für diese Art von Sensoren verwendet werden, haben einige inhärente Vorteile wie einen geringen Preis, sowie die einfache Verarbeitung und Miniaturisierung. Allerdings haben sie auch inhärente Nachteile, wie zum Beispiel die Selektivität und relativ hohe Stromverbräuche, da die Sensoren konstant auf Temperaturen zwischen 200 und 500 °C beheizt werden. In dieser Thesis wurden zwei verschiedene Materialklassen für chemo-resistive Gassensoren, betrieben bei unter 100 °C, untersucht. Zunächst wurden mit Hilfe der Überkritischen Reaktivabscheidung WO_3 Nanopartikel mit metallischen Pt-Clustern beladen. Die meisten Publikationen, die Pt- oder Pd-beladenes WO_3 behandeln, berichten von oxidierten Edelmetall-Clustern und dem Fermi-level pinning Mechanismus. Im Rahmen dieser Thesis wurde experimentell bewiesen, dass metallische Pt-Cluster in einem Spillover-Mechanismus resultieren. Die zweite Materialklasse, die auf ihre Gassensoreigenschaften bei unter 100 °C untersucht wurden, waren halbleitende Metallsulfide. Die verfügbare Menge an Literatur für diese Materialklasse ist vergleichsweise gering und zu Beginn der hier präsentierten Thesis gab es keine Publikationen mit experimentellen Beweisen für Detektionsmechanismen. Im Rahmen dieser Thesis wurden kolloidale PbS Quantenpunkte und Bi_2S_3 Nanostäbchen auf ihre Gassensoreigenschaften untersucht. Der NO_2-Detektionsmechanismus wurde für beide Materialien aufgedeckt. Für Bi_2S_3 wurde zudem der O_3-Detektionsmechanismus und die daraus resultierende Interferenz mit der NO_2-Detektion untersucht. Beide Metallsulfide reagierten selektiv auf oxidierende Gase. Mit PbS wurde zudem entdeckt, dass der organische Ligand, der zur Stabilisierung der Quantenpunkte verwendet wurde, erheblichen Einfluss auf sowohl die Sensorstabilität als auch den NO_2 Detektions-mechanismus hat. NO_2 reagierte mit dem organischen Liganden, was sowohl in der Bildung einer isolierenden Schicht um die halbleitenden Quantenpunkte resultierte als auch in einer Verstärkung des Sensorsignals aufgrund eines gebildeten Nebenprodukts der Reaktion. Bei Bi_2S_3 wurde entdeckt, dass der NO_2-Detektionsmechanismus sich mit zunehmender NO_2-Konzentration verändert. Während bei niedrigen Konzentration Schwefel-Leerstellen geheilt werden, bilden sich bei höheren Konzentrationen Nitrate.

Table of Contents

List of Abbreviations

A	Absorbance
CPD	Contact Potential Difference
CQD	Colloidal Quantum Dot
DC	Direct Current
DFT	Density Functional Theory
DRIFT	Diffuse Reflectance Infrared Fourier Transform
E_a	Activation Energy
E_B	Binding Energy
E_C	Conduction Band Edge
E_D	Donor Level
EDX	Energy Dispersive X-Ray Analysis
E_F	Fermi Energy
E_{gap}	Band Gap Energy
E_{kin}	Kinetic Energy
ESRF	European Synchrotron Radiation Facility
E_V	Valence Band Edge
E_{vac}	Vacuum Level
EXAFS	Extended X-Ray Absorption Fine Structure
G	Free Enthalpy
H	Enthalpy
HOMO	Highest Occupied Molecular Orbital
ICSD	Inorganic Crystal Structure Database
IR	Infrared
KP	Kelvin Probe
LUMO	Lowest Unoccupied Molecular Orbital
MeOH	Methanol
MFC	Mass Flow Controller
ppb	Parts per Billion
ppm	Parts per Million
r.h.	Relative Humidity
rpm	Rounds per Minute
S	Entropy
SEM	Scanning Electron Microscopy
SFRD	Supercritical Fluid Reactive Deposition
SMOX	Semiconducting Metal Oxide
T	Temperature
XANES	X-Ray Absorption Near Edge Structure
XAS	X-Ray Absorption Spectroscopy
XPS	X-Ray Photoelectron Spectroscopy
XRD	X-Ray Diffraction

List of Tables

List of Figures

1. Introduction and Motivation

In our daily life, we are surrounded by gas detection devices in a wide array of different applications. Excellent examples are automated ventilation systems, air quality control systems, exhaled breath analysis and industrial safety [1]. One of the earliest application fields was in coal mining resulting from a skyrocketing need for coal in Great Britain due to the implementation of illumination devices using flammable gas from coal in the 1820s. To meet the increased demand, the mining depth had to be increased. However, the deeper layers that now were mined also had higher gas concentrations, specifically of methane and H_2S [2]. Both gases pose significant risks to the mine workers' safety, since methane is explosive and H_2S can form flammable gas mixtures with air in addition to being toxic or even deadly for humans in certain concentration ranges. The increased amount of gas, especially methane, lead to an increase in the number of mine disasters resulting in an increasing demand for gas detection systems to prevent these tragic events. In the early 1900s, small animals like canaries were used to detect dangerous levels of gas. John Scott Haldane found that small animals reacted more sensitive to increasing gas concentrations. Hence, if a canary stopped chirping, a gas leak was expected, and the miners left the mine immediately. In the following decades, several technologies were developed for the detection of gases, starting in 1925 with a device that detected combustible gases through light wave interferences. Four decades later, Naoyoshi Taguchi developed the first commercial sensor based on semiconducting metal oxides (SMOX). This, again, was initiated by a safety issue. In Japan, gas was and still is used for cooking. This led to a high number of domestic gas explosions. The commercialization of the gas sensing device by Naoyoshi Taguchi significantly decreased this number.

SMOX based gas sensors have been widely and thoroughly investigated since the 1960s when it was first discovered that the conductance of ZnO changed depending on the surrounding atmosphere [3]. Shortly after, Taguchi brought the first commercial sensor based on SnO_2 to the market which is the most widely investigated material so far (*Figure **1***). However, the interest has been shifting to other materials as well. Nowadays, researchers are also looking into WO_3, In_2O_3, TiO_2, ZnO, CuO, NiO and many other

materials as gas sensing materials. Pristine SMOX materials are easily processed, miniaturized, cheap and robust [4]. However, all of these materials require high operation temperatures (between 200 and 500 °C) resulting in high power consumption [4] and often suffer from a lack of selectivity. Specifically, the (often) strong cross sensitivity to humidity is a huge drawback which requires alternatives for pristine SMOX materials. The high operation temperatures are usually required to 1) overcome the activation energy required for reactions and 2) to ensure the recovery of the baseline material. An additional benefit is the lower baseline resistance usually observed for semiconductors at higher temperatures.

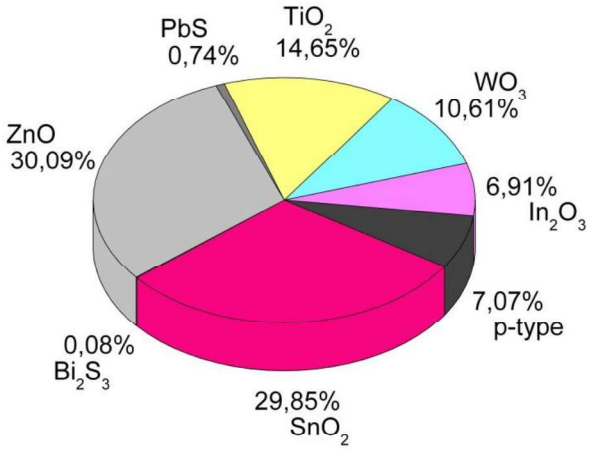

Figure 1: Number of publications on different semiconducting materials applied in gas sensors based on an internet search on https://www.webofscience.com/ on February 8th, 2022. The keywords used for the search were the respective semiconducting material in connection with "gas sensor", "gas detector", "gas detection", "gas sensing", "gas monitoring" and "gas detecting".

The focus of this Thesis was the investigation of materials that would allow for operation at temperatures below 100 °C and thereby to significantly lower the power consumption. A possible way to obtain a sensor capable of detecting gases reversibly at temperatures below 100 °C is using SMOX based heterostructures. Already the first commercial sensor from Taguchi was made from SnO_2 loaded with Pd [5]. Therefore, the investigation of heterostructures, meaning combinations of two or more SMOXs [6–11], the combination of a SMOX with a noble metal [12–15], carbon nanotube systems [16–19] or multilayer systems with filtering layers (physical or catalytic) [20–22] has been shifting into the researcher's focus.

Many researchers have been able to show the advantages of using heterostructures compared to pristine materials. However, the research is still mostly based on a trial-and-error approach. Even though the mechanisms are now better understood, the correlation between the synthesis, the structure and the function of the additive is still not fully investigated [11].

In this thesis, a WO_3 sample loaded with Pt will be investigated for its gas sensing performance at 75 °C. A number of publications exist on Pt-loaded WO_3 samples that were investigated for their gas sensing properties. However, for these sensors it was either experimentally proven, or strongly suggested by the results that the Pt-additive was present in oxidized form. The sensing mechanism discussed for these samples was usually the Fermi level pinning mechanism (see section 2.1.3). The method used to produce the samples investigated in this Thesis (this work was started but not finished during the author's Master's Thesis) was previously not reported for the production of Pt-loaded WO_3 for gas sensors. Supercritical fluid reactive deposition (SFRD) supposedly results in WO_3 samples loaded with metallic Pt clusters due to a reduction step with H_2 at the end of the process. To the author's knowledge, this material has previously not been investigated and could reveal a different sensing mechanism than WO_3 loaded with oxidized Pt. The preliminary results and conclusions from the Master's Thesis will be summarized in chapter 5.1.

Metal sulfides are an alternative class of semiconducting materials that have been getting more and more attention over the past decade. Compared to SMOX based gas sensors, this class of materials is significantly less investigated, and the mechanisms are significantly less understood. However, research in recent years has shown the potential of sulfides for low temperature gas sensing [23–26]. PbS is one of these sulfides. Impressive NO_2 sensing abilities were reported in literature before [27–29]. However, the mechanism had not been investigated. The same is true for Bi_2S_3, although significantly less work has been done on this material (*Figure **1***) [24,30]. In this Thesis, the sensing mechanisms of these two sulfides to NO_2 will be discussed in detail in addition to an explanation for their selective behaviors. The O_3 sensing mechanism of Bi_2S_3 as well as the inhibition effect of O_3 on the response to NO_2 will be investigated as well.

2. Theory and Literature

2.1. General Aspects of Chemo Resistive Gas Sensors

Gas sensors generally consist of a receptor and a transducer. The receptor recognizes analyte molecules while transducers translate the recognized molecule into a measurable signal. In chemo resistive gas sensors, this measurable signal is the change in resistance induced by reactions that take place at the surface. The processes will be discussed in more detail in the following sections.

2.1.1. Adsorption of Gases and Reception

The adsorption of gases at the surface plays a significant role in the reception process in chemo resistive gas sensors. This adsorption can be differentiated in physisorption, chemisorption or ionosorption. In physisorption, the interaction is based on van der Waals forces and only takes place at low temperatures [31]. This interaction is usually weak, fast and reversible since desorption requires little to no additional energy. In chemisorption and ionosorption, however, the interaction is significantly stronger, and it is usually accompanied by an electron transfer [32]. The processes taking place during and following the chemisorption are often complicated and are not easily described. For example, it is possible that the molecule that adsorbs at the surface dissociates while possibly charging the surface or being charged itself. Additionally, further surface reactions might take place [32]. Therefore, reversing chemisorption requires significantly more energy than reversing physisorption. In practical setups, the energy for reversing the reaction is usually obtained by heating the system or by irradiation with light [32]. Additionally, due to the formation of chemical bonds during chemisorption, this type of adsorption is highly directional and only takes place at specific sites [31].

This is also shown in *Figure **2***. The Lennard-Jones diagram shows the potential energy as a function of the distance between the surface and the adsorbate. One can see that physisorption takes place at larger distances but is also significantly weaker which can be observed as a smaller ΔH_p compared to ΔH_c. ΔE_a is the energy barrier between the chemisorbed and the physiosorbed state that is present in many but not all cases. This is

often relevant if the chemisorbed molecule is dissociated and subsequently physiosorbed at the surface.

For physisorption, the interaction between the surface and the adsorbate is very uniform across the surface and the interaction between the physisorbates is sometimes even stronger than the interaction between the surface and the physisorbate. In contrast to physisorption, chemisorption is highly directional which means that specific surface sites are needed for this interaction to take place. The exact position and orientation with respect to the surface also plays a significant role in the binding interaction [31].

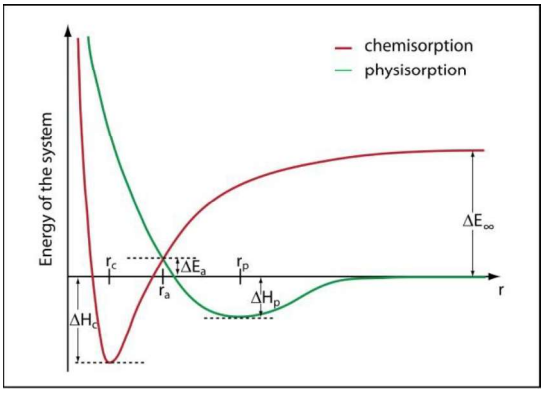

Figure 2: schematic illustration of the Lennard-Jones potential of physisorption and chemisorption in dependence of the distance r between the surface and the adsorbate; ΔH_c = heat of chemisorption, ΔH_p = heat of physisorption, ΔE_a = activation energy and the respective distances r_c, r_p and r_a, ΔE_∞ = dissociation energy. After [32].

The reception of target gases on the surface of semiconducting materials that results in a detectable signal is usually based on chemisorption. Depending on the target gas and the semiconductor, the adsorption can either be a simple chemisorption or be followed by a dissociation of the target gas resulting in a more complicated reception process.

2.1.2. Electronic Properties and Transduction

For chemo resistive gas sensors based on semiconducting materials, surface defects have been found to play a significant role. The amount of surface defects depends on a variety of factors like the temperature or the purity of the material [33]. The formation of defects is a result of thermodynamic principles that apply at temperatures above 0 K. The free enthalpy G of a material is composed of the entropy S in dependence of the temperature

T and the crystal enthalpy H (equation 1). Both the crystal enthalpy H and the entropy S increase due to the formation of defects. However, the product of the entropy S and the temperature T is a negative term which results in a minimum for the free enthalpy G (*Figure **3***)[33].

$$\delta_f^{(d)} G = \delta_f^{(d)} H - T\delta_f^{(d)} S \qquad \textbf{1}$$

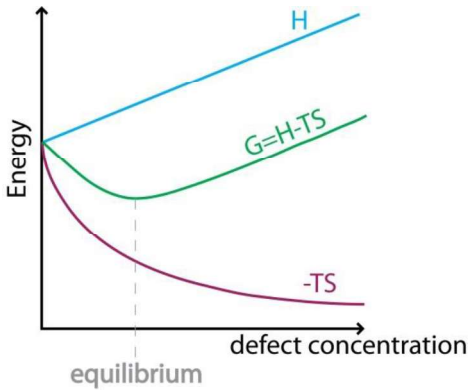

Figure 3: Schematic illustration of the contribution of the crystal enthalpy H and the entropy S to the free enthalpy G resulting in a minimum of G at a certain defect concentration. After [33].

The formation of defects influences the band structure of semiconductors. Depending on the type of defect, either a donor or an acceptor band will be formed in the band gap. This will be exemplary explained for a SMOX with oxygen vacancies as defects.

*Figure **4*** schematically shows the band structure of a semiconductor with a band gap E_{gap} between the valence band edge E_V and the conduction band edge E_C. The Fermi level E_F is in the middle of the band gap (exactly in the middle at 0 K, shifted at higher temperatures, see [34]). The formation of oxygen vacancies in SMOX materials results in the formation of a donor band E_D in the band gap E_{gap}. Equation 2 shows why.

$$O_O \leftrightarrow \frac{1}{2} O_2 + V_O^{\cdot\cdot} + 2e' \qquad \textbf{2}$$

When a lattice oxygen O_O leaves the material and forms an oxygen vacancy $V_O^{\cdot\cdot}$, it also leaves behind two electrons e'. These electrons are energetically much closer to the

conduction band than the electrons from the valence band which means less energy is required to excite them to the conduction band. Also, this is the reason why the Fermi level shifts to higher energies, because now the highest occupied electronic state is the donor level which means the Fermi level is now above the donor band [35] (defined for 0 K).

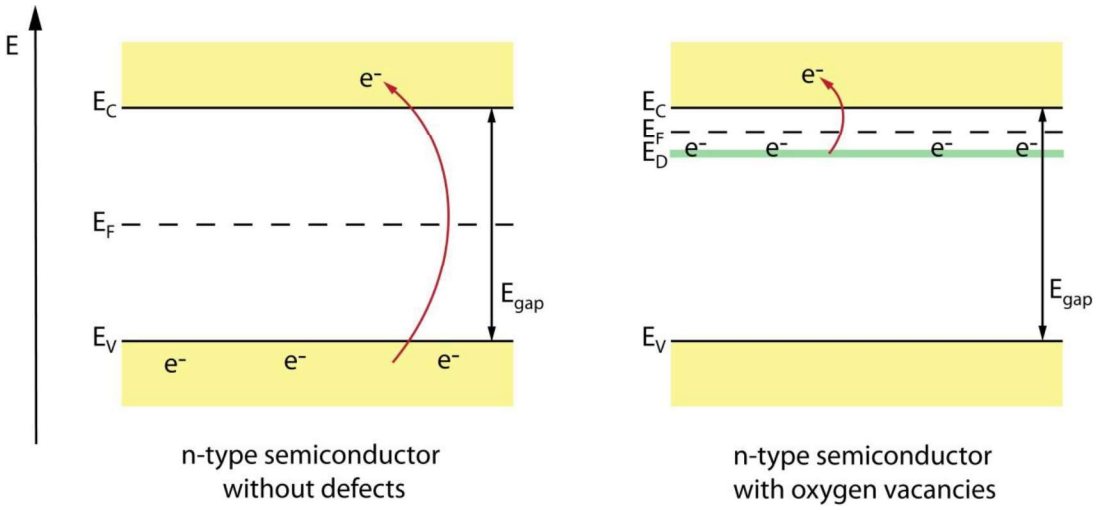

Figure 4: This is a schematic illustration of the influence of oxygen vacancies on the band structure of semiconductors. On the left, the Fermi level E_F is positioned in the middle of the band gap E_{gap} between the valence band E_V and the conduction band E_C. On the right, the Fermi level E_F is shifted between the donor band E_D and the conduction band E_C. After [35].

As mentioned earlier, the adsorption of target gases (reception) needs to be translated into a measurable signal (transduction). In chemo resistive gas sensors, this measurable signal is a change in resistance. In order to understand the transduction process, it is necessary to look at the band structure of semiconductors again. The adsorption of target gases is energetically described by surface electronic states. For example, if oxygen is adsorbed at the surface, equation 2 is reversed. This means instead of the formation of a vacancy and a release of electrons into the material, electrons get trapped by adsorbed oxygen resulting in a surface electron depletion layer (*Figure **5***).

Since the sensing layers of chemo resistive gas sensors most often are porous, the gases can diffuse through the whole layer and adsorb on the surface of all grains. If we stick to the example of an n-type semiconductor, the adsorption of oxygen on all grains results in an increase of the resistance. This is schematically illustrated in *Figure **6***. The adsorption

of oxygen at the surface results in an electron depletion layer at the surface of all grains [36–38]. This results in the formation of Schottky barriers at the grain-grain boundaries hindering the charge carriers to pass through the material. This means that due to the adsorption of oxygen the resistance of the material increases.

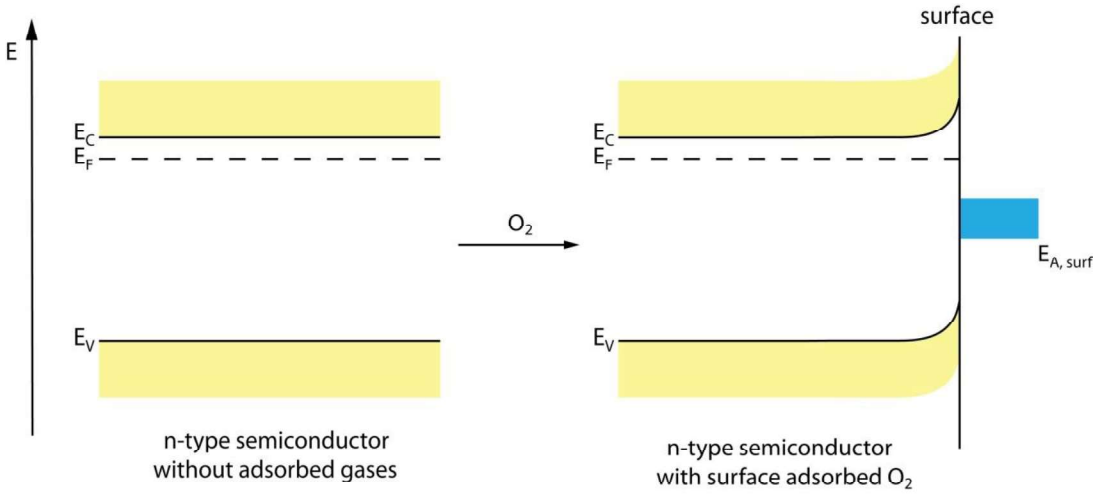

Figure 5: Schematic illustration of the influence of the formation of surface acceptor states due to the adsorption of oxygen and the resulting upwards band banding and surface electron depletion layer in n-type semiconductors. After [37].

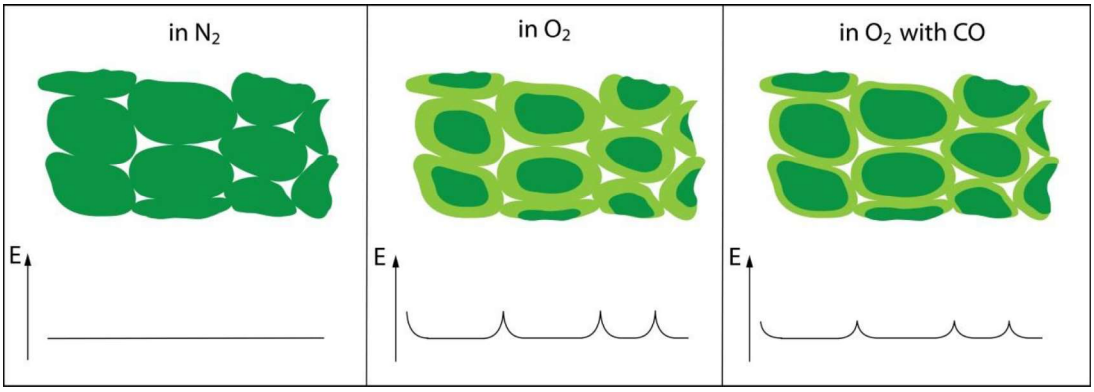

Figure 6: Schematic illustration of the Schottky barrier at grain-grain boundaries in dependence of the surrounding gas atmosphere.

Further, this explains why the resistance changes when other gases adsorb/react with the surface. CO, for example, reacts with oxygen to CO_2 at the surface of the grains. This means that previously adsorbed oxygen that trapped electrons from the material, will react with CO and release the electrons back into the material, resulting in a decrease in the upwards band bending and the thickness of the surface electron depletion layer. At

the same time, this means that the resistance of the material decreases because the barrier at the grain-grain boundaries decreases in height and the charge carriers can pass through the material more easily.

2.1.3. Noble Metal Loading

In the gas sensor community, loading base materials with noble metals has been discussed for multiple decades. The first commercial sensor by Naoyoshi Taguchi was based on SnO_2 but was loaded with Pd (unknown whether as oxide or metallic). Although it has been discussed for so long, the sensing mechanism, especially in relation to the morphology of the material, is not fully understood. A lot of fundamental research has been focused on this topic. In the 80's, Yamazoe and Matsushima have published the first suggestions for the sensing mechanisms [39,40]. These have been and constantly are refined until today. According to the current understanding, there are basically four different mechanisms when noble metal additives are involved. For example, a dopant, which is distributed throughout the whole material, can result in the formation of activated lattice species. Großmann et al. reported the activation of lattice oxygen due to the substitution of Sn^{4+} with Pt^{4+} in the lattice of SnO_2 [41,42] which resulted in an enhanced sensor response for CO and H_2. A similar effect can be observed in the presence of surface additives. In case the surface additive is a pristine noble metal, oxygen can adsorb onto the surface cluster. This results in its activation which is followed by its migration to the base material. There, the oxygen dissociates, is ionized and readily reacts with target gases. This is the so-called spillover mechanism as it was reported by Hübner et al. [43]. This mechanism can also be referred to as chemical sensitization [39,40].

If the surface additive is electronically coupled to the base material, it is spoken of electronic sensitization [39,40]. In this case, the reaction takes place exclusively on the surface of the additive resulting in its oxidation or reduction. The change in the oxidation state results in a change of the Fermi level and thereby influencing the charge distribution in its direct vicinity which results in a change in resistance. This was experimentally proven by Staerz et al. with Rh_2O_3 as a surface additive on SnO_2, WO_3 and In_2O_3 [8]. Since the resistance of the whole sample is controlled by the Fermi level of the surface additive, this mechanism is also referred to as Fermi-level control mechanism.

Using a combination of in-situ and in-operando spectroscopic methods, it is usually possible to identify the sensing mechanism. To predict the sensing mechanism of a system to a certain target gas, however, is still not possible. Even though the different sensing mechanisms are more and more understood, the correlation between the concentration, size, morphology and distribution of the surface additive on the surface of the base material is still not fully comprehended.

2.2. WO_3

WO_3 is an n-type semiconductor with a wide bandgap of 2.5 – 3.2 eV [44]. It has a number of very interesting properties resulting in its implementation in many different applications. Among these properties are its electrochromism and thermochromism which makes WO_3 an interesting material for anti-glare and anti-reflecting mirrors and smart windows [44]. Thermochromism is linked to a distortion of the crystal structure of WO_3 with changing temperature. At temperatures below 17 °C but above -50 °C, the crystal is in a triclinic form. Between 17 °C and 330 °C, WO_3 is monoclinic. Above 330 °C up to 740 °C, the crystal structure is orthorhombic [44]. The color of tungsten oxides is also dependent on the stoichiometry of the material. WO_3 has a green-yellow color, which changes to blue to brown with a change of the stoichiometry from $WO_{2.9}$, $WO_{2.72}$ to WO_2. Metallic tungsten appears grey [45].

After ZnO, SnO_2 and TiO_2, WO_3 is the most widely investigated n-type SMOX for the application in chemo resistive gas sensors (*Figure **1***). The pristine material is often reported to show good sensor responses to acetone and ethanol [46]. It was also found that loading WO_3 samples with noble metals severely influenced the sensor responses in addition to resulting in lower operation temperatures.

Pt is one of the noble metals that has been widely investigated as additive in combination with WO_3 as base material [47–52]. To my knowledge, the first report was published in the 1960s by Shaver who observed an enhanced response to H_2 [53]. This was followed by reports on enhanced sensing abilities to CO [54], NH_3 [55], ethanol [56], H_2S [57] and NO_2 [58]. Additionally, it was observed that the operation temperature could be reduced by using Pt as additive [55–58]. The sensing mechanism, however, was rarely investigated.

Most publications made assumptions based on the mechanisms proposed by Yamazoe and Matsushima [39,40] but did not support their arguments with spectroscopic data.

During my Master's Thesis, I investigated WO_3 samples loaded with low amounts of Pt [59]. The results will be shortly summarized in the following.

The Pt was added via supercritical fluid reactive deposition (SFRD) starting with $Pt(COD)Me_2$ as a precursor (see section 4.1.1) [60]. The samples were then screen printed on Al_2O_3 substrates with Pt electrodes on the front side and Pt heaters on the back side. With the help of scanning electron microscopy, it was found that the Pt clusters were all below 10 nm in diameter, and that the diameter increased with an increase in Pt concentration (*Figure **7***).

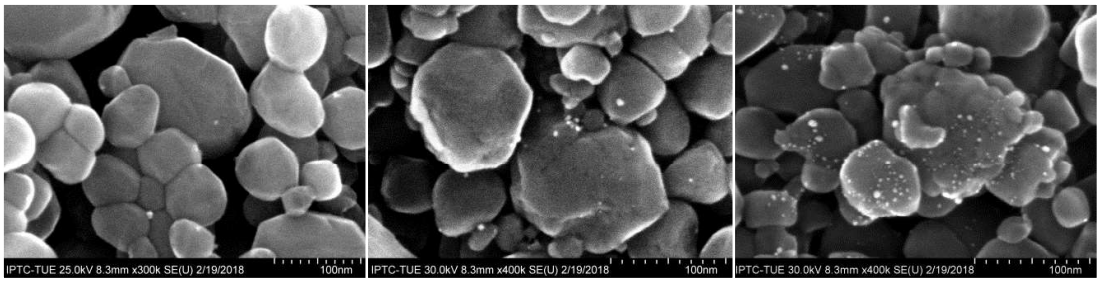

Figure 7: SEM images of pristine WO_3 (left), WO_3 loaded with 0.1 wt% Pt (middle) and WO_3 loaded with 0.2 wt% Pt (right) with a 300k fold (pristine) and 400k fold magnification (Pt loaded samples). From [59].

The measurements were conducted at 75 °C in dry air, 30 % r.h. and 80 % r.h. under the exposure to different concentrations of CO, acetone, toluene and ethanol (*Figure **8***). It was observed that the presence of Pt on WO_3 has a significant influence on the sensing characteristics. Firstly, it is observed that the baseline resistance of the sensors increases due to the presence of Pt which indicates electronic coupling between the surface additive and the base material and the withdrawal of electrons from WO_3 by Pt. Secondly, while no significant sensor responses were observed for pristine WO_3 to any of the tested gases (including humidity), the sensors with the surface loaded samples showed good responses to CO and ethanol. Additionally, responses to acetone and toluene could be observed in dry air. However, these signals were lower for the sample with 0.1 wt% Pt compared to those with 0.2 wt% Pt and decreased to negligible values in humid backgrounds. The

presence of Pt also resulted in faster response and recovery times, which becomes obvious when the resistance measurement of the sample with 0.1 wt% Pt is compared to the one with 0.2 wt% Pt.

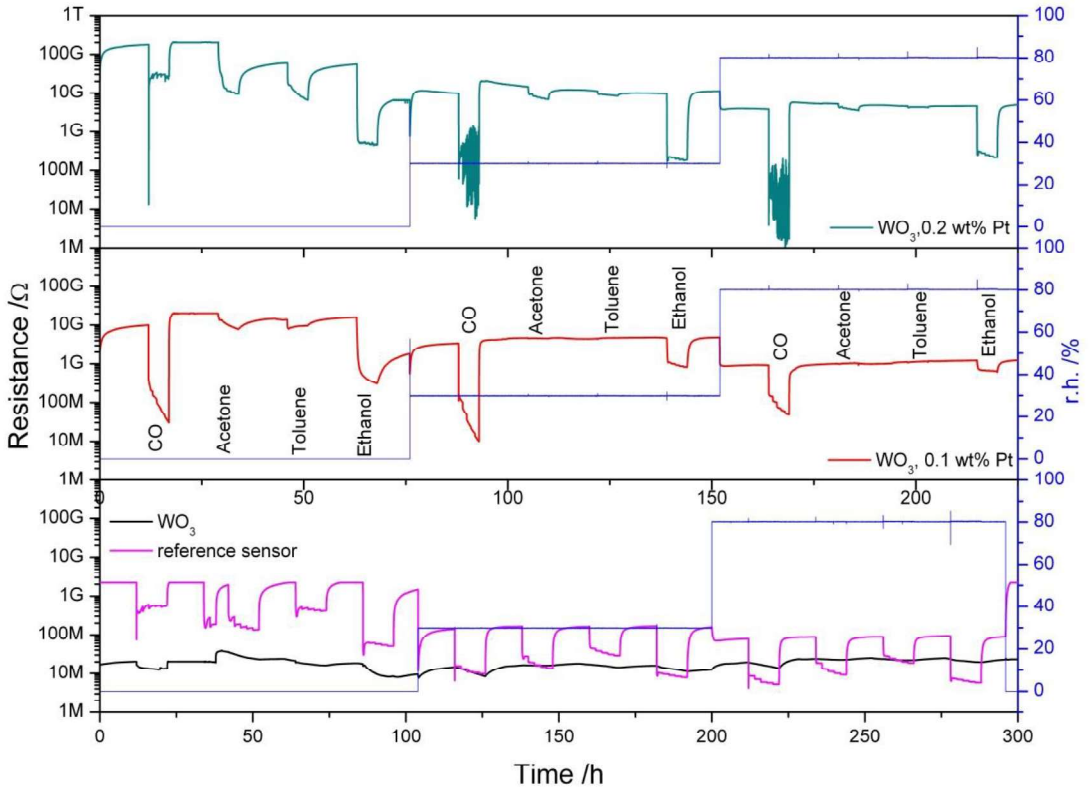

Figure 8: DC resistance measurement of pristine WO_3 (bottom), WO_3 loaded with 0.1 wt% Pt (middle) and WO_3 loaded with 0.2 wt% Pt (top) under the exposure to different concentrations of CO, acetone, toluene and ethanol in dry different background humidity levels (dry, 30 % r.h., 80 % r.h.) at 75 °C. From [59].

The underlying surface chemical reactions resulting in the observed effects on the resistance were investigated using diffuse reflectance infrared Fourier Transform spectroscopy (DRIFT spectroscopy). First, the effect of humidity on the surface was investigated (*Figure **9***). It was found that the presence of Pt resulted in a decrease in surface hydroxyl groups which was shown by the lower number of exchanged groups for the samples loaded with Pt (*Figure **9***, left). The isolated hydroxyl groups on pristine WO_3 at 3727 and 3640 cm^{-1} increase in the presence of H_2O and are exchanged in the presence of D_2O resulting in a shift of these bands to 2748 and 2684 cm^{-1}, respectively. The exchange of the isolated hydroxyl groups is not observed in the presence of Pt. Additionally, it was observed that the effect of humidity on pristine WO_3 was in general

stronger than on the samples with Pt, both on the resistance and on the surface of the samples. For pristine WO_3, a decrease in W-O bands (2064 and 1857 cm^{-1}) was observed. In addition, the intercalation of water into the lattice was found which was indicated by the increasing band at 1615 cm^{-1} in the presence of H_2O and the shift of this band to 1193 cm^{-1} in the presence of D_2O. These very dominant bands for pristine WO_3 are significantly less dominant for the samples loaded with 0.1 wt% Pt and are barely visible for the sample with 0.2 wt% Pt anymore. The band centered at 1025 cm^{-1} was assigned to W=O bonds. It was concluded that the decrease in resistance was a result of the intercalation of water in surface oxygen vacancies which in turn resulted in a shortening of W-O single bonds shifting their character to W=O double bonds.

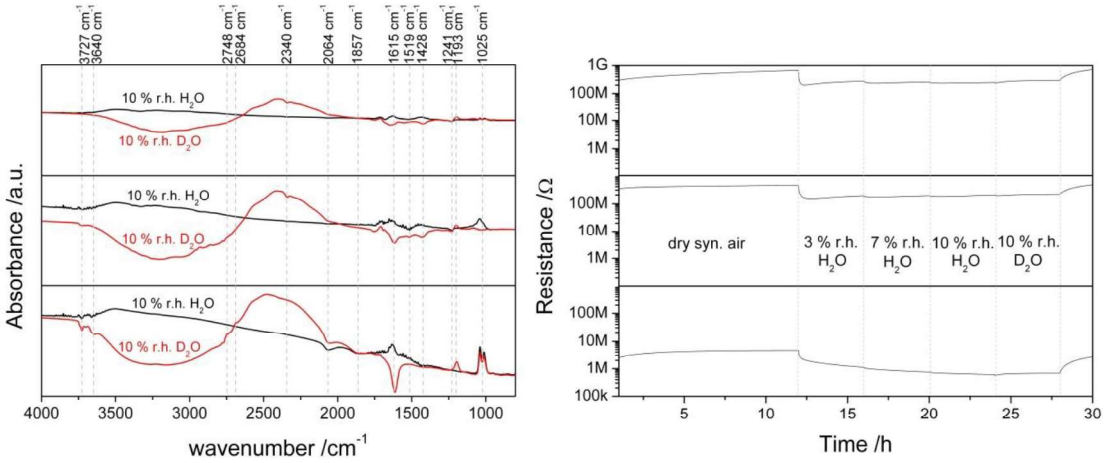

Figure 9: DRIFT spectra in 10 % r.h. H_2O and in 10 % r.h. D_2O after the exchange (left) and the corresponding DC resistance measurement recorded during the exchange experiment (right). From [59].

After the effect of humidity was understood, the surface reactions with CO were investigated in different background humidity levels (*Figure **10***). In dry synthetic air, the electrical effect of CO on pristine WO_3 was very small (*Figure **10***, right). Contrary to what would have been expected, for low CO concentrations a small increase in the resistance was observed. This changed for higher concentrations when the resistance decreased as expected. The effect of CO on the Pt-loaded samples was significantly more pronounced and a strong decrease in resistance could be observed even for low concentrations. The response of the two materials was comparable.

The DRIFT spectra explained the different behavior of pristine WO_3 compared to the Pt-loaded samples (*Figure **10***, left). For pristine WO_3, small decreasing bands assigned to W-O single and double bonds could be observed (2064, 1857 and 1025 cm^{-1}, respectively) in addition to a decreasing band at 1670 cm^{-1}. This band could not be assigned at the time. Except for the band at 1670 cm^{-1}, these bands could all be observed for the Pt-loaded samples as well. Additionally, a band at 2087 cm^{-1} was observed that shifted to 2028 cm^{-1} when exposed to ^{13}CO. These bands were assigned to metallic Pt-^{12}CO and Pt-^{13}CO bonds, respectively.

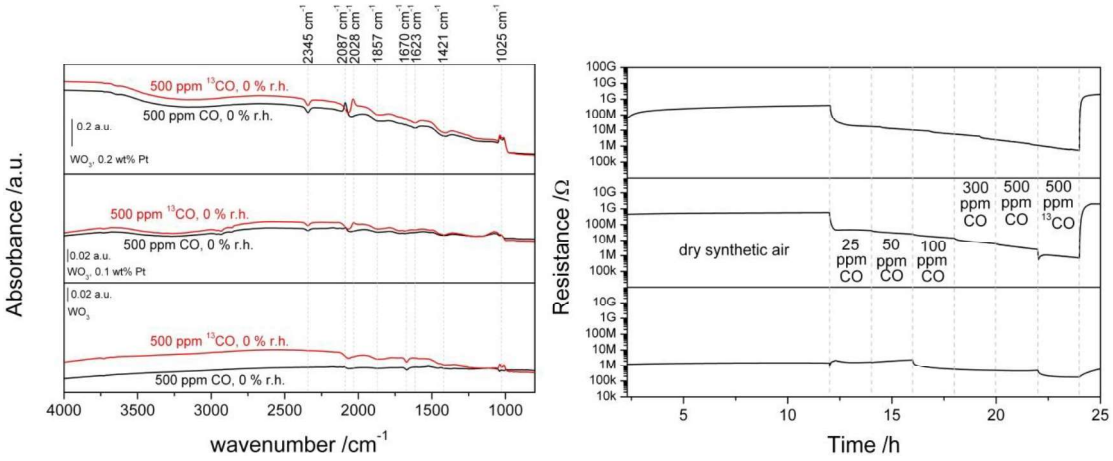

Figure 10: DRIFT spectra in dry synthetic air in the presence of 500 ppm CO and 500 ppm ^{13}CO (left) and the corresponding DC resistance measurement recorded during the exchange experiment with CO concentrations between 25 ppm and 500 ppm CO and the exchange with 500 ppm ^{13}CO (right). From [59].

In 10 % r.h., similar observations were made (*Figure **11***). The pristine material showed only a small response to CO that was correlated to a surface reduction of WO_3 indicated by the decrease of the bands assigned to the W-O bonds at 2064 and 1857 cm^{-1}. For this measurement, the band at 1670 cm^{-1} (could not be assigned) was not observed. The band centered at 1025 cm^{-1} which is assigned to the W=O double bond could not be nicely resolved here. For the Pt-loaded samples, in addition to the decreasing bands assigned to W-O single bonds, the metallic Pt-CO band at 2087 cm^{-1} and the Pt-^{13}CO band at 2028 cm^{-1} could be observed again.

The findings of the resistance measurements and the DRIFT spectra lead to the conclusion that the sensing mechanism of the Pt-loaded samples was based on a spillover mechanism which significantly enhanced the response of the sensors to the presence of CO at 75 °C.

The DRIFT spectra also indicated that the Pt surface clusters were mostly metallic since the only CO-band that could be observed could be assigned to the Pt^0-CO band. The oxidation state of the Pt surface clusters was not confirmed during the Master's Thesis, however. The answer to this question, as well as the final proof for the spillover mechanism with CO will be presented in this Thesis. Further, the reaction of pristine WO_3 at 75 °C with CO will be examined in more detail in order to explain the unexpected behavior of the resistance observed in low CO concentrations.

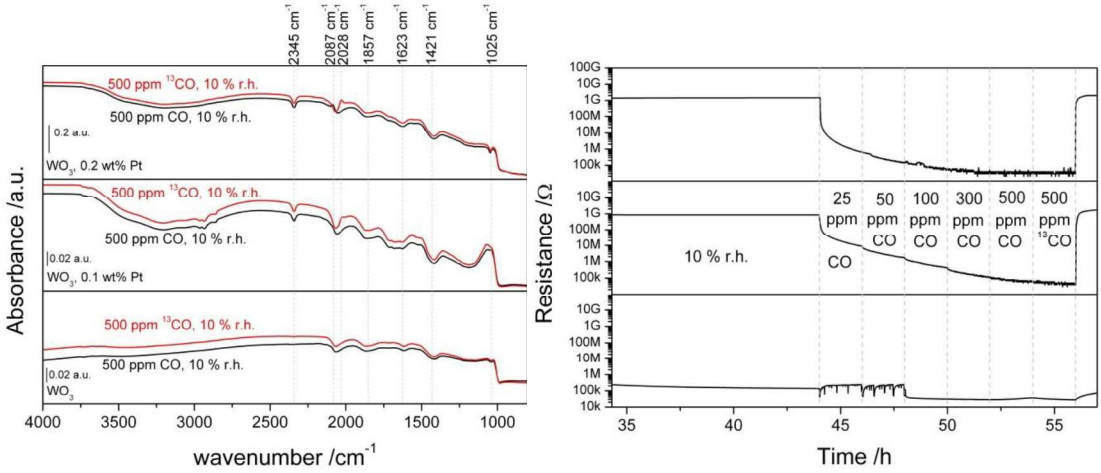

Figure 11: DRIFT spectra in 10 % r.h. in the presence of 500 ppm CO and 500 ppm ^{13}CO (left) and the corresponding DC resistance measurement recorded during the exchange experiment with CO concentrations between 25 ppm and 500 ppm CO and the exchange with 500 ppm ^{13}CO (right). From [59].

2.3. PbS

PbS is a semiconducting material that can be both show p- and n-type behavior [61]. It occurs naturally as the mineral galena which is often used to extract lead from [62–66]. The material has a narrow and direct band gap with a value of 0.41 eV [67–70] which can be tuned in dependence of the grain size as a result of the quantum confinement effect (see section 2.3.1) [71]. The large Bohr exciton radius of PbS with 18 nm [72] results in an effective charge separation. PbS has been and still is investigated for a wide array of

applications like photovoltaics [71,73], solar cells [74–76], and photodetectors [73,77–79]. In recent years, PbS has also been investigated for the detection of a variety of gases, especially at low temperatures; this is a big advantage over SMOX materials [28,80–84]. On the other hand, PbS is toxic for humans and the environment and needs to be handled with care. This might be part of the reason why the amount of research on PbS as a gas sensing material is considerably lower than the number of publications on SMOX based gas sensors (*Figure **1***). Navale et al. investigated the gas sensing ability of PbS thin films for H_2S, NH_3, C_2H_5OH, CH_3OH, Cl_2 and NO_2 [80]. They operated their sensing device at room temperature in a static system and measured the change of resistance when exposed to 100 ppm of each of the test gases. They observed a selective behavior for NO_2 with a response of 78 % compared to responses below 10 % for the other test gases [80]. Mosahebfard et al. investigated the effect of each 1 % of methane, oxygen, ethanol and CO on the resistance of a PbS sensor and found a fairly selective response for methane [28]. Liu et al. and Li et al. both looked into the sensing abilities of PbS colloidal quantum dots for 50 ppm H_2S, SO_2, NO_2 and NH_3 and found a very high and selective response for H_2S at an operation temperature of 135 °C [82,85]. All of them suggested sensing mechanisms related to reactions with surface adsorbed oxygen. However, none of the mentioned publications did any spectroscopic studies to confirm the suggested mechanisms. Additionally, as already mentioned earlier, the number of publications on PbS as a sensing material is very low. There are still a lot of questions concerning the surface reactions leading to the detected change in resistance. This Thesis will present extensive evidence of the surface reactions induced by NO_2 resulting in the observed response at room temperature with differently prepared PbS samples. Also, the effect of the sensor preparation process on the sensing properties will be discussed.

2.3.1. The Quantum Confinement Effect

Over the last few decades, zero-dimensional materials like quantum dots have been getting more and more attention. This interest is partially based on the fact that the band gap of quantum dots can be tuned by controlling their size. In order to understand how this is possible, it is necessary to look into how energy bands are formed in solid materials. Each atom has orbitals at certain energies. If a second atom gets close to the first atom, the orbitals overlap, and a bonding and antibonding orbital is formed where the bonding

orbital has a lower energy than the atomic orbital, and the antibonding is at a higher energy. This will happen with every further atom that is added to the structure resulting in the formation of further molecular orbitals. At some point, the energies of the molecular orbitals will be so close together that they are considered to be an energy band of finite width [86]. This is schematically illustrated in *Figure **12***. Now it becomes clear why it is possible to tune the band gap of nanostructures. By decreasing the size of nanoparticles below a certain limit, the bands become discrete energy levels and the band gap becomes controllable [86].

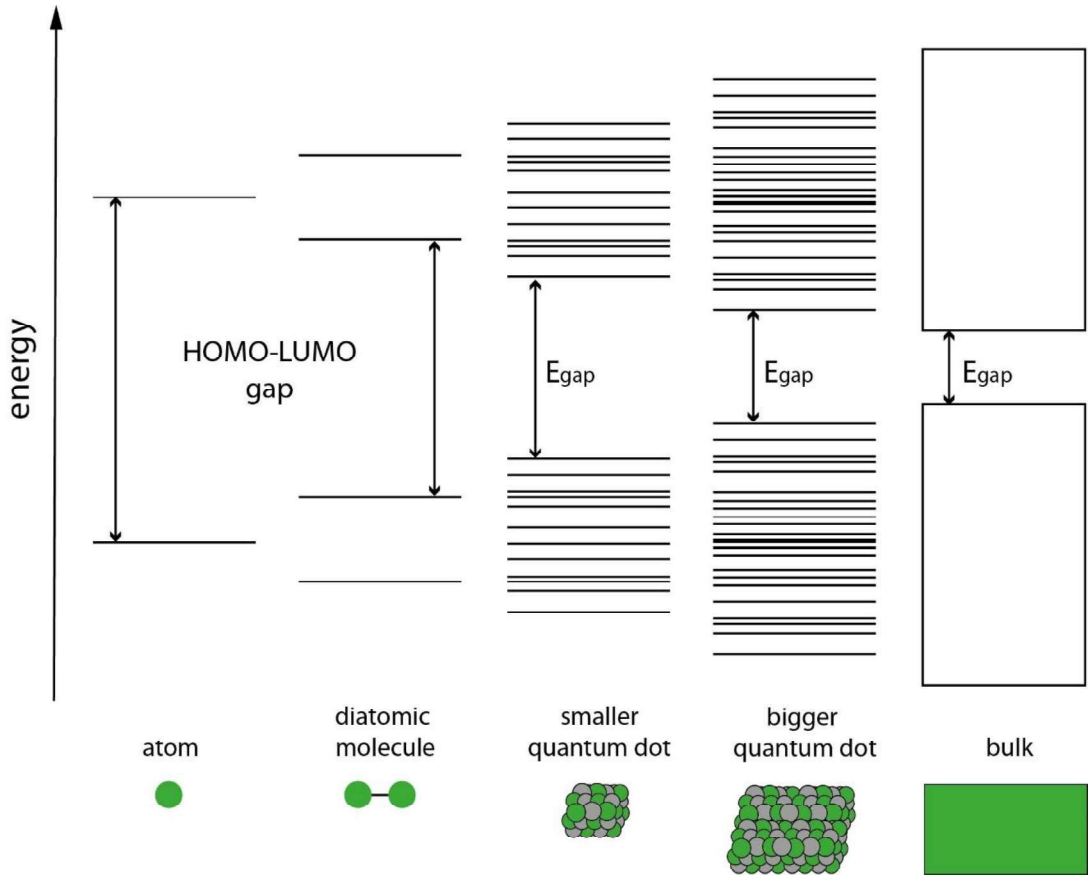

Figure 12: Schematic illustration of the changing structure of energy bands based on the increasing number of atoms.

2.4. Bi_2S_3

Bi_2S_3 is an n-type semiconductor with a band gap value of 1.3 – 1.4 eV. In contrast to PbS, Bi_2S_3 is not toxic to health and environment and in that regard has a big advantage over PbS. Just like PbS, Bi_2S_3 has a variety of different application fields including photovoltaics

[87,88], photodiodes [89,90] and bio-imaging [91,92]. Recently, Bi_2S_3 caught the interest of the gas sensor research community as well. However, the overall amount of research on this topic is low. One of the first reports on the gas sensing properties of Bi_2S_3 is from 2008 by Yao et al. [93]. They investigated the material's ability to detect H_2 in a nitrogen background and found a dependency of the change in conductance on different concentrations of H_2 when operating the sensors at room temperature [93]. Yang et al. investigated the sensing ability of Bi_2S_3 to ethanol, NH_3, H_2S, NO_2, CH_4, NO and H_2 at room temperature and found a response of 12 % to 5 ppm ethanol. The responses to 50 ppm of each of the other gases were lower [94]. Fu et al. reported a selective response to NH_3 over a number of VOCs like ethanol, methanol and benzene when operating the sensor at 30 °C and in 48 % r.h. [95]. Kan et al. reported a selective response to NO_2 over SO_2, H_2S and NH_3 at an operation temperature of 18 °C [24]. The reports on the sensing characteristics of Bi_2S_3 varied a great deal in the type of gases that could be detected. While Fu et al. claim a selective response for NH_3 over ethanol and other VOCs, Yang et al. report a selective response for ethanol over NH_3 among other gases. However, the sensing materials were prepared through different synthesis strategies which could have an effect on the sensing characteristics. This was certainly observed for other sensing materials [96]. As in the case for sensors based on PbS, none of these studies did in-operando investigations on the sensing mechanism or any chances related to the exposure to the tested gases. In this Thesis, the sensing characteristics of Bi_2S_3 nanorods prepared through a hydrothermal approach were tested at 50 °C at three different background humidity levels and under the exposure of a number of different gases. The sensing mechanism to NO_2 was extensively studied, as well as the observed inhibiting effect of previous exposures to O_3 on the sensor response to NO_2.

3. Fundamentals of the Experimental Methods

3.1. *Ex-situ*, *in-situ* and *in-operando*

Ex-situ, *in-situ* and *in-operando* are terms used to describe the conditions the experiments were conducted in with regard to realistic conditions. *Ex-situ* experiments are done in conditions that are in no way related to realistic conditions. For example, X-ray photoelectron spectroscopy (XPS) is done in ultra-high vacuum conditions. Gas sensors, however, require the presence of low pressures of gases otherwise there is nothing the gas sensor can detect. Therefore, the standard XPS experiment is usually described as an *ex-situ* experiment. The description changes to *in-situ* when the experiments are for example done at low pressures as was reported by Junker et al. among others [97]. They conducted XPS experiments at total pressures of 1 mbar instead of in ultra-high vacuum and were able to measure the resistance of the samples simultaneously. While this gives information on changes at the surface concerning the composition and the oxidation states of the surface elements, in later experiments it was found that the pressure has a significant effect on the resistance which is why this experiment is described as *in-situ*. Experiments that are done in realistic conditions, this means at the best operation temperature and application relevant pressures with a real sensor device that enable the simultaneous evaluation of the sensor response are described as *in-operando*.

Many of the experiments that are shown and described in this Thesis are done *in-operando*. If the experiments were done *in-situ* or *ex-situ*, this will be stated in the respective section on the experimental method.

3.2. Diffuse Reflectance Infrared Fourier Transform Spectroscopy

With diffuse reflectance infrared Fourier transform spectroscopy, short DRIFT spectroscopy, it is possible to measure the changes at the grainy surfaces of sensing devices due to the exposure to target gases *in-operando*. This means, it is possible to monitor the sensor's resistance and to correlate the change in resistance to chemical changes at the surface at relevant operation temperatures. The theory behind this method is the same as in basic infrared spectroscopy and can be found in detail elsewhere

[98]. Radiation can induce a change of the electric dipole moment which gives characteristic information about the sample. In accordance with equation 3, the observed frequency depends on the masses of the involved atoms described by m_{eff} (equation 4) and the strength of the bond described by k_f.

$$\tilde{\upsilon} = \frac{1}{2\pi c}\sqrt{\frac{k_f}{m_{eff}}} \quad \textbf{3}$$

$$m_{eff} = \frac{m_1 m_2}{m_1 + m_2} \quad \textbf{4}$$

In most common IR spectroscopy setups, the transmitted radiation through a pellet is detected. As indicated by the name, in DRIFT spectroscopy the diffusely reflected radiation is monitored. This is possible with the help of special optical mirror systems. The beam is adjusted on the sample with the help of multiple mirrors, including a parabolic mirror, where the beam is reflected. The reflected radiation is collected by a second parabolic mirror and directed towards the detector. Usually, the reflection of the beam is a mixture of diffuse and specular reflection. The amount of specular reflection, however, is low for samples with a rough surface. For both cases, the beam will penetrate the surface of the sample and gather information on the surface chemistry and the changes due to the exposure to certain conditions.

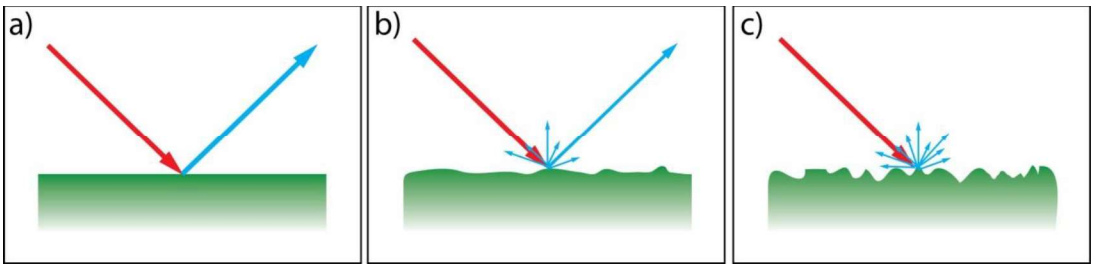

Figure 13: Schematic illustration of the differences between specular reflection (a, blue), a mixture of specular and diffuse reflectance (b, blue) and diffuse reflectance (c, blue) of the incident radiation.

3.3. X-Ray Absorption Spectroscopy

X-ray absorption spectroscopy (XAS) is an inner shell spectroscopy. This means that an atom is either excited (energy of the x-ray photon elevates an electron from the core level

to an unoccupied level) or ionized (electron is ejected from the atom). The required energies for these processes are characteristic for each element and compound giving information on its electronic structure (XANES – X-ray absorption near edge structure) and the neighboring atoms (EXAFS – Extended x-ray absorption fine structure) of the respective element [99].

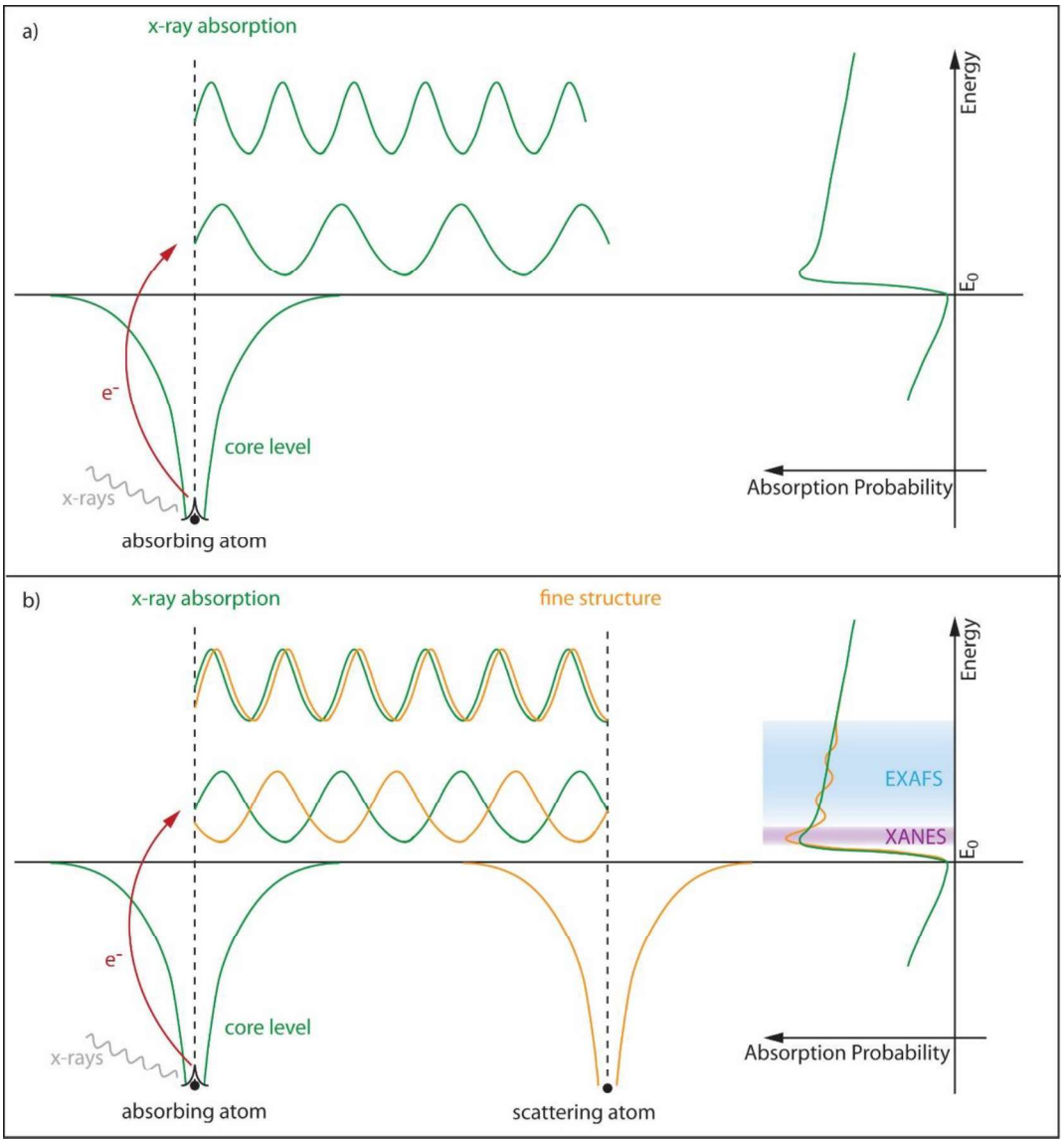

Figure 14: Schematic illustration of the potential wells and the resulting absorption of a) a monoatomic absorbing material and b) an absorbing atom with a neighboring scattering atom. Adapted from [99–101].

When the energy of the photon is high enough to excite or eject an electron from the core level, a sharp absorption edge is observed (*Figure* ***14***a, right side). The position of this

absorption edge shifts depending on the oxidation state of the respective element. In the case of a noble metal like Pt, for example, the L_3 – edge (absorption edge for the deepest shell) for metallic Pt is observed at 11,563.9 eV, for PtO_2 the L_3 – edge is at 11,565.6 eV [102]. The position of the absorption edge is what is investigated in XANES (*Figure **14***b, right). In EXAFS, one looks at the fine structure after the absorption edge which gives information on the neighboring atoms (*Figure **14***b, right). If an electron is ejected from a core level, it has a kinetic energy which is the difference between the energy of the incident photon and the binding energy. The ejected electron is described by a wave function where the wavelength decreases with increasing kinetic energy. When there is a neighboring atom, the wave is scattered and superposes the incoming wave. The result of this superposition depends on the atom that absorbed the photon energy (the wave function of the ejected electron) as well as the distance to the neighboring atom (bond length). Both are characteristic for specific elements and their combinations giving the possibility to clearly identify the investigated system [99].

3.4. X-Ray Photoelectron Spectroscopy

Similar to XAS, in x-ray photoelectron spectroscopy (XPS) core electrons are emitted and monitored. However, in XPS the kinetic energy of the ejected electron is the measure of interest [103]. The method is very surface sensitive since only electrons that are close to the surface can escape. Electrons that are deeper in the bulk of the material will lose energy due to inelastic scattering effects and will not be able to leave the material. The measured kinetic energy E_{kin} can be used to determine the binding energy E_B of the electron which is the difference between the incident x-ray photon energy $h\nu$ (usually an Al K_α or Mg K_α source with energies of 1.487 keV or 1.254 keV, respectively) and the measured kinetic energy of the electron E_{kin} [103]. The binding energy E_B is characteristic for each element and compound. In XPS, it is also possible to observe secondary effects like the ejection of Auger electrons which can disturb or cover up certain regions of the spectrum. The energies for these effects are also well known and can be found in many publications and reference tables [104].

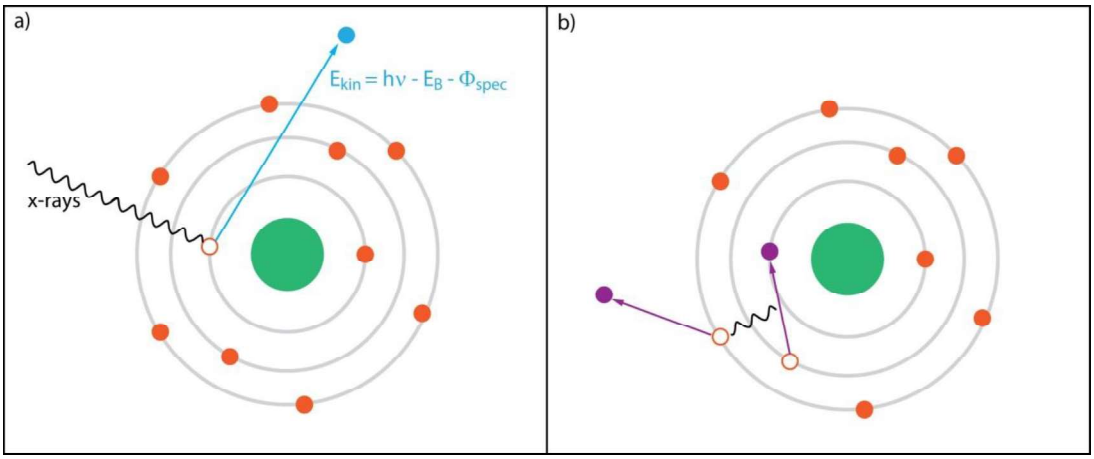

Figure 15: schematic illustration of the processes during x-ray photoelectron spectroscopy: a) emission of a primary electron; b) the hole in the inner shell is filled with an electron of one of the outer shells, the released energy can result in the emission of a secondary electron, this electron is an Auger electron. After [103].

3.5. Kelvin Probe Measurements

As was discussed in section 2.1.2, the adsorption of gases influences the surface band bending and as a result changes the work function at the surface. With the Kelvin Probe setup, it is possible to directly measure the work function changes and to correlate them to changes in the surrounding atmosphere [105]. In principle, the Kelvin Probe setup is a parallel plate capacitor where the work function of the material of the tip and the work function of the sample are different. When the two materials are electrically contacted, charges start to flow until the Fermi levels are aligned. The rearrangement of charges results in the formation of a bias across the capacitor which is called the contact potential difference [106]. With the help of a backing potential, it is possible to shift the relative position of the Fermi levels again and thereby to control the bias across the capacitor [105,106]. There are two different principles to measure the change in contact potential difference with the help of the backing potential. If you choose to operate the system in locking or zeroing mode, the backing potential is adjusted until the change in contact potential difference is zero. The mode that was used in the measurements shown in this Thesis is the so-called non-locking mode. Here, the backing potential is varied in a much higher range and the amplitude of the current is measured at (at least two) different voltages. The obtained values are linearly interpolated which enables the determination of the backing potential where the current is zero.

Kelvin Probe measurements are a useful tool to investigate the conduction mechanism in semiconducting materials under different gas atmospheres which has been shown repeatedly [107,108].

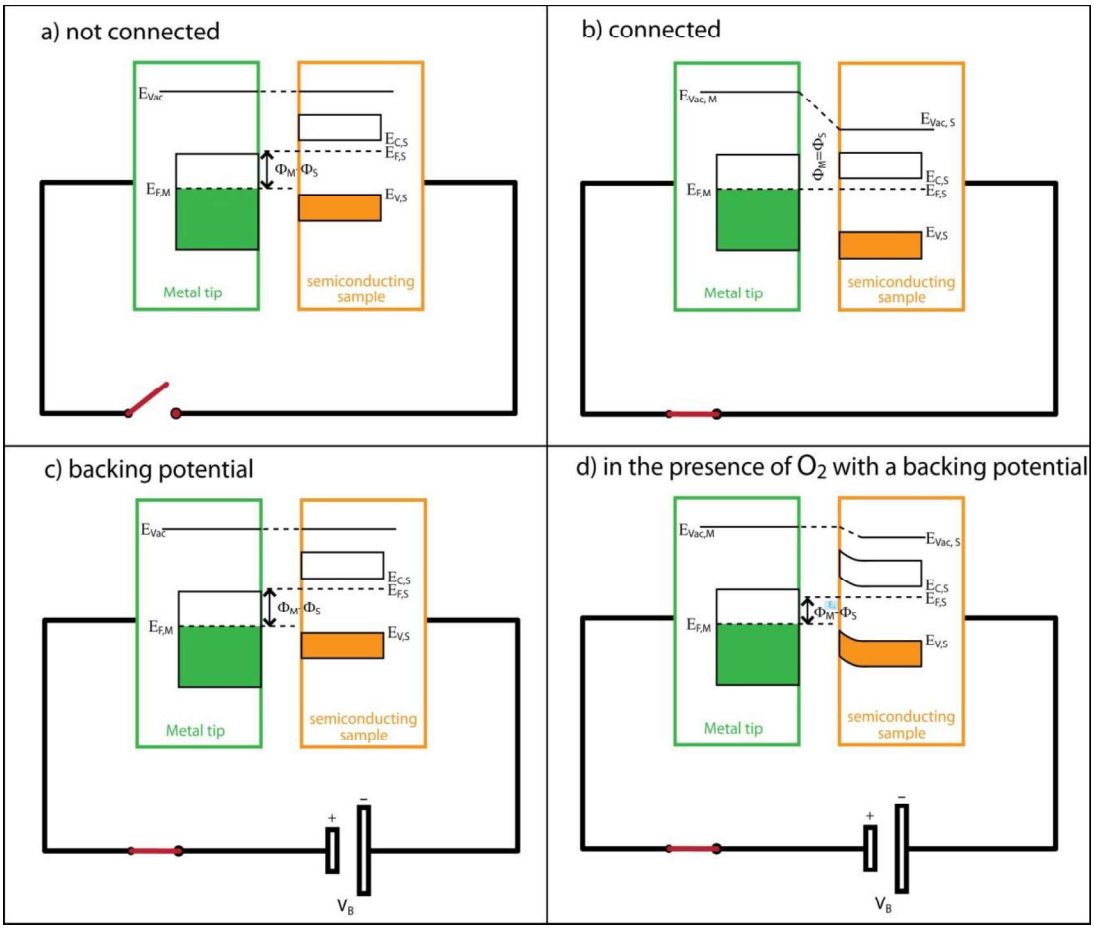

Figure 16: Schematic illustration of the CPD measurement. a) The metal tip and the semiconducting sample are not connected, and the vacuum levels are at the same height. b) The metal tip and the semiconducting sample are connected which results in the rearrangement of charges until the Fermi levels of the two materials are aligned. c) By applying an appropriate backing potential, the vacuum levels can be aligned again to the initial values. d) in the presence of oxygen, the bands of the semiconducting material show an upwards band bending which influenced the work function at the surface of the semiconducting material resulting in a smaller contact potential difference than in the absence of oxygen. Adapted from [109].

In general, the change in work function $\Delta\phi$ is the sum of the change in surface band bending $e\Delta V_s$, the change in electron affinity $\Delta\chi$, and the change in distance between the conduction band and the Fermi level $\Delta(E_c\text{-}E_F)$ (equation 5). Since the latter is related to bulk properties which are not affected by surface reactions, it stays constant. The electron

affinity changes when surface dipoles are formed like it would be the case if humidity were present and would react with the surface. For the reaction with oxygen, however, the electron affinity is expected to stay constant which means that this term can be neglected. For reactions that only influence the surface net charges, this only leaves the surface band bending and equation 5 can be simplified to equation 6, which also shows how the measured CPD can be set in relation to the band bending and the change in work function.

$$\Delta\Phi = e\Delta V_S + \Delta X + \Delta(E_C - E_F) \quad \textbf{5}$$

$$e\Delta V_S = \Delta\Phi = -\Delta CPD \times e \quad \textbf{6}$$

$$\frac{R_{gas}}{R_0} = exp\left(\frac{e\Delta V_S}{mkT}\right) \quad \textbf{7}$$

Equation 7 shows how the change in surface band bending is related to the measured resistance R. Using equation 7 to fit a plot of the resistance R as a function of the change in surface band bending $e\Delta V_S$ allows for the determination of whether a material follows a depletion layer-controlled or an accumulation layer-controlled conduction mechanism. If the value for m is 1, the material follows a depletion layer-controlled conduction mechanism. Is the value for m equal 2, the material follows an accumulation layer-controlled conduction mechanism.

4. Materials and Experimental Methods

4.1. Sample Preparations

4.1.1. Pt-Loaded WO_3

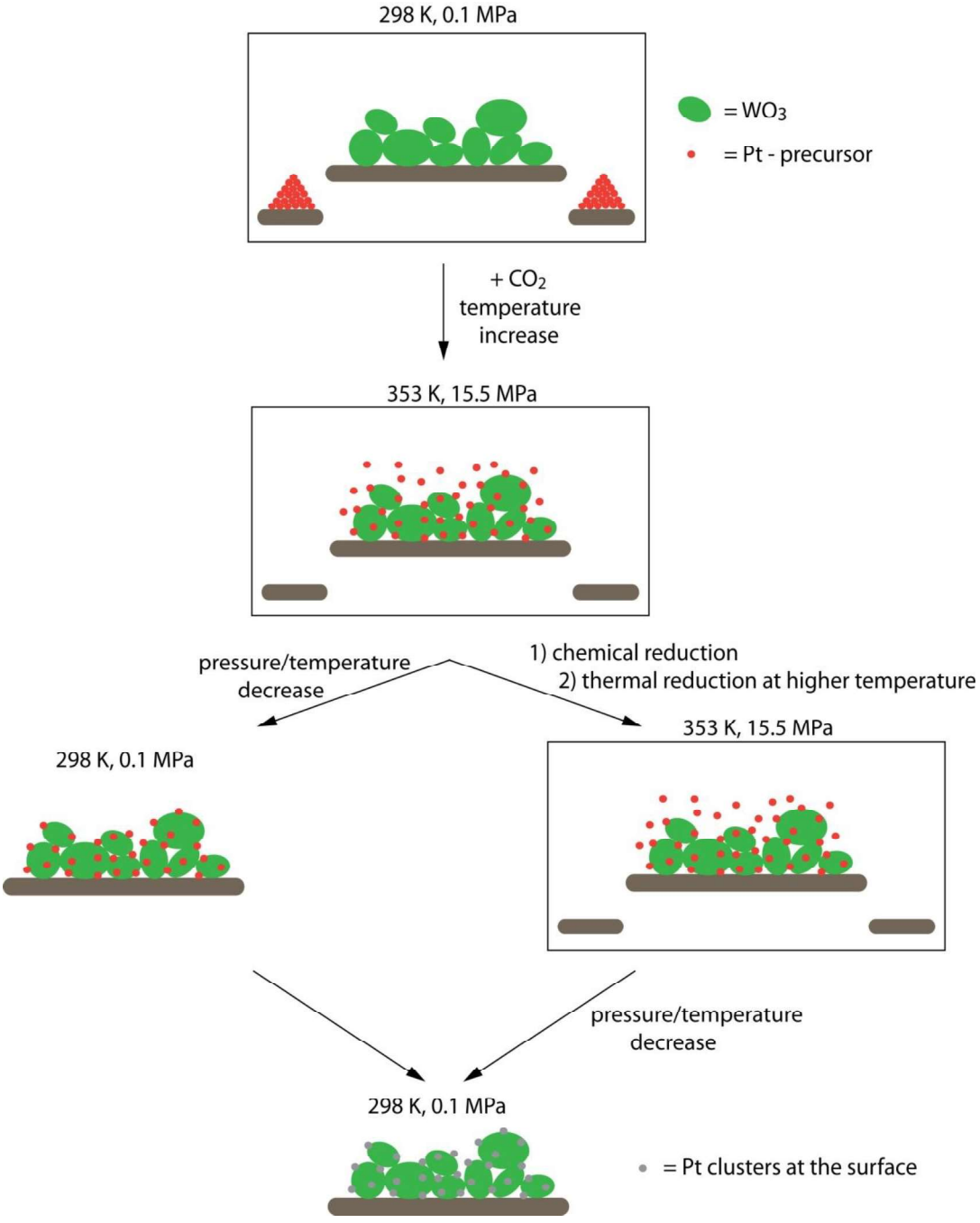

Figure 17: schematic illustration of the supercritical fluid reactive deposition method that was used to deposit Pt on WO_3.

The synthesis was performed by a former colleague at the Karlsruhe Institute of Technology, Germany as part of her Master's Thesis [60]. Pristine WO_3 was purchased from Sigma Aldrich and was used without any pretreatment. The Pt-precursor $Pt(COD)Me_2$ was purchased from ABCR GmbH. The pristine WO_3 and the Pt-precursor were put in separate reaction trays and introduced in a reactor. The reaction chamber was slowly evacuated and then carefully flushed with CO_2 until a pressure of 5 MPa was reached. In the next step, the temperature was increased to 353 K while supercritical CO_2 was introduced until a pressure of 15.5 MPa was achieved. With the help of a magnetic stir bar, the reaction components were mixed for 20 h. Following the so-called impregnation phase, there were two different options to continue the deposition: Either the surface clusters were reduced chemically/thermally followed by the reduction of the pressure and a temperature decrease, or the pressure and temperature were reduced before the thermal/chemical reduction. The samples investigated in this work underwent the chemical reduction process before the pressure went back to normal pressure. The so obtained powders were used for the sensor preparation via screen printing without any further pretreatment.

4.1.2. PbS

PbS colloidal quantum dots were synthesized by the Huan Liu group at the Huazhong University of Science and Technology in Wuhan, P.R. China by the method described in reference [110]. PbO (8.0 mmol), oleic acid (19.2 mol) and 1-octadecene (20 mL) were added to a three-neck flask. The flask was evacuated, then heated to 90 °C and kept like that for 8h. In the next step, the mixture was heated to 120 °C until the solution was clear (approximately 30 mins). After a mixture of TMS (280 µL, 2 mM) in 1-octadecene (10 mL) was quickly injected under a constant nitrogen flow, the solution was stirred for 15 s. The flask was then cooled to 36 °C in an ice bath and finally centrifuged for 5 min at 8000 rpm. The black precipitate was washed twice with acetone and then stored in octane (50 $mg*mL^{-1}$). The obtained product was PbS colloidal quantum dots stabilized with oleic acid at the surface.

4.1.3. Bi_2S_3

Bi_2S_3 nanorods were synthesized by the same cooperation partner as PbS, the Huan Liu group at the Huazhong University of Science in Technology in Wuhan, P.R. China. The sample was synthesized via a hydrothermal route starting with the precursors triphenyl bismuth (0.30 mmol) and dibenzyl disulfide (0.30 mmol) dissolved oleyl amine (2 mL). The mixture containing the precursors was mixed with a polyvinyl pyrrolidone – absolute ethanol solution (0.2 g in 13 mL). The reaction mixture was transferred to a Teflon-lined stainless-steel autoclave that was kept at 180 °C for 8 h. This resulted in the formation of a grey-black precipitate that was washed with ethanol and hexane. The nanorods - stabilized with oleyl amine at the surface - were stored in absolute ethanol (20 $mg*mL^{-1}$).

4.1.4. Deposition Methods

The materials were deposited differently onto the Al_2O_3 substrates. The WO_3 samples were deposited via screen printing. A paste of the nano powder with 1,2-propanediol was prepared in a mortar and pestle. After making sure that the paste was homogeneous, it was transferred to the molecular sieve where it was casted onto the substrates with a squeegee (Figure 18). In order to remove the residual solvent, the sensors were left at room temperature for four hours and for an additional 12 h at 80 °C in a drying oven. This was followed by a heat treatment in a tubular furnace that was heated to 500 °C in the center of the tube. The sensors were placed in a ceramic vessel that was pushed through the tubular furnace. Depending on the position on the tube, the temperature could be controlled. The sensors were kept at 400 °C for 10 mins, followed by 10 mins at 500 °C and again 10 mins at 400 °C. Then the sensors were cooled back down to room temperature. The sensors were used as obtained after heat treatment.

The sulfide materials were deposited via spin coating (Figure 19). Both materials were stored as a dispersion which enabled the direct deposition on the substrate via spin coating. However, both materials were stabilized with an organic ligand which required a ligand exchange during the deposition process since the organic ligands are insulators and resulted in a very high baseline resistance.

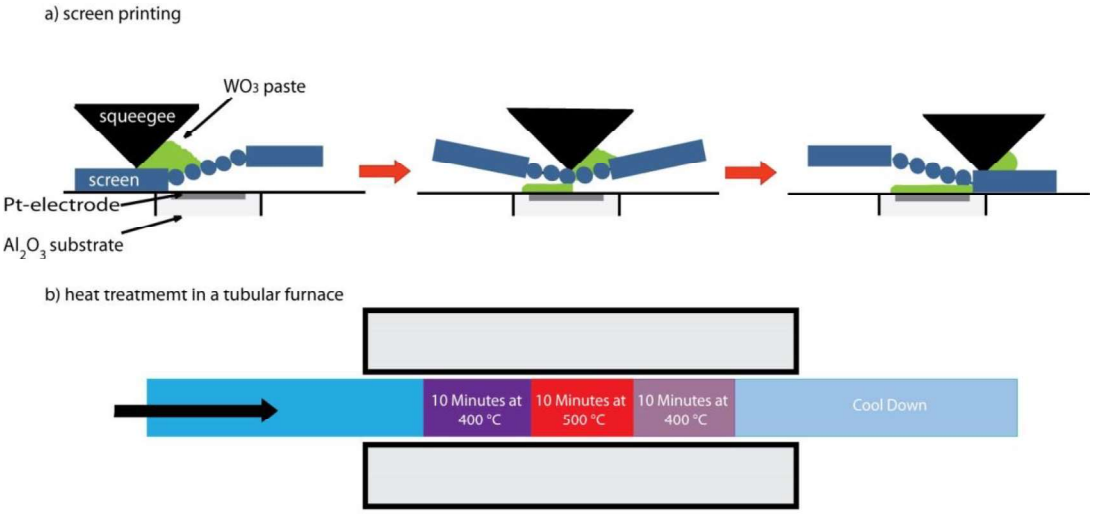

Figure 18: Schematic illustration of the screen-printing process which is followed by a heat treatment in a tubular furnace.

For the PbS ligand exchange, two different solutions were used – NH_4Cl in MeOH and $NaNO_2$ in MeOH, both 10 mg*mL^{-1}. 20 µL of the PbS dispersion were dropped on the substrate and spun for 30 s at 1500 rpm. The first layer was exchanged with 20 µL of the NH_4Cl solution (again spun for 30 s and 1500 rpm) and washed with 20 µL MeOH. Then, a second layer of PbS was applied and exchanged with the NH_4Cl solution (and washed). The third and fourth layer were exchanged with 20 µL of the $NaNO_2$ solution and subsequently washed with MeOH.

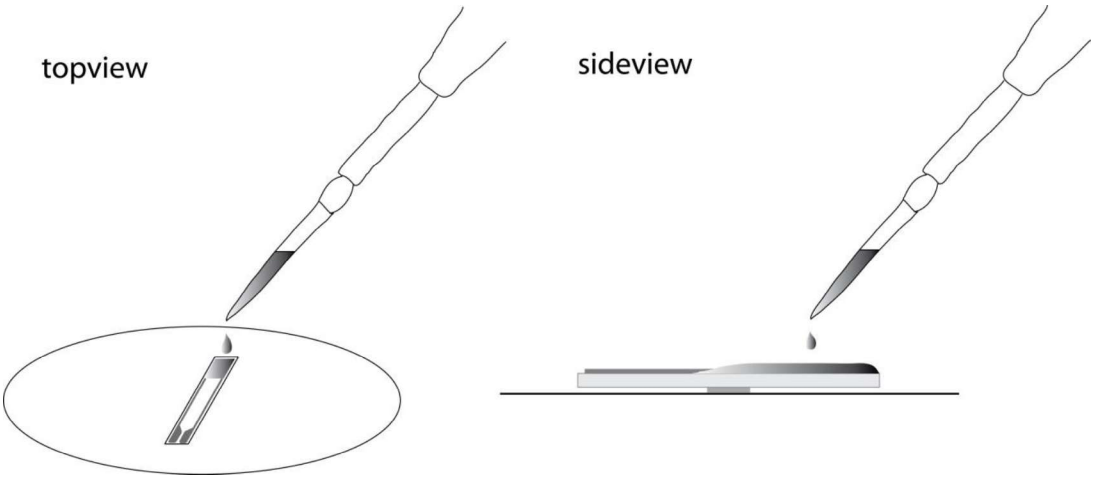

Figure 19: schematic illustration of the spin coating setup from the top (left) and the side (right).

The organic ligand at the surface of the Bi_2S_3 nanorods was exchanged with the help of a $Pb(NO_3)_2$ solution in MeOH (10 mg*mL^{-1}). 20 µL of the Bi_2S_3 dispersion was dropped on the substrate and spun for 30 s for 1500 rpm. For the exchange, 20 µL of the $Pb(NO_3)_2$ solution was dropped on the Bi_2S_3 layer and spun for another 30 s at 1500 rpm. The layer was washed with 20 µL of MeOH. This three-step procedure was repeated nine times afterwards. The spin coated sensors were used as prepared.

In order to operate the sensors at certain temperatures (WO_3, WO_3 loaded with Pt, Bi_2S_3 – the PbS sensors were operated at room temperature), the Pt-heaters on the backside of the Al_2O_3 had to be calibrated. This was done with the help of an infrared Thermometer (Maurer KTR 2300) that measured the temperature of the sensing layer in dependence of the resistance of the Pt-heater. The resistance was obtained with the help of Ohm's law. The applied voltage was divided by the measured current. The resistance and the temperature show a linear relation.

4.2. Experimental methods

4.2.1. Basic Material Characterization

For the basic characterization of the material's morphology, Scanning Electron Microscopy (SEM) combined with energy dispersive x-ray spectroscopy (EDX) was used. The images were recorded on the sensor substrate in order to obtain information on the actual sensing layers and to exclude any additional effects of the sensor preparation method on the surface. For the WO_3 samples and PbS, a HITACHI SU8030 with ultra-high-resolution imaging (≈ 1 nm) was used. The Bi_2S_3 samples were investigated with a JEOL JSM-6500F (SEM and EDX).

4.2.2. Gas Mixing Systems

The gas mixing systems in our group are fully automated. The systems are equipped with 4 to 8 different channels in different sizes (10 to 500 mL*min^{-1}), each with a mass flow controller (MFC) and magnetic valves that regulate the concentration of each gas connected to the respective channel. The magnetic valves ensure that the channels are fully closed preventing unwanted gas diffusion.

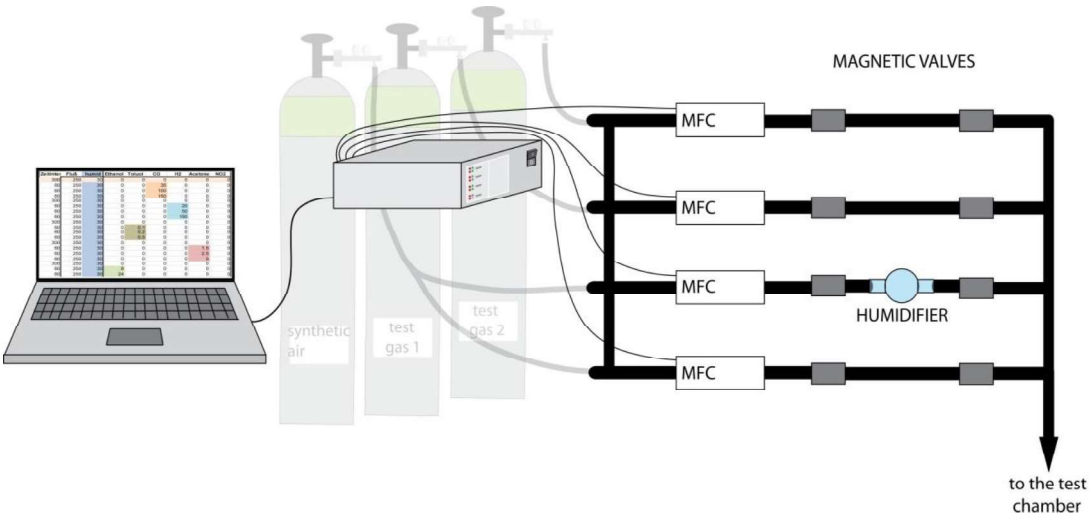

*Figure 20: schematic illustration of the fully automated gas maxing system including the mass flow controllers, magnetic valves, and the humidifier. The MFCs vary in channel size between 10 and 500 mL*min^{-1}.*

Synthetic air is used as a background gas that can be humidified by pushing the dry air stream through a humidifier filled with deionized water which results in a gas stream with 100 % r.h. By regulating the voltage of the MFCs, the amount of the respective gas that is added to the overall gas flow is controlled: The higher the voltage, the more the channel opens and the higher the amount of the respective gas. Each channel is controlled separately which results in a fully controllable gas mixture. A schematic illustration of the setup of the computer-controlled gas mixing system can be found in *Figure **20***. With the help of the different channel sizes combined with different concentrations of the test gas bottles (test gas is diluted in synthetic air to reach concentrations in the ppm range), it is possible to achieve a wide range of target gas concentrations.

All gases were supplied by Westfalen AG, Münster, Germany. The purity of the background gases synthetic air and nitrogen was 99.999 % and 99.9999 %, respectively. The target gases were delivered including a certificate with a detailed analysis listing the impurities. Deionized water was used from the building's supply system, heavy water was purchased from Sigma Aldrich (99,9 %).

4.2.3. DC Resistance Measurements

The sensors are placed in a gas-tight Teflon chamber connected to an electrometer (Keithley 617) and a power supply used to set the operation temperature. The gas flow is controlled with the help of a fully automated gas mixing system (see section 4.2.2.). The pressure in the measuring chamber is slightly above normal pressure and at a constant flow rate.

To calculate the sensor signal, one needs the baseline resistance and the resistance when exposed to the target gas. Depending on the type of material and the type of gas, this equation changes. If you have an n-type semiconductor that is exposed to a reducing gas like CO, equation 8 is used to calculate the sensor signal. This is also the equation to calculate the sensor signal for a p-type semiconductor that is exposed to an oxidizing gas. The reverse relation is used for n-type semiconductors exposed to oxidizing gases, and p-type semiconductors exposed to reducing gases (equation 9). This way, sensor signals always have values of 1 and bigger.

$$Sensor\ Signal = \frac{R_b}{R_{tg}} \geq 1 \quad (8)$$

$$Sensor\ Signal = \frac{R_{tg}}{R_b} \geq 1 \quad (9)$$

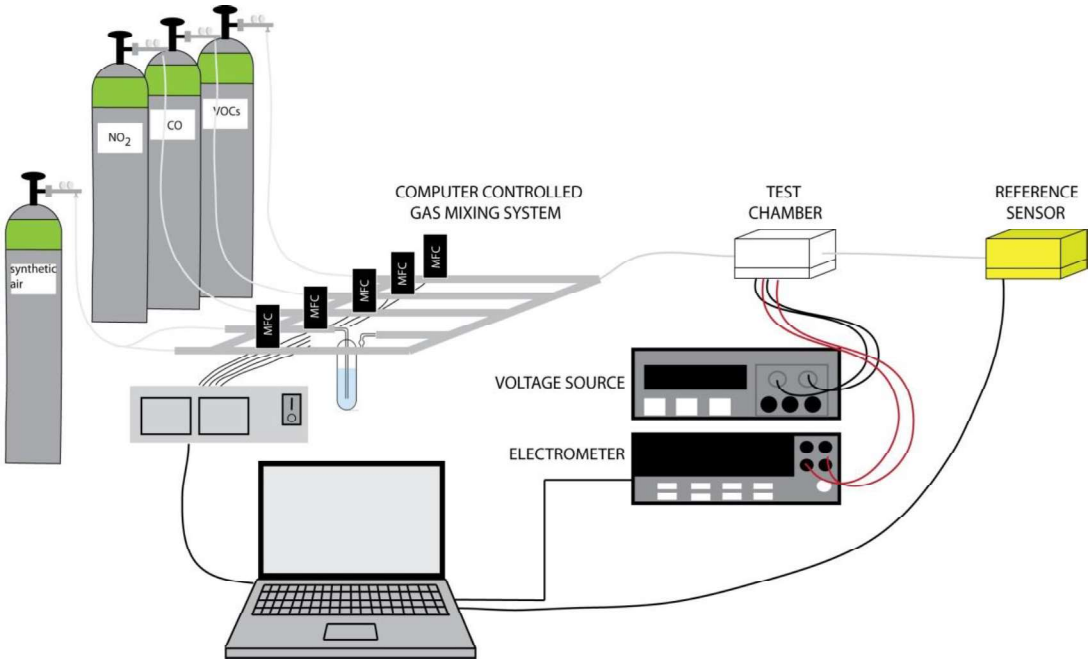

Figure 21: schematic illustration of a setup used for DC resistance measurements with a computer-controlled gas mixing system, a voltage supply to heat the sensors and an electrometer (or multimeter) for the readout, and a reference sensor after the gas tight Teflon chamber, where the sensors are placed in.

4.2.4. Diffuse Reflectance Infrared Fourier Transform Spectroscopy

For in-operando DRIFT spectroscopy, the sensors are placed in a gas-tight test chamber that was positioned in the center of a commercial optic setup with six mirrors (Harrick Praying Mantis diffuse reflectance accessory). The gas-tight gas chamber was equipped with a KBr window where the radiation could pass through without any interference in the wavenumber range of interest. Additionally, the chamber was equipped with electrical connectors for the resistance readout and temperature control as well as a gas inlet and outlet to ensure a constant and controlled gas flow. The spectrometer was an

evacuated Vertex80v with a nitrogen-cooled broad-band MCT detector (mercury cadmium telluride). The single channel spectra were continuously recorded every 15 mins with a resolution of 4 cm^{-1} and an average of 1024 scans.

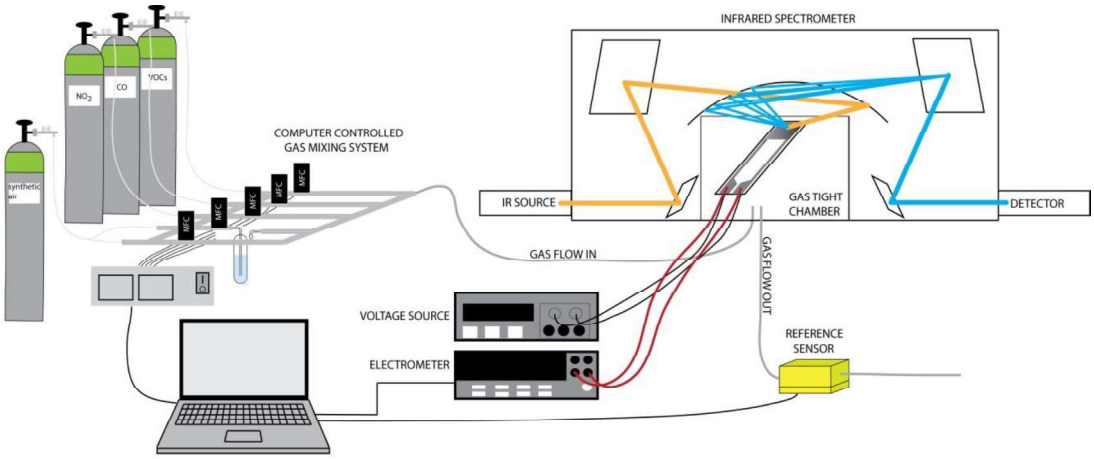

Figure 22: schematic illustration of the diffuse reflectance infrared Fourier transform spectroscopy setup including the fully automated gas mixing system.

If not otherwise indicated in the respective sections, the spectra were evaluated after equation 10, where A is the absorption. The explanation for the respective single channel spectra can be found in *Figure **23***.

$$A = -log\left(\frac{single\ channel\ in\ target\ gas}{single\ channel\ in\ background\ gas}\right) \qquad \textbf{10}$$

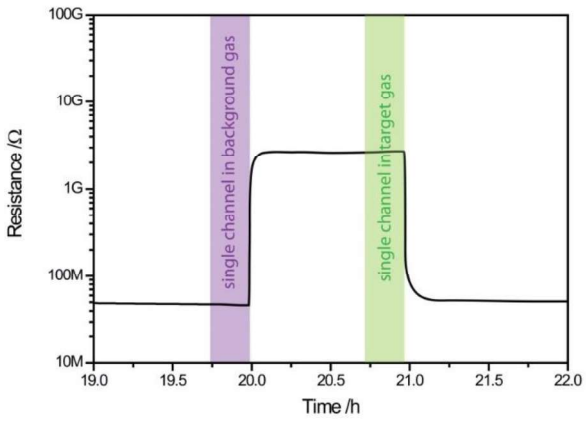

Figure 23: Schematic illustration in support of the explanation for the evaluation of the DRIFT spectra.

4.2.5. Work Function Measurements

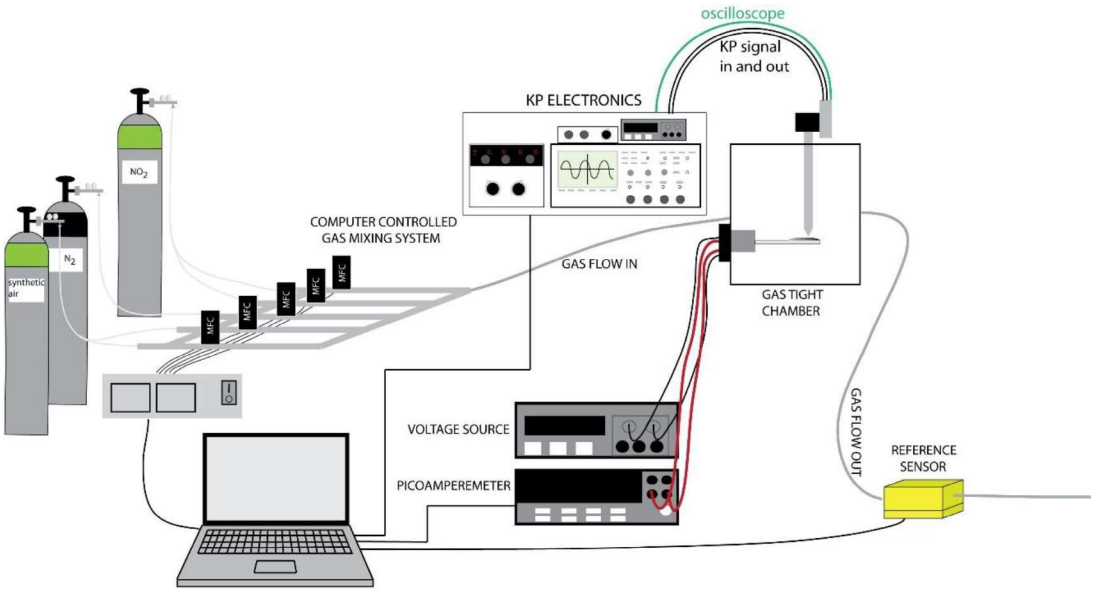

Figure 24: Schematic illustration of the Kelvin Probe setup used for in-operando work function measurements while simultaneously measuring the sensor's resistance at controlled temperatures.

As for the other in-operando measurement setups, the sensor is placed in a gas tight test chamber that is connected to a fully computer-controlled gas mixing system. The gas bottles are connected to multiple channels with different sizes in order to allow for a higher range of gas concentrations in one experiment. This way, it is possible to measure the effect of O_2 in N_2 from concentrations as low as 0.1 % to 20.5 % O_2 with one gas bottle. The same principle allowed to measure NO_2 concentrations from 50 ppb to 7 ppm in synthetic air. The sensor is connected to a voltage source as well as to a resistance measurement device, in this case a picoamperemeter. The sensor is positioned horizontally and close to the metallic Kelvin Probe tip (roughly 100 µm), which is connected to a sine wave generator. The sine wave generator is connected to a coil which is able to magnetically create the oscillation of the KP tip. The raw signal of the KP is checked with an oscilloscope. An additional voltage source is connected to the Kelvin Probe setup as backing potential.

We measure in the non-locking KP mode where the backing potential is varied in much higher ranges than is expected for the CPD. By measuring the amplitude at different

voltages and linear interpolation, the backing potential can be determined for which the current is zero.

4.2.6. XAS

The XANES data was recorded at beamline ID26 at the European Synchrotron Radiation Facility (ESRF) in Grénoble, France. A Si(111) double crystal monochromator was used to select the incident energy which covered an area of 0.2 x 0.5 mm^2 on the sensor's surface. The energy calibration was done with the help of the Pt foil. The data was recorded with the help of a high-energy-resolution fluorescence detector at the Pt L_3-edge. The setup was arranged in the vertical Rowland geometry.

The sensor was placed in a homemade gas tight chamber that allowed for the simultaneous measurement of the sensor's resistance while it was heated to a controlled temperature. The chamber was connected to a computer-controlled gas mixing system which allowed for measurements under controlled conditions. The spectra were evaluated with Athena and Arthemis software of the IFEFFIT package (energy calibration, background subtraction, normalization).

4.2.7. XPS

The samples were prepared via spin coating on 10 x 10 mm^2 gold-coated silicon wafers. The wafers were mounted on a sample holder and introduced in the ultra-high vacuum. The measurement was done with a Phoibos 100 analyzer, a 1d Delay Line detector from SPECS and an XR-50 m X-ray source with an Al/Mg anode. The measurement was performed using the Al anode. The spectra were referenced to the C 1s line at 285 eV using the data evaluation tool Unifit2018.

5. Results and Discussion

5.1. WO_3 and the Influence of Pt as Surface Additive

5.1.1. Basic Characterization

The samples (pristine WO_3 and WO_3 with either 0.1 wt% Pt or 0.2 wt% Pt) were investigated with SEM, XRD and Raman spectroscopy in order to get information on the structure of the samples loaded with Pt. The data was already summarized and briefly discussed in section 2.2 since the data was already presented in my Master's Thesis [59]. The Raman spectra and XRD data did not indicate the presence of Pt. The SEM images showed, however, that Pt was present as surface clusters with a maximum diameter of 10 nm (Figure 7). An influence on the crystal structure or morphology of the WO_3 grains was not observed.

The electronic effect of CO, acetone, toluene, and ethanol was screened at 75 °C (*Figure **8***). It was found that the presence of Pt significantly enhanced the response to CO and ethanol. In some capacity this also appeared to be a selective effect because the response to acetone and toluene was not enhanced. The sensing mechanism of CO was investigated closer with the help of DRIFT spectroscopy and XAS.

5.1.2. CO Sensing Mechanism with Pristine WO_3

The sensing mechanism with CO of pristine WO_3 and Pt-loaded WO_3 was closely investigated with the help of simultaneous DC resistance measurement and recording of DRIFT spectra. Each sensor was operated at 75 °C and was exposed to different concentrations between 25 and 500 ppm ^{12}CO followed by an exchange with 500 ppm ^{13}CO. These experiments were conducted both in a dry background and in 10 % r.h. The results for pristine WO_3 are shown in *Figure **25*** and *Figure **26***. CO is generally considered to be a reducing gas which would result in a decrease in resistance with WO_3 as sensing material with WO_3 being an n-type material. Therefore, the observed increase in resistance with low CO concentrations both in dry and humid conditions was unexpected.

The DRIFT spectra in dry conditions showed an increase in W-O bonds (increasing bands at 2064 and 1862 cm^{-1}, black and red lines in the right part of *Figure **25*** and *Figure **26***) in the presence of 25 and 50 ppm CO. Additionally, the formation of CO_2 is indicated by the small increasing double band centered at 2346 cm^{-1}. When the concentration was increased to 100 ppm, none of these bands could be observed anymore (blue line, right graph, *Figure **25***) and started to decrease when the CO concentration further increased (green and magenta, right graph, *Figure **25***). The exchange experiment with ^{13}CO resulted in the shift of the band at 2096 cm^{-1} (100 – 500 ppm CO) to 2044 cm^{-1} indicating that this band is related to a carbonyl species. However, this carbonyl can be assigned to a Pt^0–carbonyl on the Pt–electrodes used for the electrical readout. It could be possible that the electrodes promote the reaction of CO with lattice oxygen at the interface between the sensing material and the electrodes. However, the formation of CO_2 is not observed when the Pt^0-carbonyl is observed indicating that the carbonyl does not play a significant role.

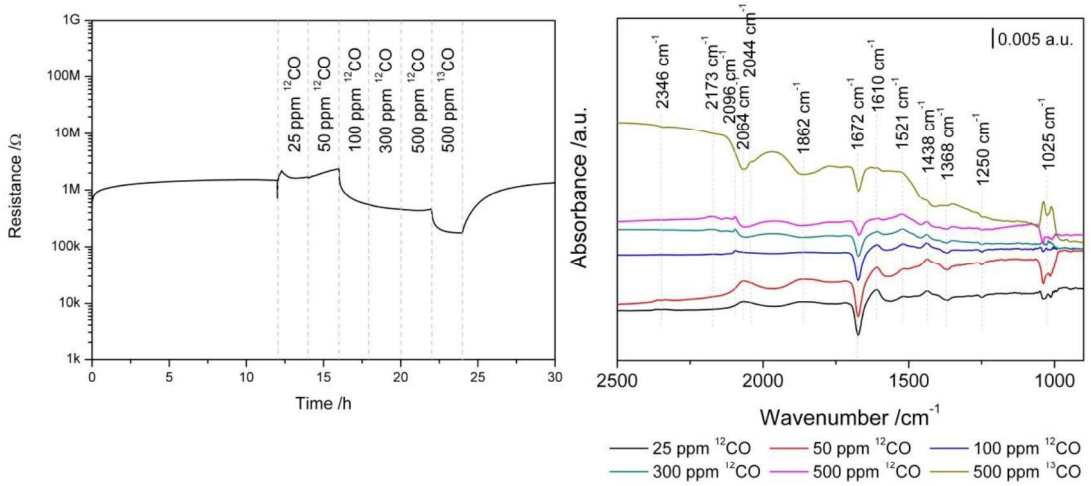

Figure 25: left: DC resistance measurement of pristine WO_3 during the exposure to different concentrations of ^{12}CO and the exchange with ^{13}CO in dry synthetic air. Right: simultaneously recorded DRIFT spectra showing the change in surface chemistry for each respective concentration.

At 1672 cm^{-1}, a sharp decreasing band is observed for all CO concentrations. As of yet, it is not clear what this band is related to. It could be related to a water species that is replaced or changed due to the reaction with CO. However, it appears that this part of the reaction is not responsible for the electrical effect that is observed (see discussion for CO sensing mechanism in humid conditions below).

In humid conditions, the behavior of the W-O related bands appears to be comparable to the behavior in dry conditions. The bands at 2064 and 1862 cm^{-1} assigned to W-O single bonds increase in 25 and 50 ppm and decrease when the CO concentration is 100 ppm and above. The interpretation of the band at 1025 cm^{-1} which is assigned to W=O double bonds is difficult in humid conditions due to a sharp drop in the absorbance in the same range. The band at 1415 cm^{-1} behaves in the same way as the bands assigned to W-O single bonds and is therefore assigned to a W-O single bond as well. The band at 1615 cm^{-1} is assigned to water intercalated in the WO_3 lattice.

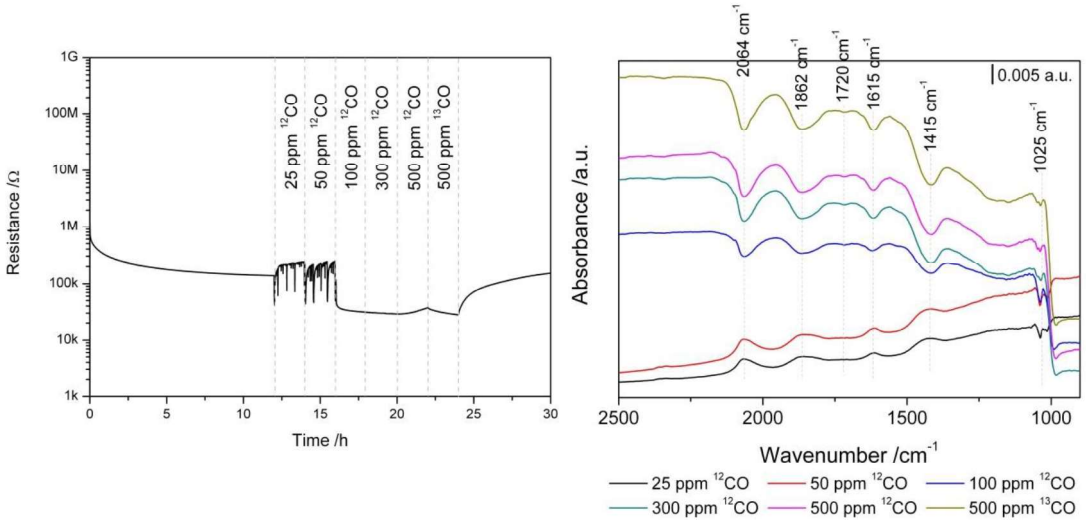

Figure 26: left: DC resistance measurement of pristine WO_3 during the exposure to different concentrations of ^{12}CO and the exchange with ^{13}CO in 10 % r.h. Right: simultaneously recorded DRIFT spectra showing the change in surface groups for each respective concentration.

In contrast to the experiment in dry conditions, in humid conditions neither the band at 1670 cm^{-1} nor the Pt^0–carbonyl band is observed. However, the electronic effect of CO in both background conditions is very similar. This indicates that these bands are not playing a significant role in the reaction that results in the observed change in resistance. The behavior of the W-O bands strongly indicates their major contribution to the resistance. When the bands at 2064, 1862 and 1415 cm^{-1} are increasing, the resistance increases. When these bands decrease, the resistance decreases. The main question now is, how it is possible that the W-O bands are increasing when CO is oxidized to CO_2 (indicated by the increasing band at 2346 cm^{-1}). A possible explanation was given by Jin et al. who with the

help of DFT calculations concluded that molecular oxygen adsorbs in an oxygen vacancy on the defective surface of WO_3 and even showed that the subsequent reaction with CO could result in the oxidation of WO_3 (*Figure* ***27***)[111].

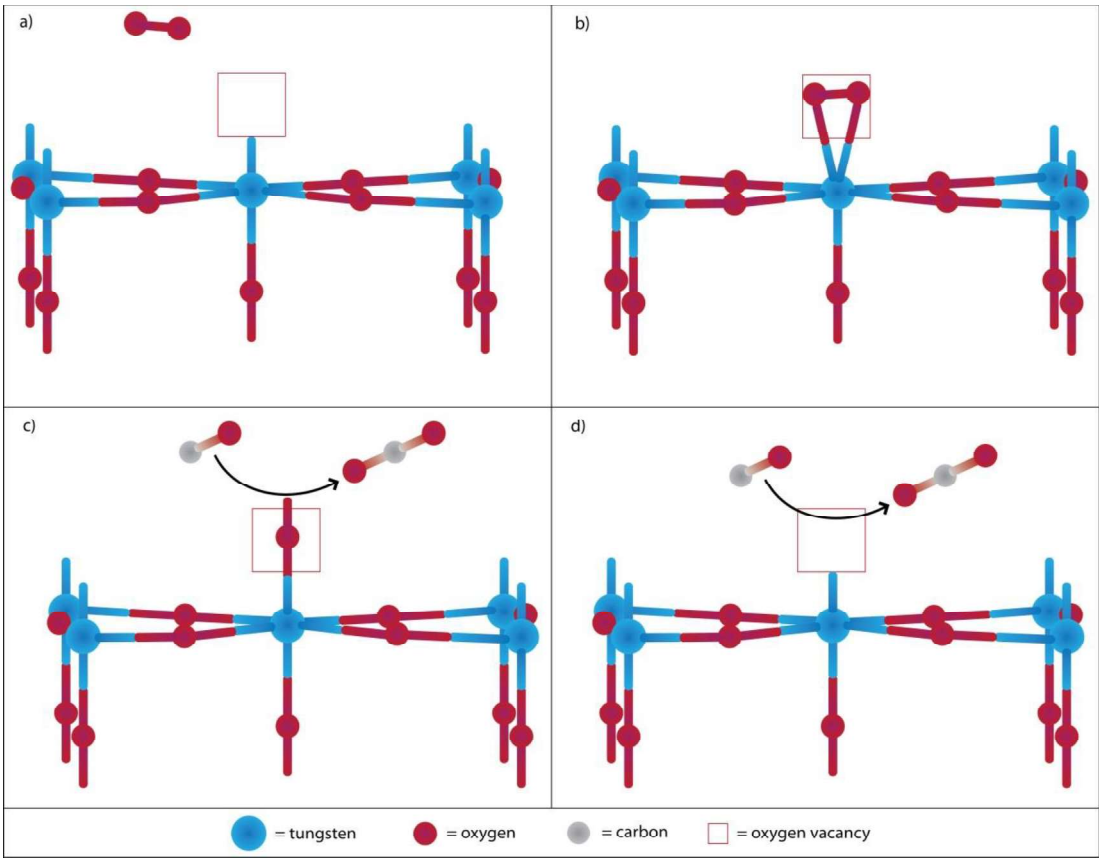

Figure 27: Schematic illustration of a) a defective WO_3 surface, b) a defective WO_3 surface with an O_2 – molecule in the vacancy, c) the reaction with low concentrations of CO and the O_2 – molecule in the vacancy, and d) the reaction at higher CO concentrations with the previously healed oxygen vacancy under reformation of a vacancy. After [111].

In more detail, molecular oxygen can adsorb parallel to the surface in the oxygen vacancy (*Figure* ***27***b). In the presence of low CO concentrations, the adsorbed oxygen molecule will react with CO to form CO_2 while the other oxygen atom will heal the oxygen vacancies (*Figure* ***27***c). With further increasing CO concentrations, CO reacts with the oxygen in the now healed vacancy to reform the oxygen vacancy (*Figure* ***27***d). The healing of the vacancy described in *Figure* ***27***c results in an increase of the resistance while the reformation of the vacancy described in *Figure* ***27***d results in a decrease of the resistance. This can also be observed in the DRIFT spectra where in low CO concentrations the

amount of W-O bonds at the surface increases, and in higher CO concentrations decreases.

In conclusion, it was possible to explain the surprising response of pristine WO_3 at 75 °C with the help of the data obtained with DRIFT spectroscopy. At low temperatures, a small amount of a per oxo species exists at the surface of WO_3. This species is very reactive and can form CO_2 in the presence of CO while healing oxygen vacancies at the surface at the same time which is observed as oxidation. With increasing concentrations of CO, the reaction to CO_2 uses lattice oxygen resulting in the reduction of the surface.

5.1.3. CO Sensing Mechanism with WO_3 Loaded with Pt

5.1.3.1. WO_3 Loaded with 0.1 wt% Pt

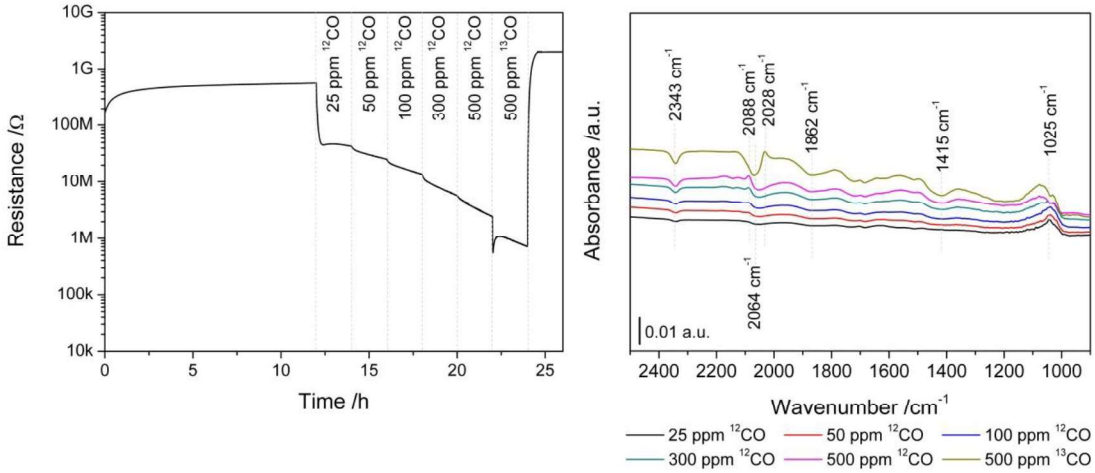

Figure 28: left: DC resistance measurement of WO_3 loaded with 0.1 wt% Pt operated at 75 °C during the exposure to different concentrations of ^{12}CO and the exchange with ^{13}CO in dry synthetic air. Right: simultaneously recorded DRIFT spectra showing the change in surface chemistry for each respective concentration.

The response of WO_3 loaded with 0.1 wt% Pt to CO is significantly different than the response of pristine WO_3. Firstly, the change in resistance is a lot stronger than for pristine WO_3. Additionally, the behavior is as expected for an n-type semiconductor in the presence of the reducing gas CO. However, how does the presence of Pt influence the sensing mechanism? In order to answer that question, DRIFT spectroscopy was done on the material while simultaneously measuring the DC resistance. In addition, the samples were investigated using in-operando XAS.

*Figure **28*** shows the DC resistance measurement of a sensor based on WO_3 loaded with 0.1 wt% Pt (left) and the simultaneously recorded DRIFT spectra. Comparing these graphs with the graphs in *Figure **25***, a significant difference in behavior becomes obvious. While the pristine WO_3 showed only small changes in resistance due to the exposure to CO, WO_3 loaded with 0.1 wt% Pt showed distinguishable steps for each CO concentration change. A comparable trend can be observed in the DRIFT spectra. The bands assigned to W-O single bonds are decreasing (2064, 1862 and 1415 cm^{-1}). The strongly decreasing band at 2364 cm^{-1} is commonly assigned to carbon contamination in the material. Additionally, a sharp increasing band at 2088 cm^{-1} is observed for all ^{12}CO concentrations that shifts to 2028 cm^{-1} when exposed to ^{13}CO. This band is assigned to a Pt-carbonyl. The fact that this band is positioned below 2100 cm^{-1} indicates that the Pt clusters at the surface are metallic. If the band were positioned above 2100 cm^{-1}, this would indicate an oxidized state of Pt.

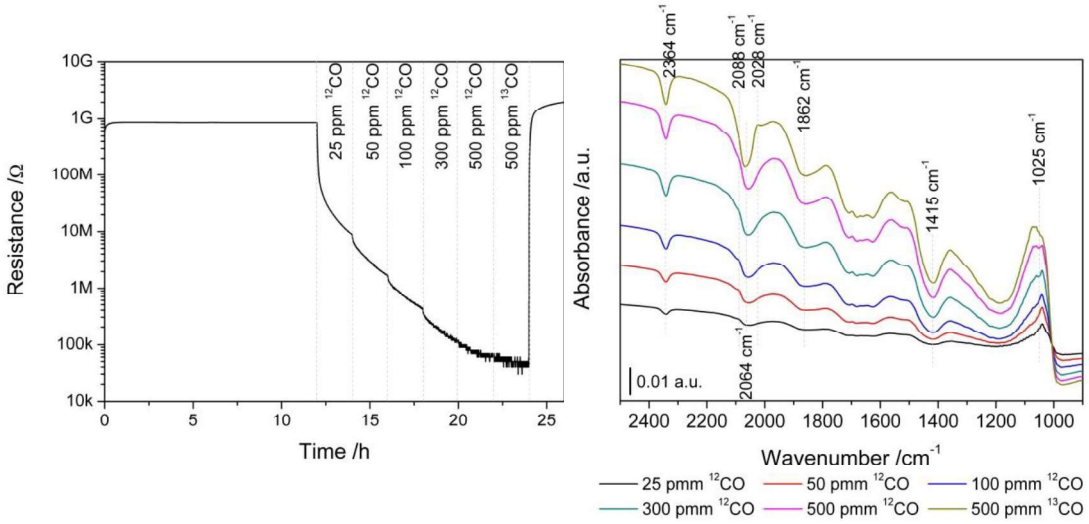

Figure 29: left: DC resistance measurement of WO_3 loaded with 0.1 wt% Pt operated at 75 °C during the exposure to different concentrations of ^{12}CO and the exchange with ^{13}CO in 10 % r.h. Right: simultaneously recorded DRIFT spectra showing the change in surface chemistry for each respective concentration.

In humid conditions, the spectra show a very similar situation, though much stronger pronounced. The sensor signal to 500 ppm CO in 10 % r.h. is roughly 12,000. This is about a factor 50 higher than the response in dry conditions to the same CO concentration. This trend can also be observed in the DRIFT spectra. The decrease in the W-O single bonds

(2064, 1862 and 1415 cm^{-1}) is a lot more pronounced than in dry conditions, which explains the bigger change in resistance. The DRIFT spectra, however, do not deliver an explanation as to why the response in humid conditions is much stronger.

5.1.3.1.1. XAS

The data obtained by simultaneously measuring the DC resistance and recording DRIFTS spectra indicated a spillover mechanism where CO adsorbed at the surface of the Pt-clusters and subsequently migrated to the base material where CO reacted with lattice oxygen to produce CO_2. At the European Synchrotron Radiation Facility (ESRF) in Grénoble, France, it is possible to do *in-operando* XAS measurements which helps support the suggested sensing mechanism. This means it is possible to monitor the change in oxidation state of the surface elements while exposing sensors to target gases at operation conditions (at 75 °C, ambient pressure). The absorption spectra were recorded at the Pt L_3–edge.

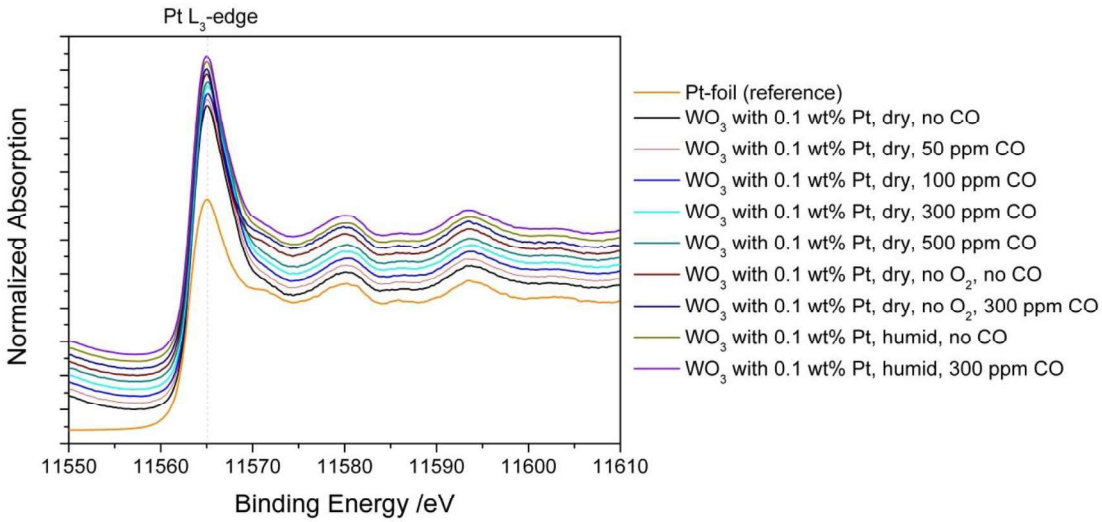

Figure 30: Absorption spectra at the Pt L_3-edge of a reference Pt foil (metallic) and WO_3 loaded with 0.1 wt% Pt in different backgrounds and in the presence of different CO concentrations.

As a reference, the absorption spectrum of a Pt foil (metallic) was recorded. Due to timing reasons, only the WO_3 sample loaded with 0.1 wt% Pt was measured at the ESRF. The sample was kept in different backgrounds (dry and humid backgrounds in the presence of O_2, and an inert background without O_2 or humidity) and exposed to different

concentrations of CO. *Figure* ***30*** shows that the gases present in the atmosphere had no clearly distinguishable effect on the oxidation state of Pt. It is also observed that the Pt clusters were metallic right from the beginning. This indicates that the sensitization mechanism cannot be based on an electronic effect like it would be the case in a Fermi-level pinning mechanism which is often observed in surface loaded materials [8,112]. If it were based on the Fermi-level pinning mechanism, one would have to be able to observe a change in the absorption edge since oxidized Pt shows a higher binding energy of core-level electrons.

5.1.3.2. WO_3 Loaded with 0.2 wt% Pt

Figure ***31*** and *Figure* ***32*** show the DC resistance and the respective DRIFT spectra of the sample loaded with 0.2 wt% Pt in dry and humid conditions. The results are very comparable to the results obtained with the sample loaded with 0.1 wt% Pt.

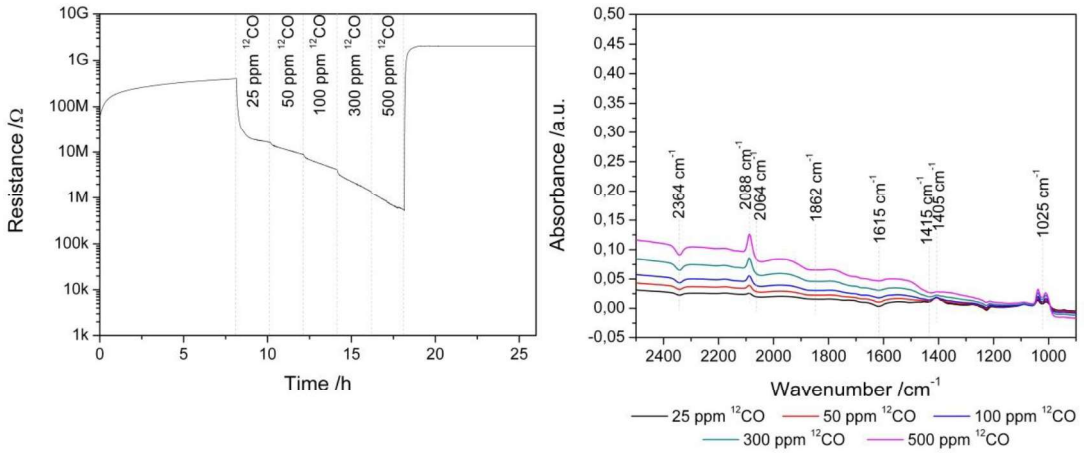

Figure 31: left: DC resistance measurement of WO_3 loaded with 0.1 wt% Pt operated at 75 °C during the exposure to different concentrations of ^{12}CO and the exchange with ^{13}CO in dry synthetic air. Right: simultaneously recorded DRIFT spectra showing the change in surface chemistry for each respective concentration.

In dry conditions, the DRIFT spectra show a strong increasing band at 2088 cm^{-1} that can be assigned to the formation of Pt^0-CO. Slightly decreasing bands at 2064, 1862 and 1415 cm^{-1} are observed that are assigned to W-O bonds at the surface. The decreasing band at 2364 cm^{-1} is correlated to carbon contamination of the material. The decreasing band at 1615 cm^{-1} is assigned to intercalated water. The increasing double band centered at 1025 cm^{-1} shows an increase in W=O double bonds.

As for the sample with the lower amount of Pt at the surface, the response is stronger in humid conditions. This is reflected in the DRIFT spectra. Excitingly, the band that can be assigned to Pt^0-CO is again less strongly pronounced while the decrease in W-O bands is pronounced stronger in humid conditions. It appears that while the formation of the Pt^0-CO is necessary as an intermediate step for the reaction with the base material, the presence of water significantly enhances the reaction between the carbonyl and the lattice oxygen of the base material which results in a significantly stronger response of the sensor.

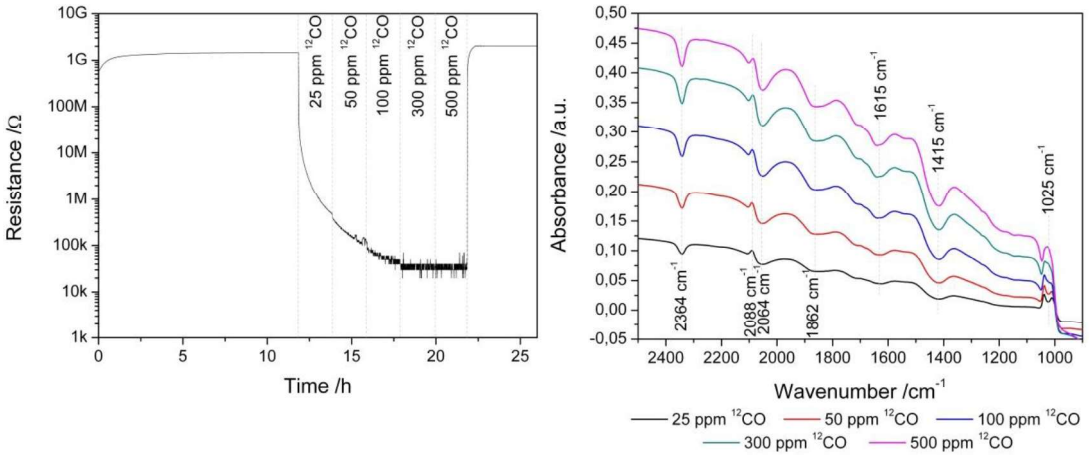

Figure 32: left: DC resistance measurement of WO_3 loaded with 0.1 wt% Pt operated at 75 °C during the exposure to different concentrations of ^{12}CO and the exchange with ^{13}CO in 10 % r.h. Right: simultaneously recorded DRIFT spectra showing the change in surface chemistry for each respective concentration.

5.1.3.3. Conclusion

In conclusion, the sensing mechanism to CO of WO_3 loaded with Pt is expected to be based on a spillover mechanism (*Figure **33***). CO is adsorbed on the Pt surface clusters where CO is activated and migrates to the interface between the surface cluster and the base material. Then, it reacts with lattice oxygen of the base material to form CO_2 under the reduction of the base material which is observed as a decrease in resistance of the sensor.

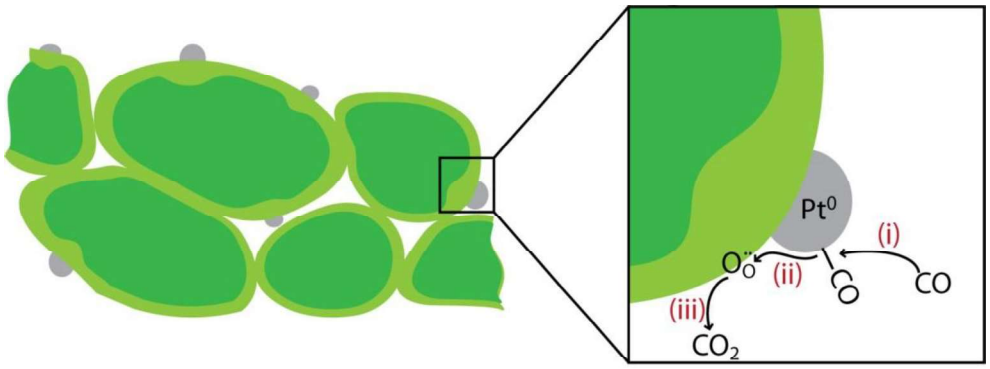

Figure 33: schematic illustration of the spillover mechanism of the Pt loaded WO_3 sample investigated here in this work. (i) CO adsorbs at the surface of the Pt^0-cluster. (ii) The carbonyl migrates to the interface with the base material WO_3. (iii) Carbonyl reacts with lattice oxygen to form CO_2 under the reduction of the base material.

5.2. PbS

5.2.1. Basic Characterization

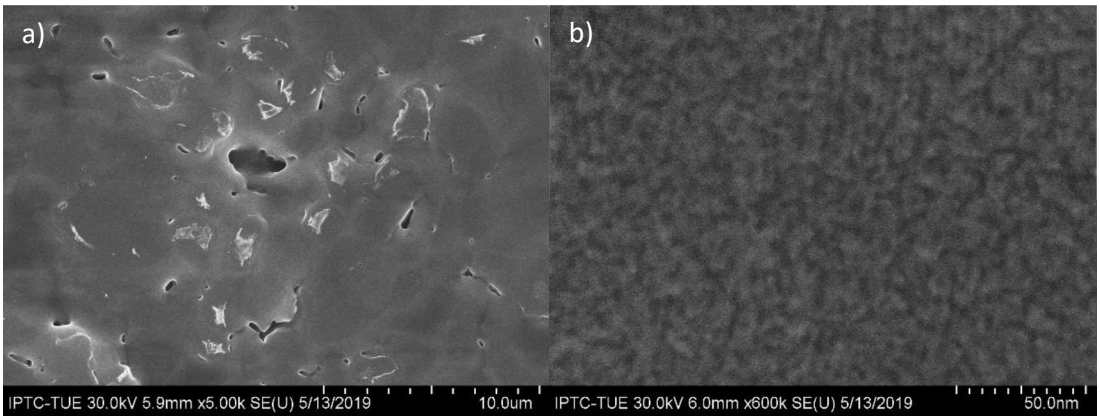

Figure 34: SEM images of a freshly prepared sensor at a 5000 – (a) and 600,000 – (b) fold magnification showing the porous surface consisting of quantum dots of the size of roughly 5 nm in diameter.

The basic characterization of the samples was conducted on the sensor substrate to get as much information as possible on the sensing device after the material underwent the sensor production process.

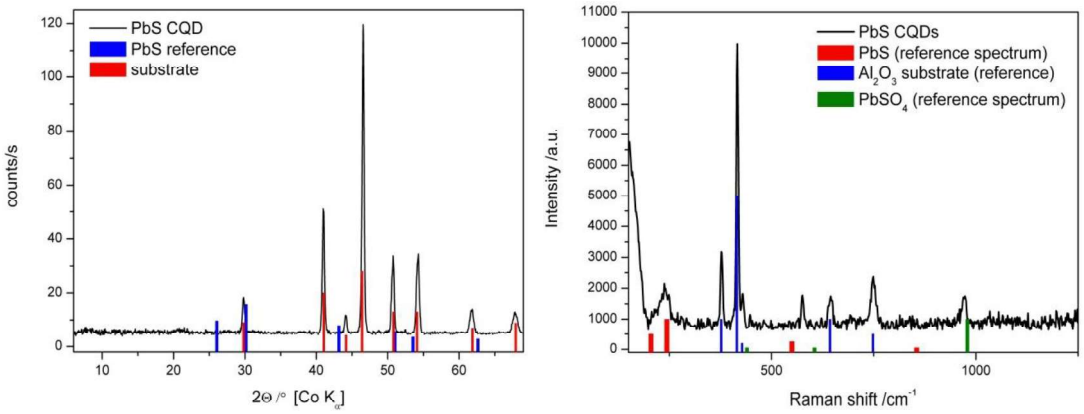

Figure 35: XRD pattern (left) and Raman spectrum (right) of the freshly prepared sensor device showing mostly reflexes and signals that can be assigned to the substrate consisting of Al_2O_3.

Figure ***34*** shows SEM images of the surface of a freshly prepared sensor in two different magnifications. The image recorded with a low magnification shows a mostly homogeneous surface with only a few irregularities. The image taken with a 600k-fold

magnification confirms the high regularity at the surface. The high regularity is a result of highly ordered colloidal quantum dots with a diameter of roughly 4 nm on average.

Additionally, XRD and Raman spectroscopy were done on the sensors. The results can be found in *Figure **35***. Due to the low layer thickness and the small size of the quantum dots, it was not possible to see any reflexes in the XRD pattern that could be assigned to PbS. With Raman spectroscopy, small signals correlated to PbS were observed at 205 and 244 cm^{-1}. The band at 979 cm^{-1} is assigned to $PbSO_4$. The presence of $PbSO_4$ in the fresh sample was confirmed by XPS (Figure 36).

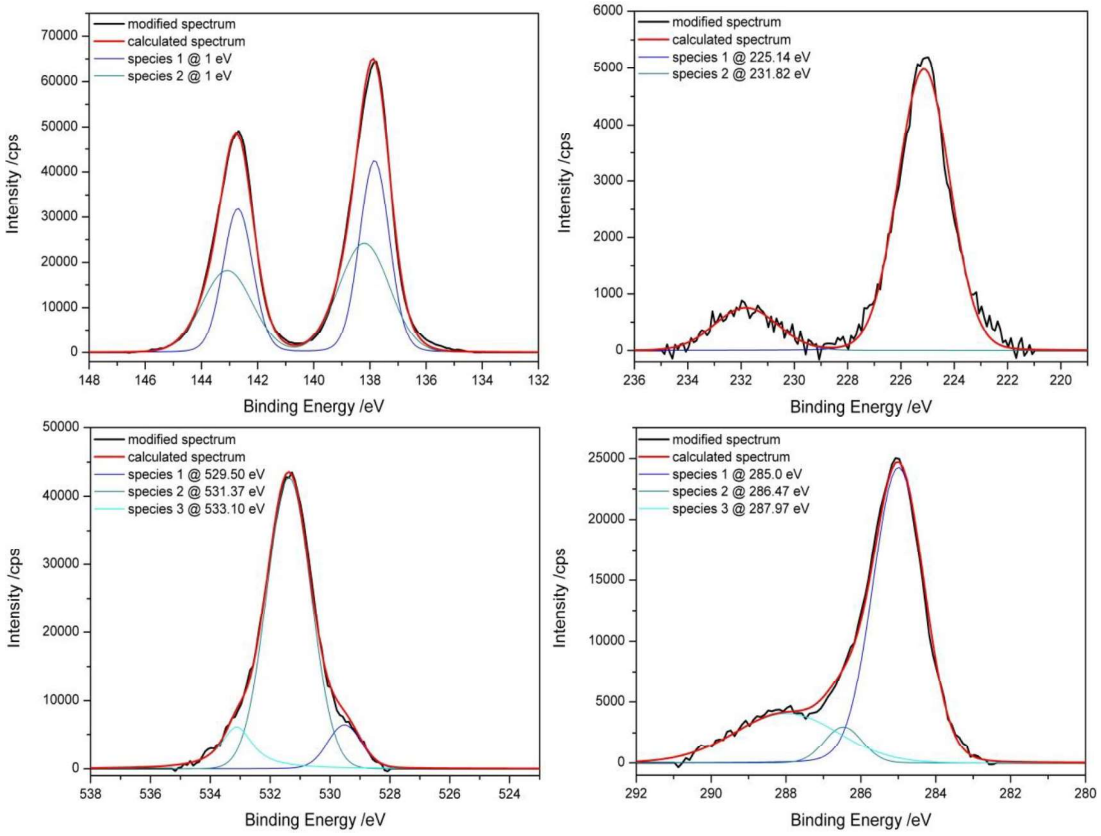

Figure 36: Detail spectra of different ranges of fresh PbS recorded on a Si-Au waver: a) Pb 4f, b) S 2s, c) O 1s, d) C 1s. From [110].

The detail spectra of the freshly prepared PbS shows the presence of multiple components. The Pb 4f spectra shows two components – one at 137.6 eV and one at 138.2 eV. The former component is assigned to PbS while the latter is a mixture or PbO, $PbCO_3$ and $Pb(OH)_2$. The S 2s detail spectrum shows two components as well – one at 225.15 eV and one at 231.8 eV. The former can be assigned to PbS again. The latter,

however, shows the presence of $PbSO_4$. On the one hand, this confirms the finding of the Raman spectrum. On the other hand, the Pb 4f detail spectrum did not show the presence of $PbSO_4$. The binding energy of $PbSO_4$ in the Pb 4f region would be expected at 139.5 eV. The O 1s detail spectrum showed three components – one at 529.5 eV, one at 531.4 eV and one at 533.1 eV. The component at 531.4 eV is by far the most intensive one and can be assigned to a mixture of $PbCO_3$, PbO and $PbSO_4$. The component at the lower binding energy is assigned to PbO as well, while the component at 533.1 eV is assigned to $Pb(OH)_2$ and adsorbed H_2O. The XPS data confirms the observation of the Raman spectra. The fresh sample is already oxidized to some extent. $PbSO_4$ was not observed in the Pb 4f detail spectrum, but in the S 2s detail spectrum. The O 1s spectrum could not help further in confirming the presence of $PbSO_4$ due to an overlap of the binding energies found in PbO and $PbCO_3$ which was clearly observed in the Pb 4f detail spectrum.

5.2.2. The Effect of the Sensor Preparation on the Electronic Measurements

The standard method for the preparation of sensors in our lab is screen printing. However, this method was not suitable in this case because the CQDs had to undergo a ligand exchange procedure to remove the organic ligand at the surface. In screen printed layers, this would have been a problem because the layers are roughly 50 µm and a successful exchange throughout the layer could not be ensured. Therefore, alternative methods were explored: dip coating, drop coating (both *Figure **37***) and spin coating (Figure 19).

For dip coating, the sensor was dipped into a dispersion of PbS CQDs in octane with a concentration of 50 $mg*mL^{-1}$ for 25 s (*Figure **37***, 1a). The sensor was given 10 s to dry before the sensor was dipped into an exchange solution. The exchange was done by dipping the sensor in a 10 $mg*mL^{-1}$ solution of $NaNO_2$ in MeOH for another 15 s (*Figure **37***, 2.). The layer was washed by dipping the sensor in MeOH for 15 s (*Figure **37***, 3.). These three steps were repeated a second time. This was followed by another two rounds of dip coating; however, the ligand exchange was now executed in an NH_4Cl solution in MeOH (10 $mg*mL^{-1}$).

For drop coating, one drop of the PbS dispersion was applied on the substrate. The drop was given 10 s to dry before it was dipped into the exchange solution. As for the dip coated sensors, a $NaNO_2$-solution was used for the first two rounds of ligand exchange, and an NH_4Cl-solution was used for the third and fourth round. A third batch of sensors was prepared with the help of spin coating as was described in section 4.1.4.

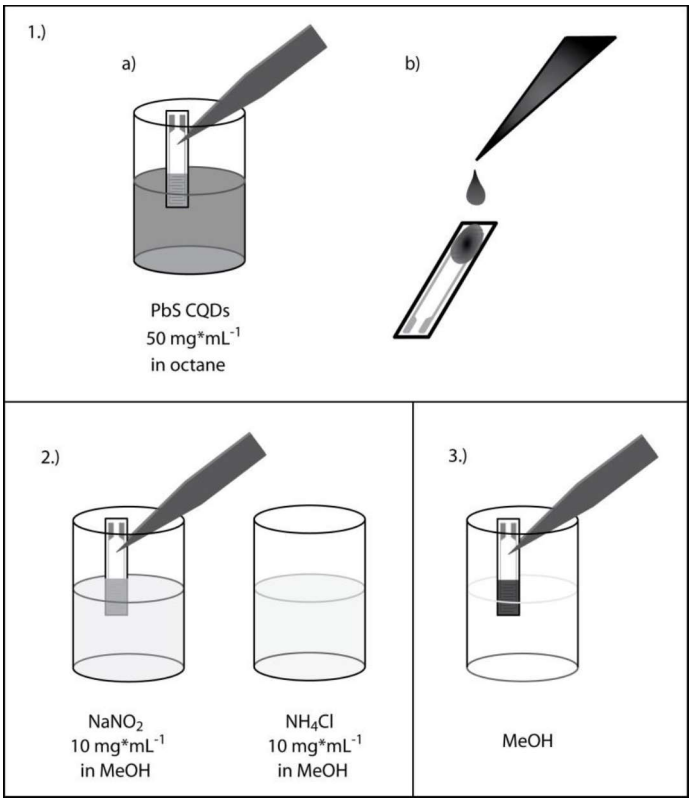

Figure 37: Schematic illustration of the sensor preparation via dip coating and drop coating. For dip coating, the cleaned substrate was dipped into a dispersion of PbS in MeOH for 25 s (1a). After giving the sensor 10 s to dry, it was dipped into the exchange solution for 45 s (2.) and washed in MeOH for 15 s (3.). These three steps for repeated a second time. For drop coating, one drop of the dispersion was applied on the substrate (1b.). The sensor was given 10 s to dry before it was dipped in the exchange solution for 45 s (2.) and washed with MeOH for 15 s (3.). These steps were repeated four times in total.

The results of the electrical measurements are shown in *Figure **38***. The left graph in the figure shows the data of two drop coated sensors that were prepared at the same time with the same solutions/dispersion and were simultaneously measured in the same system. Although the sensors were prepared at the same time, the results are significantly different. Measurements like this with drop coated sensors were no rarity and it was

concluded that drop coating was not a suitable method for the sensor preparation. The results obtained with dip coated sensors (*Figure **38***, right) show a sharp decrease in resistance when the sensors are initially exposed to NO_2. However, the resistance increases rapidly after the initial drop and stabilizes at a baseline significantly higher than in the beginning. Additionally, the sensors do not respond to NO_2 anymore starting with the second exposure. These results indicate that even though the results are reproducible, dip coating does not result in devices that can be investigated for their sensing abilities to NO_2.

The results obtained with spin coated sensors are shown in *Figure **38***, middle. This graph shows that sensors prepared with spin coating react reproducibly to NO_2, show comparable trends, and show nice responses to NO_2.

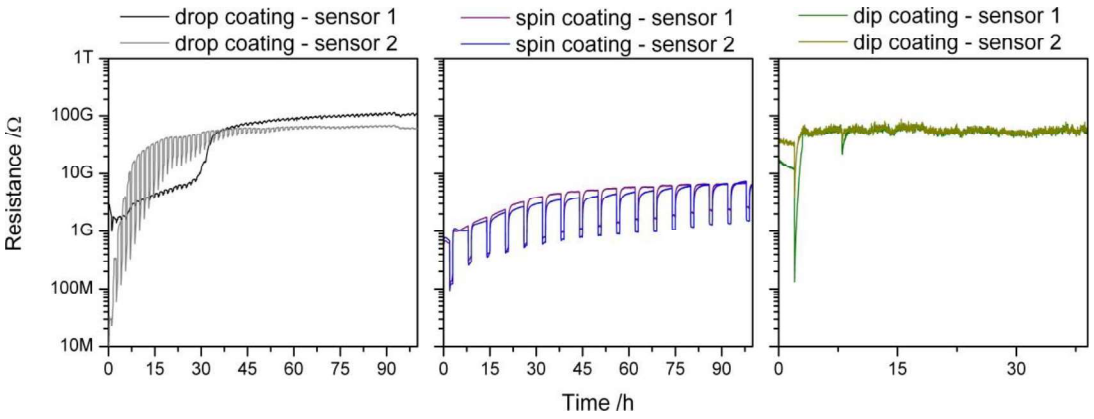

Figure 38: Comparison of the electrical results obtained with sensors prepared via drop coating (left), spin coating (center) and dip coating (right).

Based on these results, it was concluded that spin coating is the most suitable method for the preparation of sensing layers from PbS CQDs. One reason for this observation could be the higher uniformity of the spin coated layers compared to the drop and dip coated layers, also with respect to the ligand exchange. For spin coated layers, the exchange was executed layer by layer. For the drop coated sensors, the sensing layer varies strongly in layer thickness which results in varying efficiency of the ligand exchange depending on the position on the sensing layer. It is expected that the homogeneity of sensing layers prepared via dip coating is in between that of drop coated and spin coated sensors.

5.2.3. Aging Mechanism

Since it was reported that quantum dots show a quantum confinement effect, it was necessary to investigate the influence of the nanoparticle size on the sensing characteristics. This was done comparing the sensing behavior of the colloidal quantum dots to the sensing behavior of a micrometric material. Each material was spin-coated onto a substrate and underwent the ligand exchange procedure in order to exclude any influence of the preparation procedure on the sensing behavior. The sensors were operated at room temperature and repeatedly exposed to 3 ppm NO_2 in dry synthetic air. The results are shown in *Figure **39***.

Initial comparison reveals similar trends for the two materials. Both sensors show a baseline drift to a higher resistance with the biggest increase after the first exposure to NO_2. Additionally, both materials show a decrease in the sensor signal which stabilizes over time. However, the stabilization process for the bulk material took place significantly quicker than for the colloidal quantum dots. This could have multiple reasons, one of them being the difference in nanoparticle size, the other being differences in surface chemistry.

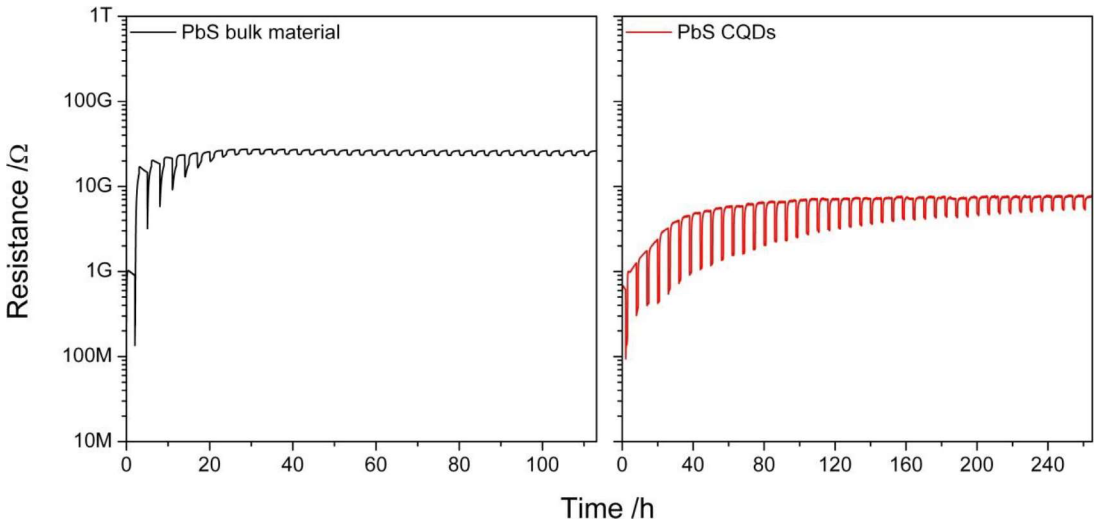

Figure 39: Comparison of the DC resistance behavior of the bulk material (left) and the CQDs (right) under repeated exposure to 3 ppm NO_2 in dry synthetic air operated at room temperature.

In order to investigate the surface chemistry of the two materials, *in-operando* DRIFT spectroscopy was conducted. The sensors were placed in the setup described in section

3.2 and repeatedly exposed to 3 ppm NO_2 in a background of dry synthetic air at room temperature. The first step was the investigation of the reason behind the increase in baseline resistance. This was done evaluating the spectra recorded in synthetic air in between the NO_2 pulses: The spectrum after a pulse was referenced to the one recorded before the pulse. This way, the changes in surface chemistry responsible for the baseline increase were revealed. Since the stabilization process for the two different PbS materials was significantly different in speed, three sections were investigated: the beginning, the middle, and the end of the stabilizing process. This is the reason why the pulses investigated for the PbS CQDs are further apart than those of the micrometric material.

*Figure **40*** shows the DC resistance measurements and the respective spectral data for the micrometric PbS based sensor (a) and the sensor based on PbS CQDs (b). While the resistance shows comparable trends of the two sensors, the spectral data looks completely different. For the micrometric material, small changing bands between 3000 and 2800 cm^{-1} are observed (both decreasing and increasing), in addition to multiple increasing bands at 1762, 1693, between 1600 and 1200 and at around 1000 cm^{-1}. 3000 to 2800 cm^{-1} is a typical range for saturated C-H and C-C vibrations [113,114]. The fact that in addition to decreasing bands also increasing bands are observed in this range indicates that saturated organics are reacting with NO_2. If only decreasing bands were observed, this would mean that the amount of organics at the surface is decreasing (organics are going away). The presence of additional increasing bands shows that the organics are not going away but instead are reacting and changing when exposed to NO_2. This is also indicated by the increasing band at 1762 cm^{-1} which is a typical wavenumber for carbonyl compounds [113]. The increasing bands between 1600 and 1200 cm^{-1} are in a range where characteristic vibrations of multiple different chemical groups are: (i) C-H and C-C vibrations and (ii) surface nitrates and nitrites [113,115]. It is known that organics are involved in the aging of the micrometric material due to the presence of the changing bands below 3000 cm^{-1}. It is likely that this is accompanied by increasing bands in the range between 1600 cm^{-1} and 1200 cm^{-1}. Since the micrometric material was commercially purchased, no precise information could be found on possible organic residuals which would have made the assignment easier. On the other hand, the

formation of nitrates and nitrites due to the exposure to NO_2 has been reported before for gas sensors based on different semiconducting materials [116,117].

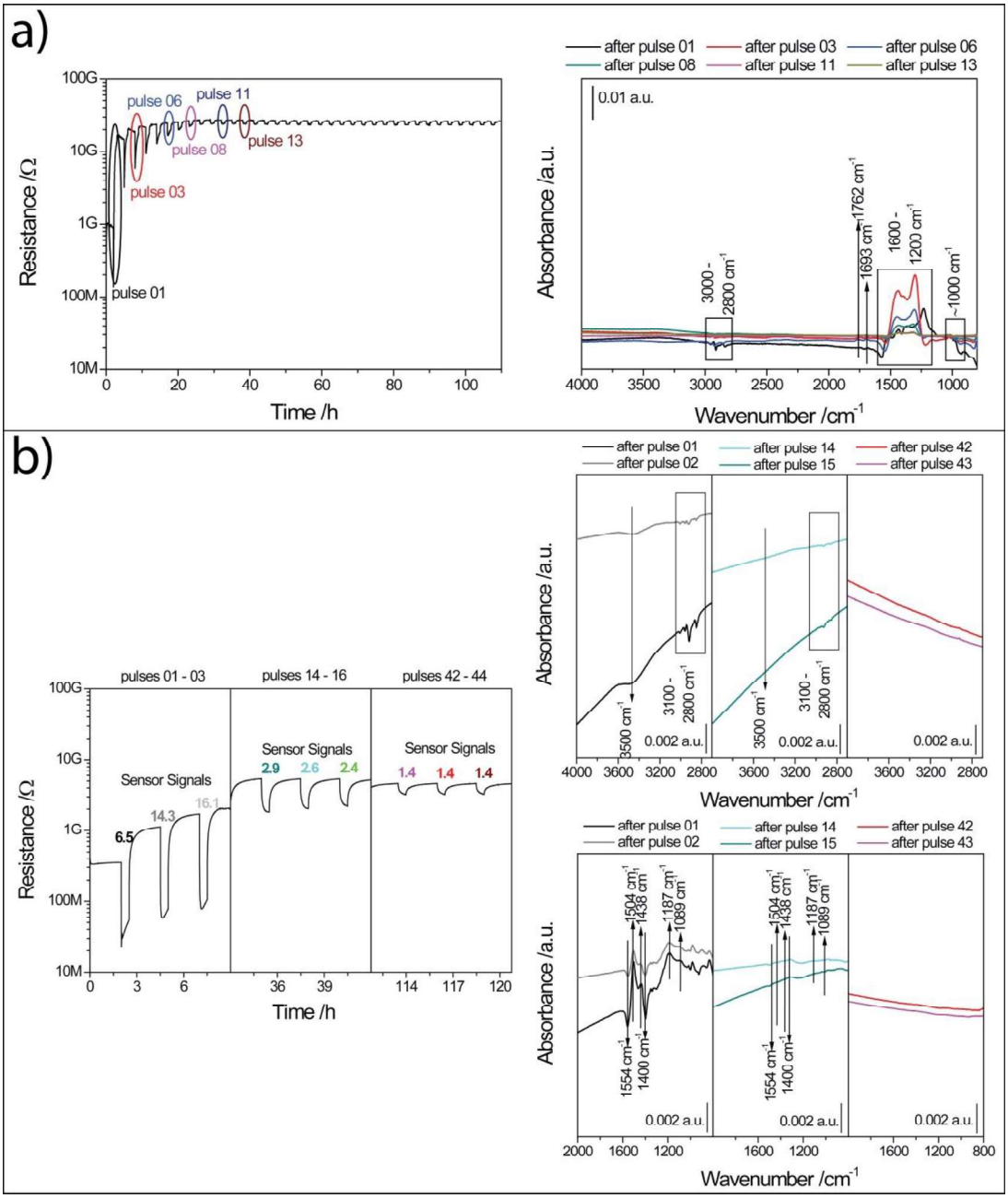

Figure 40: a) DC resistance measurement of a sensor prepared with micrometric PbS (right) and the DRIFT spectra (left) showing the changes in surface groups that are responsible for the baseline increase. b) DC resistance measurement of a sensor prepared with PbS CQDs (right) and the DRIFT spectra (left) showing the changes in surface groups that are responsible for the baseline increase (top: 4000 – 2700 cm^{-1}, bottom: 2000 – 800 cm^{-1}). From [110].

Even though the origin of the increasing bands between 1600 and 1200 cm^{-1} cannot clearly be assigned, the formation of sulphates can be excluded. The most reported product of the oxidation of PbS is $PbSO_4$ [62,118,119]. The vibrational bands of $PbSO_4$ would be expected between 1200 and 950 cm^{-1} [119]. These bands were not observed which is why the oxidation of the sulfide to the sulphate is excluded as reason behind the increase in baseline resistance.

Based on the DRIFT spectra, it is concluded that the reaction of the organics with the target gas NO_2 is responsible for the baseline increase observed for the sensor based on micrometric PbS. Additionally, the formation of nitrates and nitrites could play a role. For other materials, however, it was observed, that the electronic effect of the formation of nitrates is negligible and is, therefore, excluded as main contributor to the baseline resistance increase.

The aging mechanism of the sensor based on PbS CQDs also appears to be related to a reaction between organics and NO_2. As was the case for the sensors based on micrometric PbS, changing bands are observed in the typical wavenumber range for saturated C-H and C-C vibrations (between 3000 and 2800 cm^{-1}. Additionally, changing bands above 3000 cm^{-1} are observed which is the typical range for unsaturated C-H and C-C vibrations [113]. In the lower wavenumber range, sharp decreasing bands are observed at 1554 and 1400 cm^{-1} in addition to sharp increasing bands at 1504 and 1438 cm^{-1} and some broader increasing bands at 1187 and 1089 cm^{-1}. These bands are all observed as long as an increase in baseline resistance can be observed. An extensive literature research revealed that the decreasing bands both at around 3000 cm^{-1} and the two sharp bands at 1554 and 1400 cm^{-1} can be assigned to oleic acid [120]. Oleic acid was used during the synthesis of the PbS CQDs and should have been removed during the ligand exchange which was part of the sensor preparation process. The fact that not only decreasing but also increasing bands were observed indicated that oleic acid reacted with NO_2 to a different organic compound. There are multiple reports in literature about the reaction of oleic acid with NO_2 which results in the formation of nonanoic acid and azelaic acid [121–123]. The characteristic vibrations of these two acids were found to coincide with the observed increasing bands at around 3000 cm^{-1} and below 1600 cm^{-1}. The fact that these bands are observed in the DRIFT spectra led to the conclusion that the decomposition of oleic acid

into nonanoic acid and azelaic acid which both adsorbed on the surface of the PbS CQDs resulted in the formation of an insulation organic shell around the CQDs. Again, the formation of $PbSO_4$ which was often reported as the most common aging product of PbS could not be observed in the DRIFT spectra.

In order to confirm the proposed aging mechanism and to find definite proof that excluded the formation of $PbSO_4$ as aging product, samples were prepared on gold-coated silicon wafers (*Figure **41***), just like the samples that were investigated for the general characterization of the PbS CQDs (*Figure **36***).

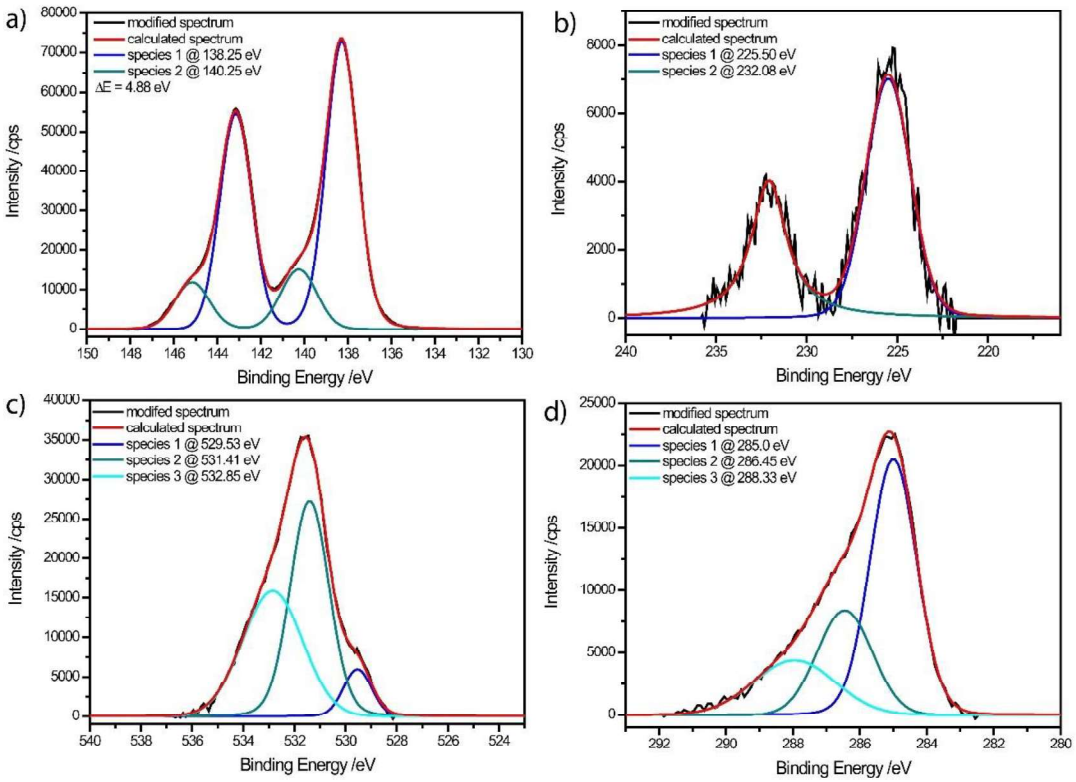

Figure 41: Detail spectra of different ranges of aged PbS recorded on a Si-Au waver: a) Pb 4f, b) S 2s, c) O 1s, d) C 1s. From [110].

All detail spectra clearly show changes in the surface composition of the PbS CQDs. While for the fresh sample, the main component of the Pb 4f detail spectrum was assigned to PbS (*Figure **36**a*, *Table **1***), this component could not be observed anymore for the aged sample (*Figure **41**a*, *Table **1***). Instead, the main component shifted to 138.2 eV which was assigned to a mixture of PbO, $PbCO_3$ and $Pb(OH)_2$. Additionally, a new component can be

observed, which was not found in the detail spectrum of the fresh sample. This component was found at 139.9 eV. This binding energy is higher than would be expected for $PbSO_4$. However, the binding energy of $PbSO_4$ is closest to the observed binding energy. When looking at the S 2s detail spectrum, the same two components are observed in the aged and in the fresh sample. The ratio of the components shifts in favor of the component at the higher binding energy which was assigned to $PbSO_4$. This would suggest that the amount of $PbSO_4$ increases as a result of aging. However, upon closer investigation of the XPS data, it was observed that the amount of sulfur decreased as a result of aging. The peak area of an XPS spectrum is directly proportional to the concentration of this element in a sample. There are certain sensitivity factors which would allow for the quantification of an element. In this work, however, the exact quantity is not of interest, and it is sufficient to look at the ratios of the elements to one another.

Table 1: Overview of the XPS data of the fresh and the aged sample [62–65,104,118,124–133]

sample	element	Binding Energy /eV	compound	Absolute Area (ratio)[a]	Ratio[b]
fresh	Pb 4f	137.7	PbS	472090 (0.58)	1
		138.6	$PbCO_3/PbO/Pb(OH)_2$	344964 (0.42)	
	S 2s	225.2	PbS	49469 (0.06)	0.071
		231.8	$PbSO_4$	8935 (0.01)	
	O 1s	529.5	$PbO_{tetragonal}$	9337 (0.01)	0.123
		531.4	$PbCO_3/PbO_{rhombic}$	837967 (0.10)	
		533.1	$Pb(OH)_2/H_2O_{ads}$	315601 (0.01)	
	C 1s	285.0	C-H	42309 (0.05)	0.074
		286.5	C-OH	3818 (0.005)	
		288.0	$PbCO_3$	14307 (0.02)	
aged	Pb 4f	138.2	$PbCO_3/PbO/Pb(OH)_2$	837967 (0.73)	1
		139.9	$PbSO_4$	315601 (0.27)	
	S 2s	225.5	PbS	22201 (0.02)	0.037
		232.1	$PbSO_4$	13756 (0.01)	
	O 1s	529.5	$PbO_{tetragonal}$	8467 (0.01)	0.112
		531.4	$PbCO_3/PbO_{rhombic}$	53808 (0.05)	
		532.9	$Pb(OH)_2/H_2O_{ads}$	46513 (0.04)	
	C 1s	285.0	C-H	36734 (0.03)	0.069
		286.5	C-OH	17268 (0.01)	
		288.3	$PbCO_3$	13382 (0.01)	

The area of each element was calculated with the help of the fitted data. The data was used to build two different ratios: one was calculated for each component compared to the total amount of Pb in the sample, the second one was calculated with the total amount of each element compared to the total amount of Pb. This way, it was possible to

determine if the ratios of the elements stay constant, and in case this ratio changed, if there are specific components this change could be assigned to. The results obtained for sulfur showed two things. Firstly, it was observed that the total amount of sulfur was divided by factor 2 in the aged sample compared to the fresh sample. Secondly, it was observed that the amount of sulphate compared to the amount of Pb in the aged sample stayed constant, but the amount of the sulfide sulfur (component at 225.5 eV) was divided by 3. The O 1s and C 1s detail spectra showed changes as well. The O 1s detail spectra indicated an increase in amount of $Pb(OH)_2$ or adsorbed water, while the C 1s detail spectra a shift in the direction of C-OH.

In conclusion, the XPS data indicated different things. While the Pb 4f detail spectra indicated an increase in $PbSO_4$, this was not confirmed by the S 2s and O 1s detail spectra. Instead, the S 2s detail spectra indicated a decrease in amount of sulfur in the sample. The C 1s and O 1s detail spectra indicated an increase in hydroxyl groups at the surface.

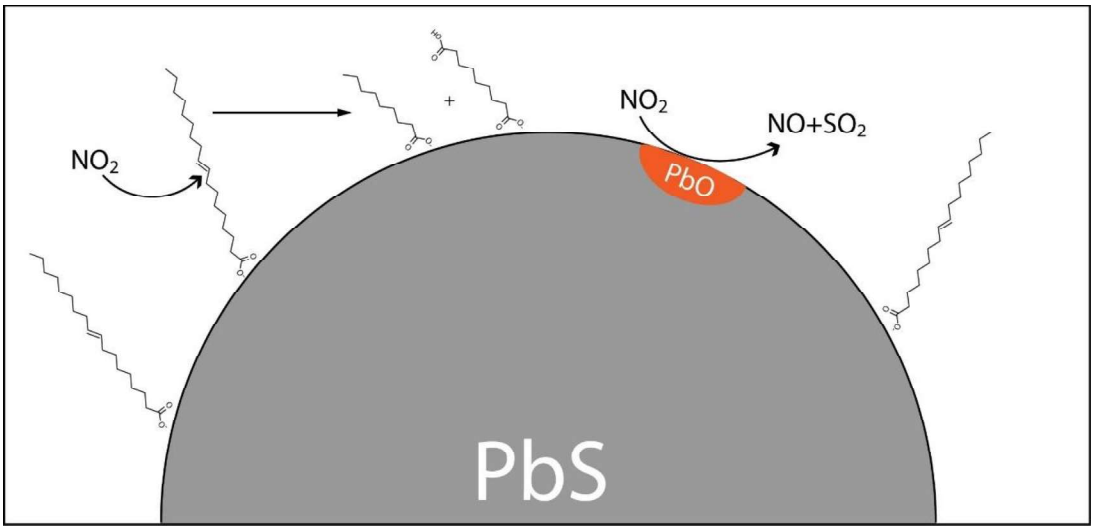

Figure 42: Schematic illustration of the reactions taking place at the surface of PbS CQDs resulting in the observed increase in resistance.

In literature a number of different aging mechanisms for PbS can be found. By far the most of them report $PbSO_4$ as oxidation product [134]. The data obtained in this work did not confirm the formation of $PbSO_4$. Instead, the DRIFT spectra indicated the reaction between oleic acid and NO_2 as reason behind the observed aging of PbS. The XPS data additionally indicated that the amount of sulfur decreased due to aging. Our observations

matched the reports by Nowak et al. and Zingg and Hercules [62,118,126]. Nowak et al. investigated the surface oxidation of PbS during the flotation process. They found that in the presence of organics, the main oxidation product was $PbCO_3$ [62]. Zingg and Hercules, on the other hand, found that in the beginning of the aging process, the surface was oxidized to PbO under elimination of gaseous SO_2 [118]. It was concluded that the observed increase in resistance had a mixture of reasons (*Figure **42***): 1) the residual oleic acid reacted with NO_2 resulting it the formation of nonanoic acid and azelaic acid which adsorbed at the surface and resulted in the formation of a poorly conducting shell around the PbS CQDs; 2) NO_2 oxidized the PbS surface to PbO under elimination of gaseous SO_2. The former reaction was confirmed with the help of the DRIFT spectra and the detail spectra in the Pb 4f and C 1s range, where the main components changed to $PbO/PbCO_3$ and $PbCO_3$, respectively. The latter reaction was concluded after the detailed evaluation of the Pb 4f and S 2s detail spectra where a decrease in the sulfur concentration was observed.

5.2.4. Sensing Mechanism of PbS CQDs

In order to understand the mechanism responsible for the observed sensor signal for both materials, the DRIFT spectra during the exposure to NO_2 were evaluated (*Figure **43***). The spectra in *Figure **43***a show the changes at the surface of the micrometric material under exposure to NO_2. For the first three pulses, the strongest bands are observed at 1162, 1068 and 968 cm^{-1}. These bands are positioned where the typical vibrations of $PbSO_4$ would be expected [119]. The fact that these bands are decreasing during the exposure to NO_2 means that the micrometric material must have been oxidized before it was exposed to NO_2. And even more, that $PbSO_4$ was not formed in the presence of NO_2. The interactions between the already present $PbSO_4$ and NO_2 result in the observed instable sensor behavior for the first few pulses. Furthermore, changing bands in the range between 3000 and 2800 cm^{-1} are observed. These bands are again assigned to C-H and C-C vibrations of saturated organic compounds. As was discussed in the earlier section about the aging mechanism, there is no precise information on the synthesis process which makes it difficult to assign these bands to a specific compound. However, similar to the aging mechanism, the sensor's behavior in NO_2 becomes stable when the organics do not change anymore.

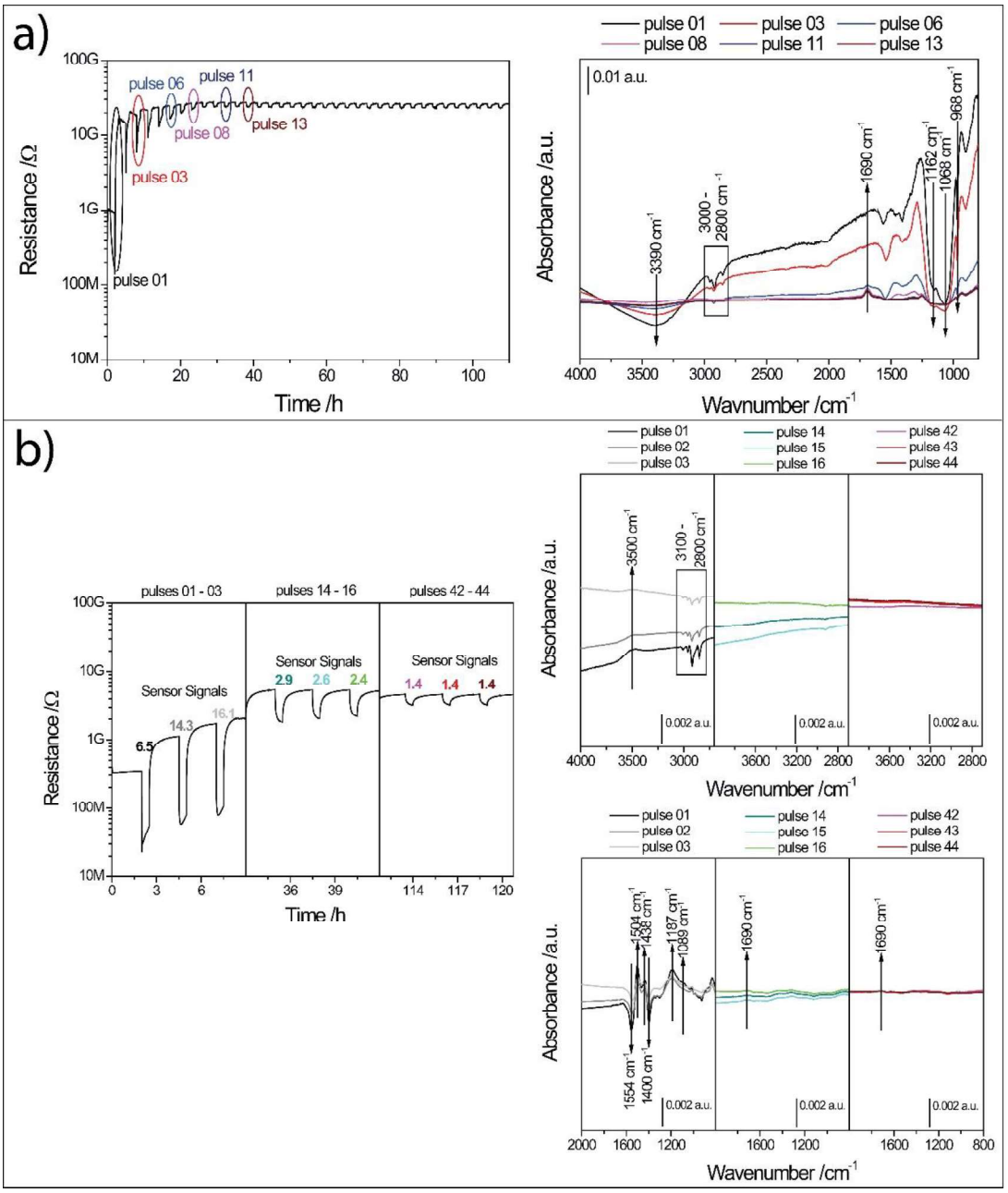

Figure 43: DRIFT spectra of the micrometric material (top) and the PbS CQDs (bottom) under exposure to 3 ppm NO_2 at room temperature. From [110].

Additionally, the decreasing sulphate bands were not observed when the sensor was back in synthetic air. This means that the reaction between NO_2 and the SO_4^{2-} group is reversible. As of now, the exact reaction is not clear for the first few NO_2 pulses. Starting with pulse 06, the spectra show reproducible behavior. The decreasing bands at 1162, 1068 and 968 cm^{-1} are barely visible starting with pulse 08. With pulse 06, an increasing band at 1690 cm^{-1} can be observed which can be assigned to molecularly adsorbed NO_2

[115]. The adsorption of NO_2 will result in the entrapment of electrons from the valence band which will result in an increase of holes in the valence band. This means that the number of charge carriers in PbS increases which can be observed as a decrease in resistance.

The DRIFT spectra of the PbS CQDs in NO_2 (*Figure **43**b*) show less differences compared to those evaluated for the discussion of the baseline increase (*Figure **40**b*). Again, the changing bands between 3100 and 2800 cm^{-1} are observed in addition to the decreasing bands at 1554 and 1400 cm^{-1} and the increasing bands at 1504, 1438, 1187 and 1089 cm^{-1}. The decreasing bands are still assigned to oleic acid, the residual from the synthesis process, while the increasing bands are assigned to its decomposition products nonanoic acid and azelaic acid [120–123].

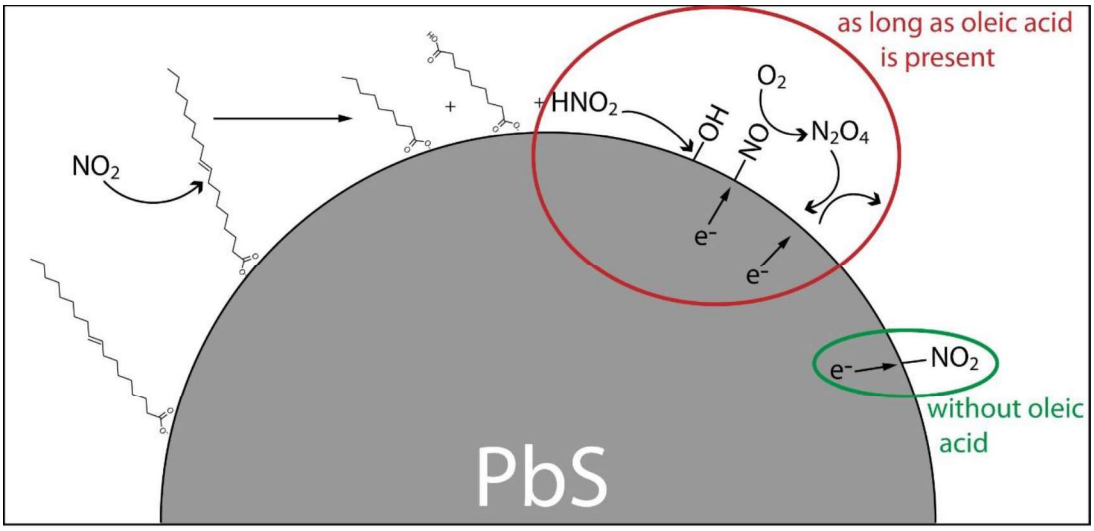

Figure 44: schematic illustration of the sensing mechanism with PbS CQDS in the presence of NO_2 with (red circle) and without (green circle) oleic acid enhancing the response.

This does not explain the change in resistance during the exposure to NO_2 since it was found that the reaction between oleic acid and NO_2 was responsible for the baseline increase. However, a reported by-product of this reaction is HNO_2, a highly reactive molecule. Further research revealed that HNO_2 can adsorb at the surface as –OH and –NO which explains the increasing band at 3500 cm^{-1} – a typical wavenumber for hydroxyl groups. The band of adsorbed –NO would be expected in the range where the decreasing and increasing bands of the decomposition products of oleic acid are observed [115].

Additionally, NO can react with O_2 to form N_2O_4 which is an excellent electron acceptor and could also be responsible for the observed sensor response.

When the changing organic bands cannot be observed anymore, an increasing band at 1690 cm^{-1} is observed – like for the micrometric sample. This band is again assigned to molecularly adsorbed NO_2 which results in the stable response at the end of the experiment [115]. Since the sensor signal decreases in correlation with the changing organic bands, it is concluded that the by-product of the consumption of oleic acid – HNO_2 – is responsible for the high sensor signal in the beginning of the experiment. With an increasing number of exposures to NO_2, less and less oleic acid remains at the CQD surface that can be consumed by NO_2 resulting in less HNO_2 to enhance the sensor signal. At some point, less to no oleic acid is consumed which is when the adsorption of molecular NO_2 is observed. Comparable to the micrometric material, the adsorption of NO_2 is responsible for the stable sensor signal at the end of the experiment. The summary of the sensing mechanism is schematically illustrated in *Figure **44***.

5.2.5. Aging and Sensing Mechanism of PbS CQDs without Oleic Acid

Since organics played a key role in the observed instability of the sensors and in the sensing process, an additional sensor was produced with a slightly different ligand exchange procedure. The minimal adaptation in the ligand exchange following the principle “the more, the better” included the exchange of each layer with both exchange solutions instead of exchanging two layers of PbS with NH_4Cl and two layers with $NaNO_2$. The sensor was exposed to the same measurement protocol as the previously investigated sensor based on CQDs and a severely different behavior was observed (*Figure **45***).

There are multiple differences in the behavior of the two sensors. The most obvious differences are the time it takes for the baseline resistance and the sensor signal to stabilize. The baseline resistance of the sensor with the standard ligand exchange (discussed in the previous section, *Figure **45*** top) stabilizes after roughly 15 exposures to 3 ppm NO_2. The baseline resistance of the sensor prepared with the modified ligand exchange does not stabilize until the end (*Figure **45***, bottom). There is a small but constant increase in baseline resistance after each exposure, even after more than 40 exposures.

On the other hand, the stabilization process of the sensor signal shows the opposite effect: While it takes almost 40 exposures until the sensor prepared with the standard ligand exchange reaches a stable sensor signal, the sensor prepared with the modified ligand exchange shows stable sensor signals starting with the fourth exposure already and it stays constant even though the baseline resistance constantly increases. In order to identify the underlying surface reactions resulting in the observed differences in behavior, DRIFT spectroscopy was done again. *Figure **46*** shows the resistance data of both sensors of the same NO_2 pulses enabling the best possible comparison of the surface reactions and the influence of the ligand exchange.

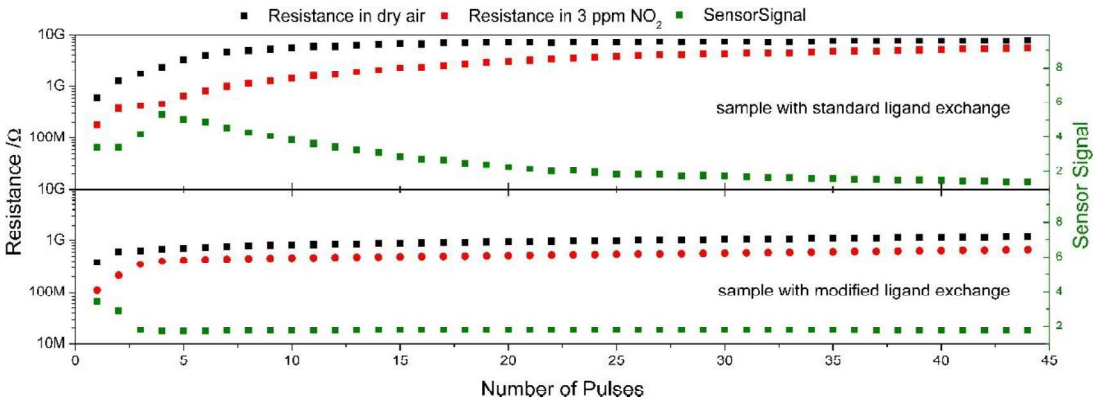

Figure 45: comparison of the data obtained with the two different sensors based on PbS CQDs. The sensor that was discussed in the previous section is shown at the top, the sensor with the slightly modified ligand exchange is shown at the bottom. Adapted from [110].

The data shown in *Figure **46***a is the data that was discussed in the previous section. The surface aging was related to the reaction between oleic acid – a residual from the synthesis – with NO_2 based on the decreasing bands at 1554 and 1400 cm^{-1} (oleic acid) and the increasing bands at 1504, 1438, 1187 and 1089 cm^{-1} (nonanoic acid and azelaic acid). The spectral data recorded on the sample prepared with the modified ligand exchange shows none of these bands. Additionally, the bands observed after the first pulse are different than those observed after the second pulse. The bands observed between 1600 and 1200 cm^{-1} after the first two pulses are assigned to different nitrate and nitrite species [115]. For the first pulse, an additional increasing band at 837 cm^{-1} is observed which was assigned to $Pb(NO_3)_2$ [135]. The decreasing double band centered at 1117 cm^{-1} which was observed after the second pulse, was assigned to a Pb-S vibration [136]. The band at 1708 cm^{-1} decreases after the first pulse but increases just as strongly

after the second pulse. It is possible that these bands correlate to molecularly adsorbed NO_2. However, it is unclear why this band would decrease after the first pulse. After pulses 14 and 15, only small increasing bands in the range for nitrates and nitrites can be observed. After pulses 42 and 43, the spectra are not indicative of any specific groups. The sharp band that is observed after pulse 42 at around 1350 cm^{-1} is assumed to be an artifact. None of the prior or following spectra after that pulse showed that band.

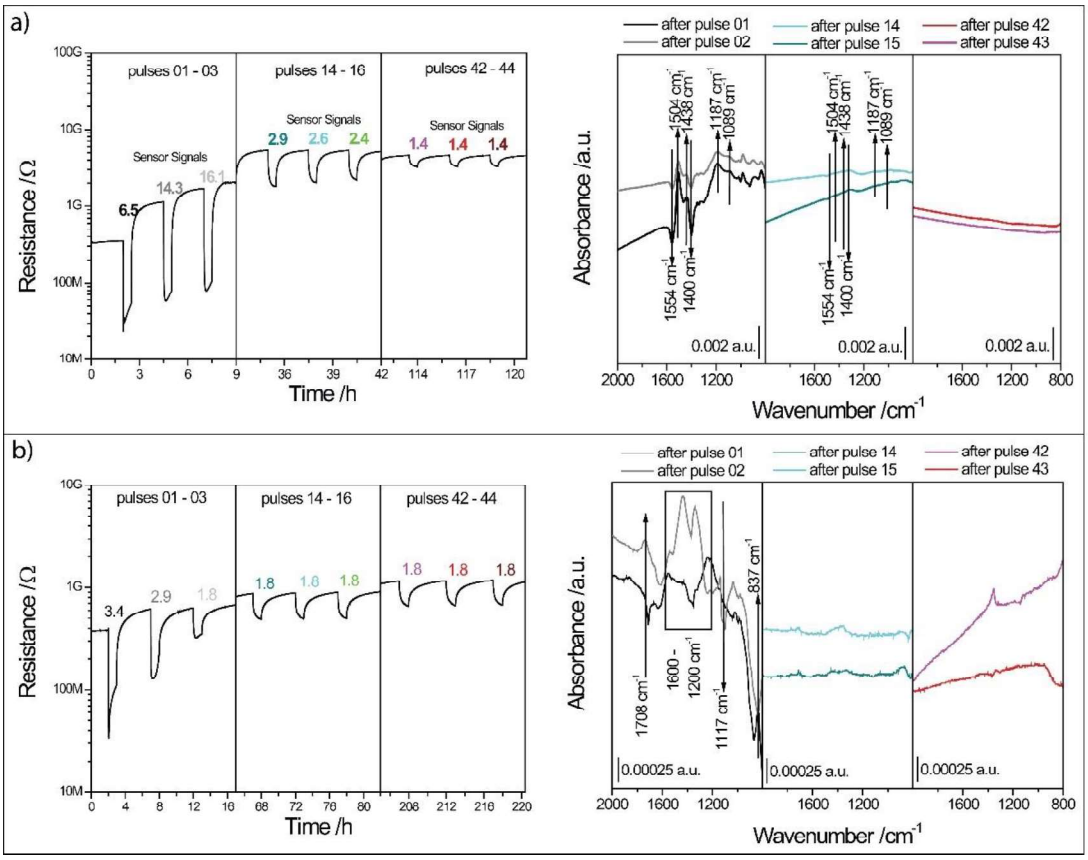

Figure 46: a) DC resistance measurement and DRIFT spectra of the sensor prepared with CQDs that underwent the standard ligand exchange, as was discussed in the previous section, showing the changes at the surface responsible for the increase in baseline resistance. b) DC resistance measurement and DRIFT spectra of the sensor prepared with CQDs that underwent the modified ligand exchange showing the changes at the surface responsible for the increase in baseline resistance. From [110].

Similar to what was observed when investigating the differences in ageing (see above), the changes at the surface during the exposure to NO_2 also are completely different for the two samples. Figure 47 shows the DC resistance measurements and DRIFT spectra of

both samples during the same exposures after which the change in baseline was investigated in the prior sections.

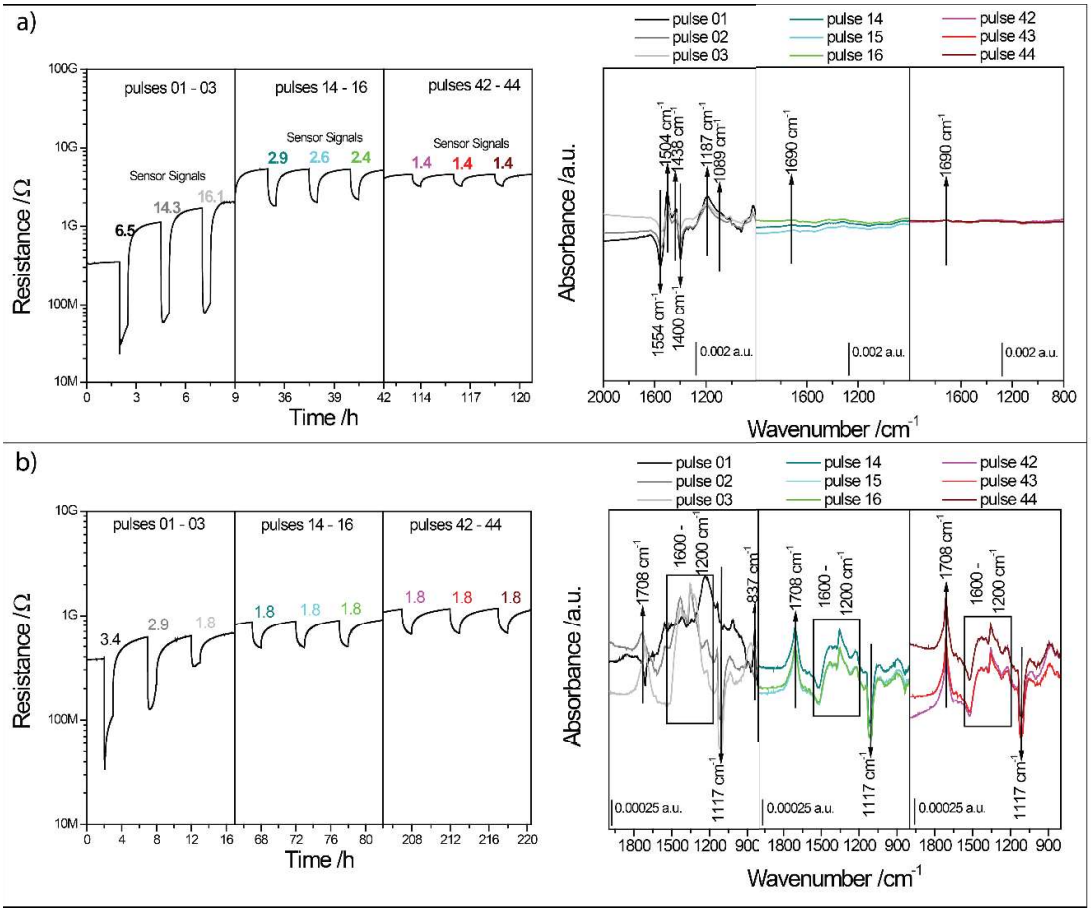

Figure 47: a) DC resistance (left) and DRIFT spectra (right) of the sensor prepared with CQDs that underwent the standard ligand exchange, as was discussed in the previous section, showing the changes at the surface during the exposure to NO_2. b) DC resistance (left) and DRIFT spectra (spectra) of the sensor prepared with CQDs that underwent the modified ligand exchange showing the changes at the surface during the exposure to NO_2. From [110].

Just as was observed for the changes at the surface after the exposure to NO_2 for the sample that underwent the modified ligand exchange, the first pulse looks significantly different than the other pulses. Pulse 02 and 03 already show comparable bands as are observed during pulse 14 and all following pulses. There is an increasing band at 1708 cm^{-1} which is assigned to molecularly adsorbed NO_2. The multiple increasing bands observed between 1600 and 1200 cm^{-1} are assigned to various nitrates and nitrites, while the decreasing double band at 1117 cm^{-1} is assigned to a Pb-S overtone vibration. At 837 cm^{-}

[1], an increasing band is observed which is assigned to $Pb(NO_3)_2$. Based on this spectral data, it is concluded that the PbS sample without any organics at the surface has a significantly different sensing mechanism than the initially investigated sample. As before, molecularly adsorbed NO_2 will result in a redistribution of charges at the surface resulting in a decrease in resistance. The fact that the response is stable at around 1.8 instead of the 1.4 observed for the sample that underwent ageing in the presence of organics, might be attributed to the lack of the organic shell surrounding the CQDs after the modified ligand exchange. However, the fact that the baseline still shows an upwards drift even in the absence of organics which could form an insulating shell around the semiconducting CQDs shows the inherent instability of PbS and therefore the unsuitability of PbS as a pristine material for its usage in gas sensors.

5.3. Bi_2S_3

5.3.1. Basic Characterization

The Bi_2S_3 nanorods were characterized by powder XRD as well es by SEM and EDX. The powder XRD was recorded by the collaboration partners at the Huazhong University of Science and Technology, Wuhan, P.R. China, of the freshly prepared sample right after the synthesis. The SEM and EDX data were recorded at the University of Tübingen after their deposition on the Al_2O_3 substrates via spin coating and after the ligand exchange with $Pb(NO_3)_2$.

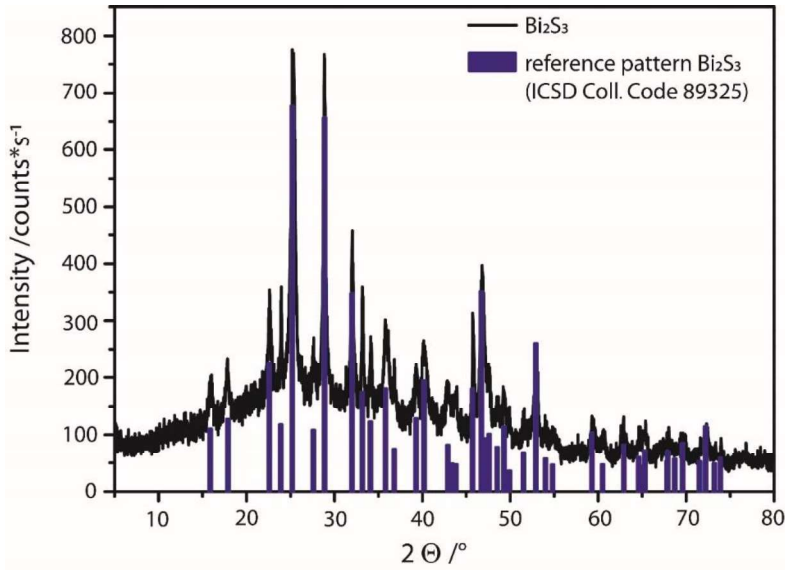

Figure 48: powder XRD or freshly prepared Bi_2S_3 nanorods (black) and a reference pattern (blue) confirming the successful synthesis of Bi_2S_3.

The XRD pattern shows that Bi_2S_3 was successfully synthesized confirmed by a reference pattern of the International Crystal Structure Database (ICSD) no. 89325 (*Figure **48***) [137].

The SEM images show that Bi_2S_3 is mostly present in the form of nanorods (*Figure **49***). The EDX data confirms that the observed needles consist of Bi and S. However, Al, O and Pt are also observed as a result of the thin layer of the sample which leads to the observation of the substrate elements in the EDX (*Figure **49***, bottom). The big particles/agglomerates that are observed in the SEM images were also investigated with the help of EDX. In these areas Bi and S are also observed, however the strongest peaks are observed for Al and O

again as a result of the very thin sample layer. It should be noted that Pt is not observed in this area indicating that this area is not on top of an electrode.

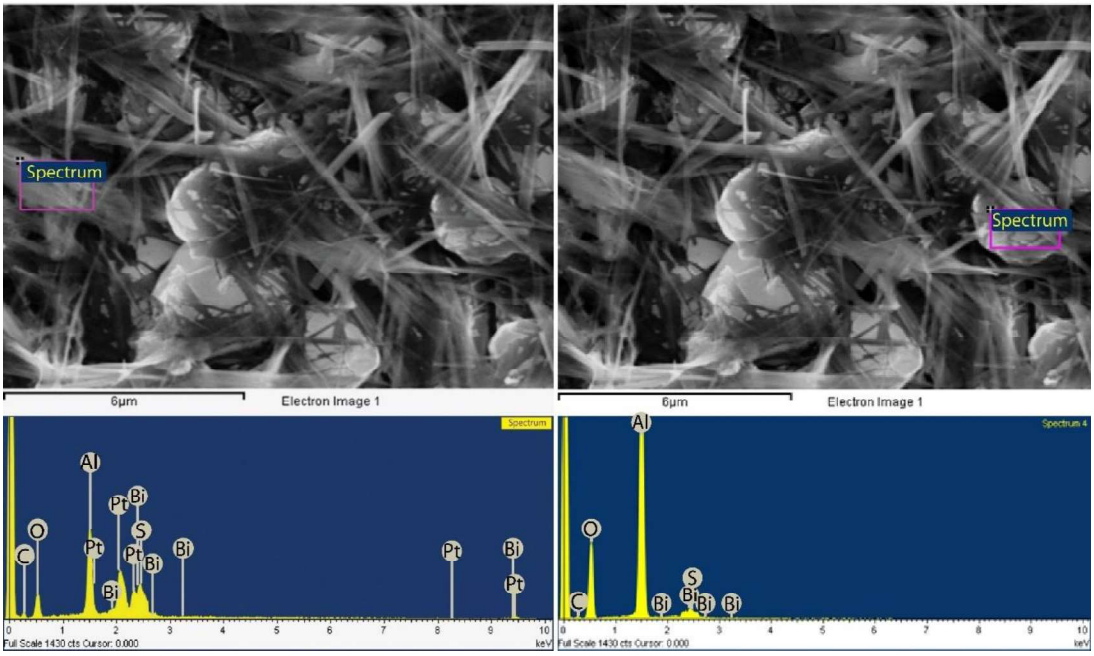

Figure 49: SEM images of Bi_2S_3 nanorods spin coated on Al_2O_3 substrates and EDX spectra of two different areas as marked in the SEM images at the top. From [138].

5.3.2. Determination of the Transduction Mechanism

Since there is not a lot of literature on Bi_2S_3 and its usage for gas sensors, there is also not a lot of information on the transduction mechanism. Therefore, in the first test, a Bi_2S_3 sensor was investigated in a Kelvin Probe setup. The Kelvin Probe technique has been successfully used to investigate the transduction mechanism of several semiconducting materials used in gas sensors like SnO_2 among others [33,105,107,108,139–142]. The easiest way to test whether a material follows an electron depletion or hole accumulation layer-controlled transduction mechanism, is its exposure to different levels of oxygen in a nitrogen background while measuring the materials work function and the respective resistance. The theoretical background is explained in section 3.5.

A Bi_2S_3 was placed in a gas tight test chamber that allowed for the simultaneous measurement of the material's work function and resistance under controlled gas exposures. The sensor was equilibrated in a nitrogen background and then exposed to

oxygen concentrations between 1000 pm and 20.5 % in nitrogen. The results are shown in *Figure* ***50***a. The black curve shows the contact potential difference between the reference tip and the surface of Bi_2S_3. In the presence of only nitrogen, it is assumed that the energy bands of Bi_2S_3 are flat while the presence of oxygen will result in an upwards band bending. Depending on whether the conduction mechanism is electron depletion or hole accumulation layer controlled, the resistance will increase or decrease, respectively. The resistance of the Bi_2S_3 sensors increases in the presence of oxygen which suggests an electron depletion layer-controlled conduction mechanism.

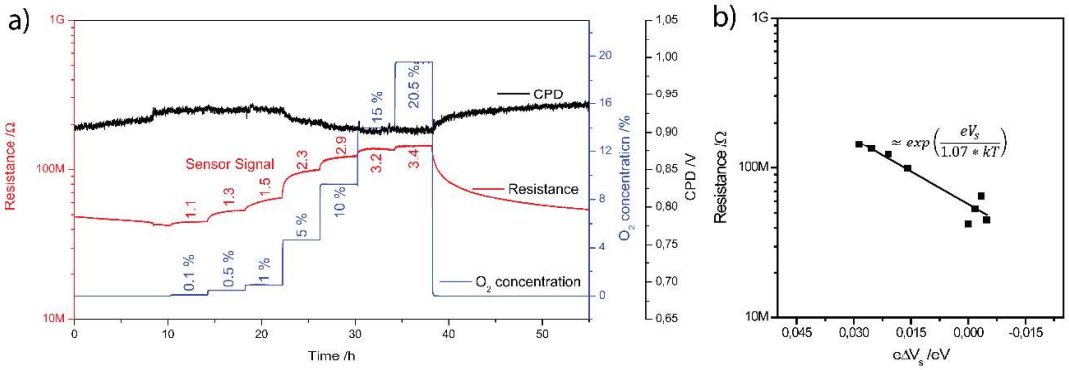

Figure 50: a) measurement of the contact potential difference and the resistance in dependence of the oxygen concentration. b) The resistance is plotted over the change in surface band banding allowing for the determination of the transduction mechanism. From [138].

This is confirmed with the help of the plot shown in *Figure* ***50***b where the resistance is plotted over the change in surface band bending in accordance with equation 7. As discussed earlier, based on the value determined for factor *m*, one can determine the conduction mechanism without a doubt. For a perfect depletion layer-controlled conduction mechanism, *m* will have the value 1. For a perfect accumulation layer-controlled conduction mechanism, *m* will have the value 2. The fit based on the data obtained with the Bi_2S_3 sensor gives the value 1.07 for *m* which is very close to the value for a perfect depletion layer-controlled conduction mechanism.

5.3.3. General Gas Sensing Profile

After it was determined that the conduction mechanism of Bi_2S_3 is depletion layer-controlled, the next step was to determine the gas sensing profile of Bi_2S_3.

There is not a lot of literature on gas sensing with Bi_2S_3 and the reports that were published show opposing trends in selectivity (see 2.4). Especially the reported sensitivity towards different VOCs was confusing. There are studies that show that the sensitivity and selectivity of a material can strongly depend on the way it was synthesized even though characterization shows that both materials are of comparable composition. A prominent example is SnO_2. Degler et al. found that two SnO_2 samples that were synthesized via the same route and only were calcined at different temperatures, showed severely different surface reactions [143]. They found that SnO_2 that was calcined at 450 °C formed carbonates under exposure to CO, which was not observed for the sample that was calcined at 1000 °C. They concluded that the calcination temperature strongly influenced the surface species that were formed [143]. This was later supported by Wicker et al. with the help of theoretical calculations [96].

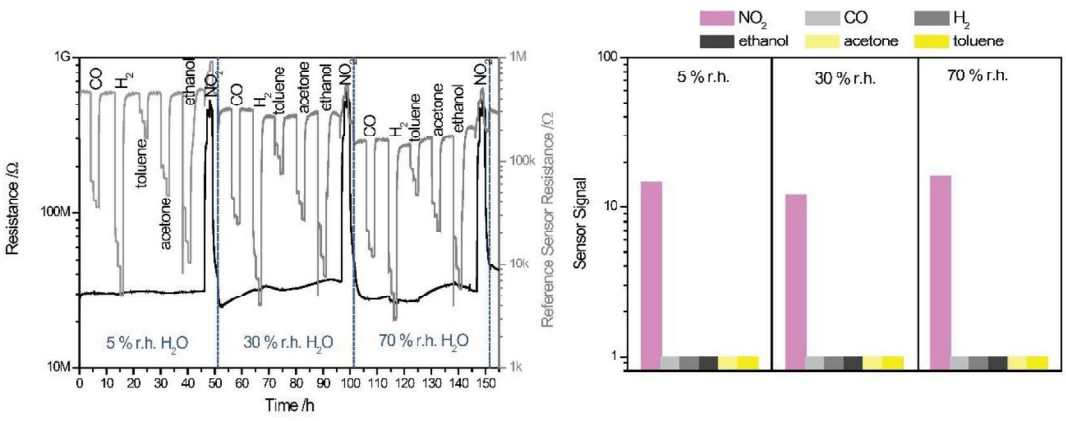

Figure 51: left: DC resistance measurement of a Bi_2S_3 sensor exposed to the standard protocol (black) and a reference sensor (grey) showing that the reason for the lack of a response of the Bi_2S_3 was not related to an issue with the experimental setup. right: bar chart showing the sensor signal to the respective gases. A response of 1 means that there was no response (see equation 8). From [138].

Since it cannot be excluded that the differences in behavior of the reported Bi_2S_3 gas sensors was a result of differences in the synthesis strategy resulting in different surface species, it was necessary to screen the Bi_2S_3 nanorods for their gas sensing characteristics as there was no way to predict how this sample would perform. This was done in a standard test system where the sensors were exposed to CO, H_2, toluene, acetone, ethanol and NO_2 in different background humidity levels. The sensors were operated at 50 °C.

The measurement shows that the Bi_2S_3 sample only responds to NO_2 (*Figure **51***). None of the reducing gases resulted in a response. This might be a result of a lack of surface oxygen which is required in many of the publicly accepted surface reactions with the tested reducing gases. CO for example is in general expected to reduce the surface under formation of CO_2 and a surface vacancy. A similar reaction is expected for H_2 where H_2O is often considered to be the reaction product. The fact that Bi_2S_3 does not have any surface oxygen could therefore be the reason for the observed selectivity. The situation is different for NO_2, an oxidizing gas that is willing to part ways with oxygen under formation of NO. It is possible that sulfur vacancies at the surface are reaction partners for this reaction. DRIFT spectroscopy was done in order to get additional information on the reaction mechanism (see 5.3.4).

5.3.4. Gas Sensing Mechanism of NO_2

As was discussed in the previous section, NO_2 was the only gas that was detectable with the here investigated Bi_2S_3 sensor. It was hypothesized that this was a result of the reaction of NO_2 with sulfur vacancies filling the vacancy with oxygen under formation of NO. To get as much information as possible on the sensing mechanism of NO_2 with a Bi_2S_3 sensor, DRIFT spectroscopy and Kelvin Probe measurements each coupled with DC resistance measurements were conducted. While DRIFT spectroscopy is an effective tool to identify surface reactions that result in the observed resistance changes, Kelvin Probe and DC resistance measurements reveal the electronic changes induced by said identified surface reactions.

First, the influence of the surface reactions on the surface band bending were investigated by measuring the changing CPD. In case the reaction with NO_2 is purely based on healing sulfur vacancies at the surface of Bi_2S_3 with oxygen under formation of NO, it is expected to see a correlation between the surface band bending and the resistance similar to what was observed with oxygen, namely a correlation where factor $m = 1$. Therefore, the sensor was exposed to NO_2 concentrations between 50 ppb and 7 ppm while the CPD and the resistance of the sensor were constantly measured. The results are shown in *Figure **52***.

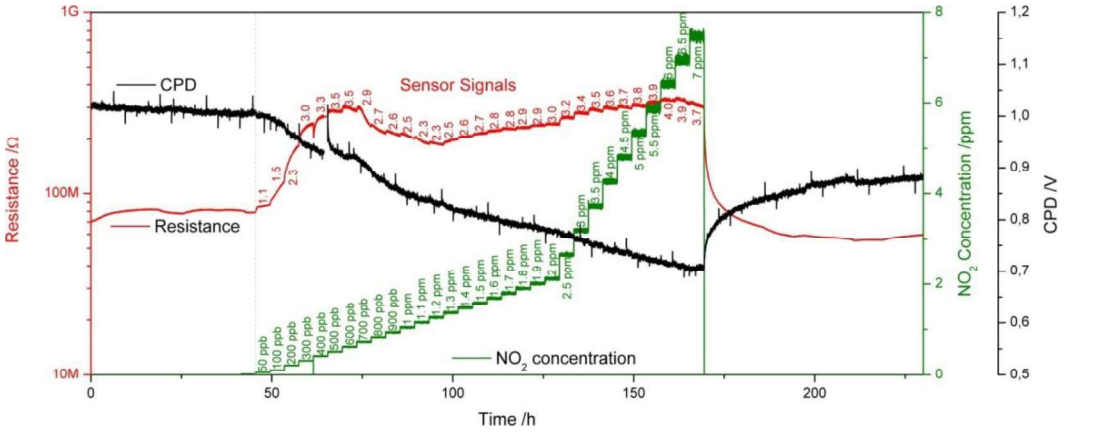

Figure 52: influence of increasing NO_2 concentrations on the contact potential difference and the resistance, measured in a background of dry synthetic air. From [138].

The sensor's behavior for low NO_2 concentrations was in the range of what was expected: the CPD decreased while the resistance increased. However, when the sensor was exposed to 600 ppb the resistance dropped while the CPD still decreased. Further increase in NO_2 concentration resulted in a further decrease in resistance up to a concentration of 1.2 ppm NO_2 at which point the resistance started to increase again. There were cases reported in literature, where a switch from a depletion layer-controlled to an accumulation layer-controlled mechanism for materials with small band gaps was observed due to a cross-over of the valence band and the Fermi-level as a result of upwards band bending [142]. If this were the case for Bi_2S_3 in the presence of NO_2, one would expect a decrease in resistance for concentrations higher than 600 ppb. However, since the resistance starts to increase again with concentrations higher than 1.2 ppm, a purely electronic reason for this behavior can be excluded. It was concluded that the observed behavior must result from chemical changes, to be exact: a change in surface reaction. In order to test this hypothesis, the sample was investigated with the help of *in-operando* DRIFT spectroscopy.

The regions of interest in a DRIFT spectrum are below 2000 cm^{-1}. Between 1600 cm^{-1} and 1200 cm^{-1}, the formation of various nitrate and nitrite species would be observable [115]. In case NO_2 gets molecularly adsorbed at the surface, an increasing band at around 1700 cm^{-1} should appear [115]. Based on the fundamental vibrations of Bi_2S_3 at 1120, 868 and 618 cm^{-1}, overtone vibrations could appear between 1700 and 1650 cm^{-1} as well as between 1200 and 1150 cm^{-1} [144–148]. As discussed in the previous chapter on gas

sensing with PbS, it is also possible that the organic ligand used during the synthesis could play a role in the sensing mechanism. Therefore, vibrations of oleyl amine should also be considered. These can be found at 1647, 1593, 1465 and 1071 cm^{-1} [149]. Since NO_2 is capable of healing oxygen vacancies in metal oxides, it should also be considered that NO_2 might be able to heal sulfur vacancies which would result in the formation of Bi-O bonds. If this were the case, increasing bands should be observed at 820 cm^{-1} and 420 cm^{-1} [150]. The available DRIFT setup is only capable of measuring down to 800 cm^{-1}. Therefore, in case Bi-O bonds were formed, it is highly unlikely that the bond formation could be observed in these measurements.

*Figure **53*** shows the results of the experiment in the DRIFT setup. *Figure **53***a shows the DC resistance in dependence of the NO_2 concentration, *Figure **53***b shows the respective changes at the surface during the exposure to 600 ppb where the change in behavior takes place.

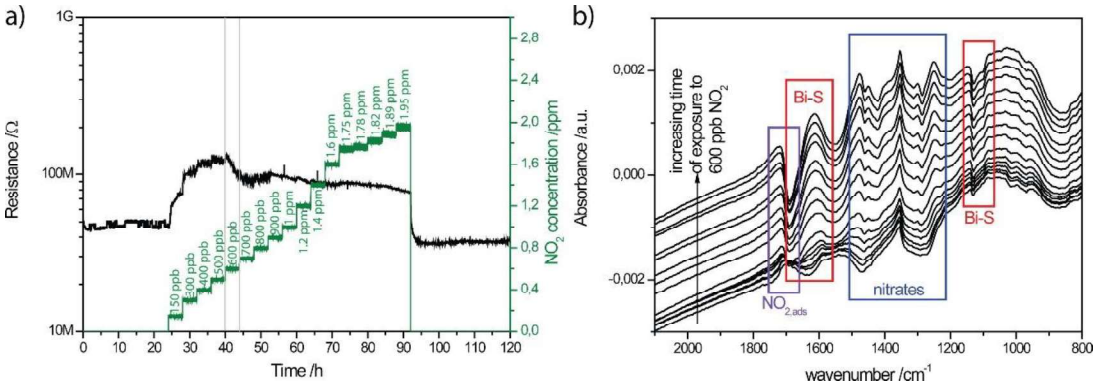

Figure 53: a) DC resistance of a Bi_2S_3 sensor in the presence of different NO_2 concentration in a background of dry synthetic air, operated at 50 °C. b) The DRIFT spectra evaluating the 4-hour exposure to 600 ppb NO_2. From [138].

The spectroscopic data shown in *Figure **53***b indicates that a change in the chemical reaction at the surface takes place when exposed to at least 600 ppb NO_2. The spectrum recorded at the end of the exposure to 600 ppb, or any higher concentration shows different features than the spectrum recorded at the end of the exposure to 500 ppb or any lower concentration. In order to better comprehend what exactly changes during the exposure to 600 ppb, the spectral data recorded during this concentration step was investigated more thoroughly.

In the beginning of the exposure, an increasing band at 1701 cm^{-1} is observed which can be assigned to molecularly adsorbed NO_2 [115]. The longer the material is exposed to 600 ppb NO_2, this band shifts to slightly higher wavenumbers due to an overlap with a decreasing double band (1689 and 1672 cm^{-1}). Next to the decreasing double band, an increasing double band (centered at 1612 cm^{-1}) is observed. Additionally, nitrates and nitrites start to form the longer the sensor is exposed to 600 ppb NO_2 based on the increasing bands between 1500 and 1200 cm^{-1}. The fact that the double feature with the decreasing and increasing double bands next to each other appears at the same time as nitrates and nitrites start to form, suggests a correlation between these surface groups. Both double bands (the decreasing one centered at 1680 cm^{-1} and the increasing one centered at 1612 cm^{-1}) are in the range where Bi-S overtone vibrations can be expected. The fact that these two bands present as double bands supports the assumption that both double bands can be assigned to Bi-S overtone vibrations. In the Bi_2S_3 lattice, there are two slightly different Bi-centers. While one of the Bi atoms is bonded to four S atoms, the other Bi atom is bonded to five S atoms which would result in slightly different vibration frequencies.

Decreasing bands are usually associated with breaking of a chemical bond, as for example observed for metal oxides where decreasing metal-oxygen bands usually mean that oxygen is removed from the lattice. However, the fact that in the case of Bi_2S_3, the decreasing double band is accompanied by an increasing double band at slightly lower wavenumbers could also indicate that the Bi-S bond is weakened instead of broken which would be observed as exactly that – a decreasing double band next to an increasing double band at lower wavenumbers. The simultaneous formation of nitrates and nitrites indicates that the Bi-S bond is weakened as a result of surface nitrates and nitrates.

This leads to the question why nitrates would be observed and why the resistance would start to behave unexpectedly the moment the nitrates formation is first observed. The DRIFT spectra indicate molecularly adsorbed NO_2 (increasing band at 1701 cm^{-1}) and a weakened Bi-S bond due to the formation of nitrates and nitrites (double feature at 1680 and 1612 cm^{-1} in addition to the increasing bands between 1500 and 1200 cm^{-1}). A commonly reported reaction of NO_2 at the surface metal oxides includes the healing of oxygen vacancies under formation NO. Bi_2S_3 is obviously not a metal oxide and therefore

has no oxygen vacancies. However, it is highly probable that Bi_2S_3 has sulfur vacancies instead. It is possible that the sulfur vacancies could be healed by NO_2 under formation of NO similar to the surface reaction with metal oxides. As mentioned in the beginning of this section, the formation of Bi-O would result in increasing bands at 820 and 420 cm^{-1} [150]. With the setup available at the institute, bands in this wavenumber range cannot be measured since they are outside the detector's range. This means with the currently available experimental data it is not possible to prove the healing of sulfur vacancies with oxygen, however, the fact that the formation of nitrates is observed strongly suggests this reaction.

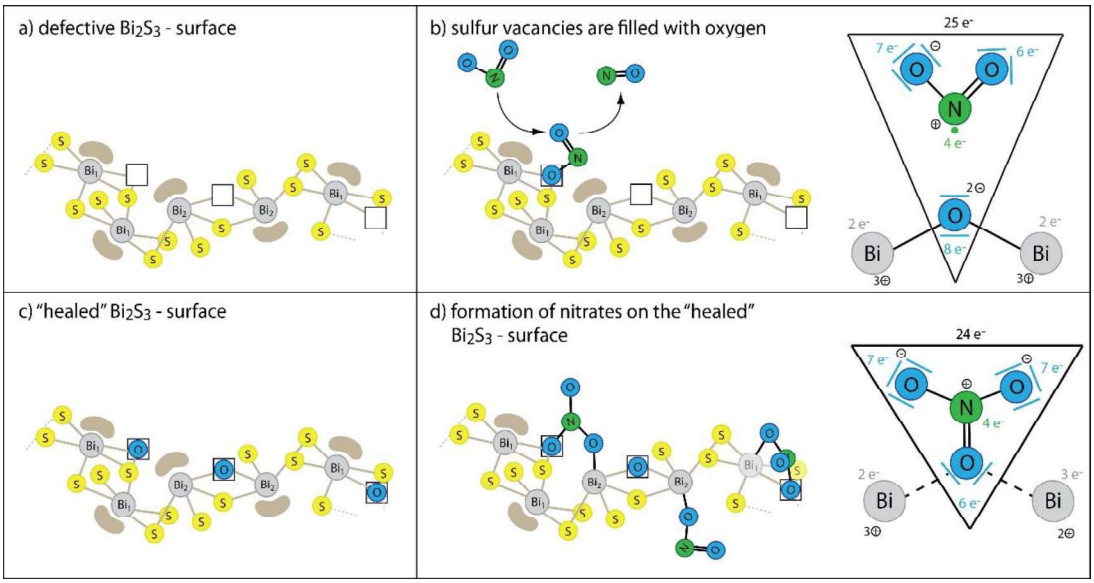

Figure 54: Schematic illustration of the NO_2 sensing mechanism on the surface of defective Bi_2S_3 in dependence of the NO_2 concentration. a) defective Bi_2S_3 surface as it is present; b) reduction of NO_2 to NO resulting in healed sulfur vacancies that are filled with oxygen, and schematic illustration of the involved valence electrons; c) surface with healed oxygen vacancies, d) schematic illustration of the reaction of NO_2 with the healed Bi_2S_3 surface resulting in the formation of nitrates, and schematic illustration of the involved valance electrons showing the release of one electron back into the base material. From [138].

Based on the DRIFT spectra, the following conclusions are made:

1) In low NO_2 concentrations, sulfur vacancies at the surface of Bi_2S_3 are healed by NO_2 with oxygen under the formation of NO.
2) At 600 ppb NO_2, the previously healed sulfur vacancies that are now filled with oxygen enable the formation of nitrates and nitrites.

3) In the presence of all NO_2 concentrations, molecularly adsorbed NO_2 is observed.

The change in chemical reaction at the surface of Bi_2S_3 coincides with the observed change in behavior of the resistance. In order to understand how the changing surface reaction can result in the observed resistance changes, one has to look closer into the electrons that are involved in these reactions. NO_2 has 17 valence electrons in its gaseous form. Oxygen that is bound in the Bi_2S_3 lattice has 8 valence electrons. This means, free gaseous NO_2 and lattice bound oxygen have a total of 25 valence electrons. This is the situation expected in low NO_2 concentrations. When gaseous NO_2 forms a nitrate with the oxygen bound in the Bi_2S_3 lattice, this nitrate has 24 valence electrons, one electron less than free NO_2 and lattice bound oxygen. This electron is released into Bi_2S_3 upon formation of nitrates. The experiments that are described in section 5.3.2 show that the transduction in Bi_2S_3 is depletion layer-controlled which means that the released electron would be observable as a decrease in resistance, which is exactly what is observed.

The concluded surface reactions explain the behavior of the resistance with increasing NO_2 concentrations. However, as mentioned earlier, a depletion layer-controlled transduction means that a decrease in resistance should be accompanied by an increase in CPD, while an increase in resistance should be accompanied by a decrease in CPD. This is not the behavior that was observed in the Kelvin Probe experiment – the CPD constantly decreased while the resistance changed its behavior multiple times (*Figure **52***). A possible explanation for this phenomenon could be the simplifications that were made earlier. For the initial evaluation, it was assumed that the change in CPD is equivalent to the change in surface band bending. However, it was also mentioned that this was only true if no surface dipoles were present at the surface. The healing of surface vacancies with oxygen is not expected to result in the formation of surface dipoles. NO_2, on the other hand, is a molecule that has been reported to form surface dipoles which would influence the electron affinity at the surface of the semiconductor which would further result in a change in CPD. This means earlier simplifications cannot be made anymore. Instead, one must calculate the theoretically expected change in CPD based on the measured change in resistance. The difference between the theoretically expected values for the change in CPD and the measured change in CPD will give the change in electron affinity at the

surface resulting from the formation of surface dipoles due to the absorption of NO_2 in the form of nitrates or nitrites.

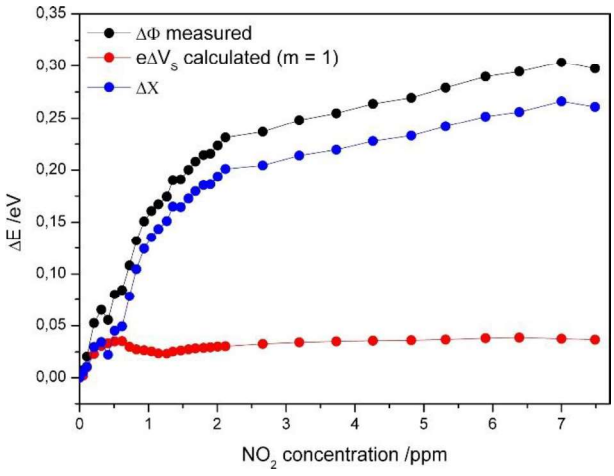

Figure 55: This graph shows the measured change in work function (black), the calculated and expected change in band bending based on a perfect depletion layer controlled transduction (red) and the resulting change in electron affinity based on the measured change in work function and calculated and expected change in band bending (difference between red and black). From [138].

The result of this evaluation is shown in *Figure* ***55***. Based on the results shown in this figure, one can determine three different regions in the increase in electron affinity. There is an initial increase in electron affinity up to roughly 600 ppb NO_2, at which point the change in resistance behavior is observed. Even for low concentrations, there is already a significant increase in electron affinity. At this point, there are two reactions expected to occur: 1) the healing of sulfur vacancies with oxygen under reduction of NO_2 to NO; and 2) the formation of nitrites due to the molecular adsorption of NO_2. Reaction 1 is not expected to result in the formation of surface dipoles. Reaction 2, on the other hand, could very well result in a shift in electron distribution in NO_2 and result in the formation of surface dipoles. Then, there is the second region in the graph shown in *Figure* ***55*** between 600 ppb and 2 ppm where the increase in electron affinity is stronger pronounced than below 600 ppb NO_2. This is most probably a result of the simultaneous adsorption of molecular NO_2 and the formation of nitrates. Nitrates, just like nitrites, are expected to form surface dipoles and would add to the increase in observable electron affinity change. The third region in the graph is observed for concentrations above 2 ppm. In this region, a constant increase in electron affinity is observed. It is difficult to say why

this might be the case, however, it is assumed that in this concentration range surface nitrates are the predominant species that adds to the increase in electron affinity.

5.3.5. Gas Sensing Mechanism of O_3

O_3 was investigated as a second oxidizing gas, partially due to the expected sensing mechanism. The sulfur vacancies of Bi_2S_3 were distinguished as the key reactive surface sites for the reaction with NO_2. In order to test whether this could be the predominant reaction site for oxidizing gases in general, Bi_2S_3 was exposed to O_3. For metal oxide-based gas sensors, the reported reaction mechanism with O_3 describes the oxidation of oxygen vacancies and the subsequent formation of O_2. Since it was observed that low NO_2 concentrations results in the healing of sulfur vacancies, it is expected to observe the same with O_3. This hypothesis was tested with the help of DRIFT spectroscopy once again by equilibrating the sensor in synthetic air followed by repeated exposures to 1.4 ppm O_3.

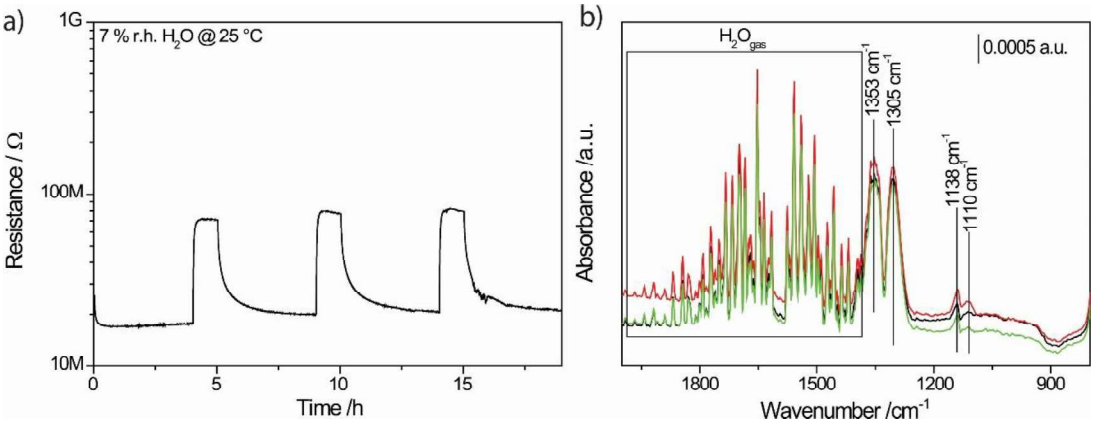

Figure 56: a) DC resistance measurement of a Bi_2S_3 sensors exposed to 1.4 ppm O_3 three times in a row; b) DIRFT spectra of the three O_3 pulses correlating to the DC resistance measurement in part a) of this figure (black – pulse 1, red – pulse 2, green – pulse 3). From [138].

The data in *Figure* ***56***a shows the increase in resistance resulting from the reaction of O_3 at the surface, the correlating spectral data during the respective O_3 exposures is shown in *Figure* ***56***b. Apart from a significant amount of gaseous water, which is a side product of the O_3 generation, two double bands can be clearly determined: one at 1353 and 1305 cm^{-1}, the other one at 1138 and 1110 cm^{-1}. There are reports that both double bands are indicative of adsorbed O_3 [151–154]. As of now, it is not possible to confirm whether the

adsorption of O_3 is followed by the formation of molecular O_2 and healing of sulfur vacancies. The formation of Bi-O bonds is not observable with the available DRIFT setup, and O_2 is not IR-active, and even if it were, the amount of O_2 formed due to the reaction with O_3 would be very low compared to the already present amount of O_2 in the test background. Therefore, experiments that could support the assumed reaction mechanism require either an IR setup that can measure the lower wavenumber range where the formation of Bi-O bands would be observed or a way to analyze the exhaust gas for O_2 in an experiment in a nitrogen background in order to make sure that the formation of O_2 will be observed. Neither setup was available in the lab at the time of this work. Therefore, an alternative way to support the assumed mechanism was chosen. The results are discussed in the upcoming section (section 5.3.6).

5.3.6. Competition Between O_3 and NO_2

The fact that the formation of Bi-O bands cannot be observed with the available DRIFT spectroscopy setup since the detector does not cover the needed wavenumber range, the possibilities to confirm the assumed reaction mechanism of both O_3 and NO_2 at the surface of Bi_2S_3, where sulfur vacancies are healed at the surface, are limited. The experiments with both oxidizing gases strongly indicate that the healing of sulfur vacancies is involved in the mechanism, however, definite experimental proof is missing. A way to further support the assumed reaction mechanisms with both oxidizing gases is the investigation of the competition between O_3 and NO_2. In the case that both gases heal sulfur vacancies as part of the reaction mechanism, one should see a decrease in the sensor response to either gas after the sensor was exposed to the other gas. This theory was tested by exposing the sensor to NO_2 and O_3 alternatingly.

*Figure **57*** shows the result of the competition experiment. The baseline resistance shows a relatively stable value, while the resistance in the presence of the oxidizing target gases shows some changes. The first exposure to 1.4 ppm NO_2 has a significantly higher response than the following four exposures. It is possible that this is already a result of the healed surface vacancies that need some time to recover. However, the response to NO_2 is relatively stable at around 6. The five exposures to NO_2 were followed by three exposures to 1.4 ppm O_3. The response to O_3 is lower than that to the same concentration

of NO_2, though stable at a value of around 4. The next four exposures are to 1.4 ppm NO_2 again and a significant decrease in response compared to the first five exposures to NO_2 is observed. This indicates that the reaction between NO_2 and Bi_2S_3 is inhibited by prior exposures to O_3. It should be noted that the subsequent exposure to O_3 does not seem to be influenced by exposures to NO_2 in between. The two O_3 exposures after the second set of NO_2 exposures appear to result in approximately the same response as before the NO_2 exposures. However, the response to NO_2 following the two O_3 exposures again shows a decrease in sensor response.

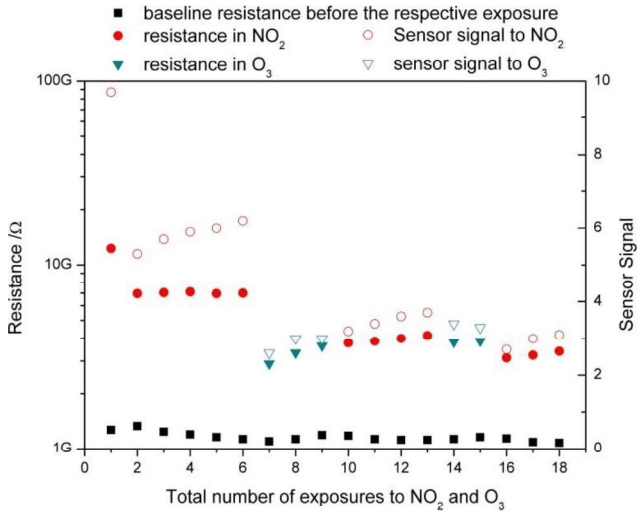

Figure 57: Resistance values and sensor signals of a Bi_2S_3 sensor exposed to 1.4 ppm NO_2 five times, followed by two exposures to O_3, four exposures to NO_2, two exposures to O_3 and finally three exposures to NO_2. From [138].

To investigate the underlying reaction with O_3 that inhibits the response of Bi_2S_3 to NO_2, the spectra recorded after the O_3 exposures were investigated. In cases where there are any remaining surface groups after the exposure to O_3 that are not related to the healed sulfur vacancies but could play a role in the inhibition of the reaction with NO_2, these spectra should reveal it.

*Figure **58*** shows the changes at the surface of Bi_2S_3 following each of the first three exposures to O_3. To obtain these spectra, the last recorded spectrum before the sensor was exposed to O_3 was used as a reference, while the spectrum in equilibrium after the exposure to O_3 was used to see how well the surface recovered after the exposure to O_3. Based on the spectra in *Figure **58*** it is not clearly distinguishable why the response to NO_2

is inhibited. The double band at 1138 cm^{-1} and 1110 cm^{-1} which was also observed during the exposure to O_3 does not fully recover indicating that a small amount of adsorbed O_3 sticks to the surface even after O_3 is removed from the system. Since it is assumed that O_3 adsorbs in sulfur vacancies this could explain the inhibition of the response to NO_2. However, it is more likely that the amount of healed sulfur vacancies far outweighs the small amount of adsorbed O_3 in sulfur vacancies and it is still assumed that the number of healed sulfur vacancies due to the exposure to O_3 are responsible for the decrease in the response to NO_2.

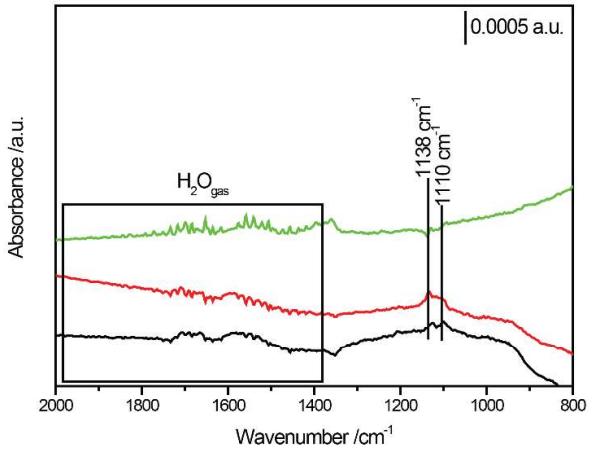

Figure 58: DRIFT spectra showing the changes at the surface following the exposure to 1.4 ppm O_3 (surface in equilibrium conditions after the exposure referenced to right before the exposure - both in dry synthetic air).

6. Summary

In the realm of this Thesis, two classes of materials were investigated with regard to their gas sensing characteristics when operated at temperatures below 100 °C: a noble metal loaded SMOX and two different semiconducting metal sulfides. The investigated SMOX material was WO_3 that was surface-loaded with Pt via SFRD. By using this method, it was possible to obtain WO_3 nanoparticles that were loaded with metallic Pt instead of the often-reported oxidized Pt. The investigation of this material was started during the author's Master's Thesis and continued during the presented Thesis. The focus was on the CO sensing mechanism with both the noble metal loaded WO_3 and the pristine WO_3 and on how the presence of Pt changes the surface reactions. Part of the material characterization was also done in the realm of this Thesis. The sensors were investigated in-situ at the synchrotron facility in Grénoble, France. During this beamtime it was found that the noble metal was mostly present in metallic form initially and stayed metallic even after operation in air. These results combined with the findings obtained with DRIFT spectroscopy revealed the spillover mechanism as sensing mechanism for the detection of CO with WO_3 loaded with metallic Pt.

When the pristine WO_3 sample was investigated under the same operation conditions, it was found that the exposure to low CO concentrations resulted in an increase in resistance which was unexpected since WO_3 is a n-type semiconductor and the exposure to CO, a reducing gas, was expected to result in a decrease in resistance, in case a response was observed. With the help of DRIFT spectroscopy and theoretical calculations found in literature, it was concluded that at 75 °C molecular oxygen adsorbed in surface oxygen vacancies and if exposed to CO, the molecular oxygen was split, effectively healing the surface vacancy while also oxidizing CO to CO_2.

The investigation of semiconducting metal sulfides was a topic that had not been discussed a lot in literature. Initial investigations were done on lead sulfide colloidal quantum dots. We had to realize that with this material the sensor preparation had a huge impact on the sensor performance, and it was difficult to obtain reproducible performances. Therefore, the first experiments that were done had the goal to produce

reliable sensors that showed reproducible results. Different techniques were tested for the sensor preparation as well as different ways to do the ligand exchange necessary for these colloidal quantum dots. These experiments resulted in the conclusion that spin coating was the method best suitable for sensor production with PbS CQDs.

Then, the sensors were investigated for their sensing performance. It was found that sensors made from PbS CQDs lacked a response to every tested volatile organic compound, however showed good responses to NO_2. Repeated exposures to NO_2 revealed severe instability of the sensor, both in terms of sensor response and baseline stability. With the help of DRIFT spectroscopy, it was found that the ligand exchange was not effective enough to remove all of the organic ligand from the surface. Further, it was concluded that the residual organic ligand played a key role in both the ageing and sensing mechanisms. The reaction between NO_2 and oleic acid (the organic ligand that was used to stabilize the CQDs after the synthesis) resulted in the formation of byproducts that 1) initially induced a higher sensor response than NO_2 would have done on its own and 2) the organic reaction products got stuck on the surface of the CQDs resulting in the formation of an insulating shell around the semiconducting CQD which was observed as an increase in baseline resistance. This was confirmed by producing new sensors with an improved ligand exchange procedure. The samples were again investigated with DRIFT spectroscopy, and it was found that NO_2 adsorbed at the surface, directly resulting in a charge transfer observed as a decrease in resistance, while at the same time the formation of $Pb(NO_3)_2$ was observed which resulted in a steady and slow increase in baseline resistance.

The second semiconducting metal sulfide that was investigated was Bi_2S_3. There was and still is even less literature on Bi_2S_3 and its sensing capabilities than on PbS. Additionally, the little literature that exists contradicts each other with regard to selectivity and sensitivity. Just like the PbS sensors, the Bi_2S_3 sensors were produced via spin coating including a ligand exchange procedure. The initial experiments with these sensors revealed a selective response to NO_2 over CO, H_2, ethanol, toluene and acetone that was independent of humidity. The sensing mechanism was investigated with the help of Kelvin Probe measurements as well as DRIFT spectroscopy. It was found that the NO_2 sensing mechanism of Bi_2S_3 changed depending on the NO_2 concentration. While low NO_2

concentrations resulted in an increase in resistance due to healing of sulfur vacancies at the surface, in higher concentrations a drop in resistance was observed due to the subsequent formation of nitrates involving the healed sulfur vacancies with oxygen. A further increase in NO_2 concentration resulted in a constant battle of a release and uptake of electrons, and the resistance basically remained constant. Since the available DRIFT setup was not capable of measuring the wavenumber range in which the formation of Bi-O bonds would be observed, the obtained experimental results could not prove beyond a doubt that the suggested mechanism is correct. Therefore, the sensing mechanism to a second oxidizing gas was investigated, namely O_3. The O_3 sensing mechanism for SMOX based sensors that can be found in literature suggests a similar mechanism as was suggested for the reaction of NO_2 at the surface of Bi_2S_3: surface oxygen vacancies are healed by O_3 under formation of O_2. While the limitation of the DRIFT setup remained the same (the formation of Bi-O cannot be observed), it was assumed that O_3 and NO_2 would compete for the same reaction sites, the surface sulfur vacancies. If this were the case, an inhibition of the sensor response would be expected. And indeed, the sensor response to NO_2 after it was exposed to O_3 decreased. While this is still no definite proof of the suggested mechanism, it was taken as another indication in support of the suggested NO_2 mechanism.

In summary, both materials showed promise for the development of chemo resistive gas sensors operatable at low temperatures. WO_3 loaded with metallic Pt showed high responses to CO when operated at 75 °C while no response to acetone and toluene was low. The response to ethanol was lower than the response to CO which is exciting since the response to ethanol usually far exceeds the response to CO. The metal sulfides showed selectivity for oxidizing gases. Both PbS (at room temperature) and Bi_2S_3 (at 50 °C) showed no response to any of the reducing gases that were tested while they showed good responses to NO_2, and Bi_2S_3 also to O_3. PbS, however, also displayed severe instability when exposed to NO_2 multiple times. Bi_2S_3 did not display the same instability but showed a concentration dependent sensing mechanism to NO_2 in addition to an inhibition of the signal when the material was exposed to O_3. Both metal sulfides showed limitations, however, but also promise that is worth to be further investigated.

7. Outlook

There are still a lot of unknowns where the investigated materials, their sensing behavior and mechanisms are concerned. Especially the class of semiconducting metal sulfides is a relatively new class of materials used in gas sensing devices. There is not a lot of literature and some of the literature contradicts each other. While the results obtained with Bi_2S_3 seemed promising, there is still a lot of work to be done. It starts with finding definite proof of the here suggested mechanism. In discussions with other scientists, XPS was often mentioned as a possible tool to confirm the mechanism. However, the experiment would have to be planned carefully. It was observed that the Bi_2S_3 fully recovered if left in room air for less than 2 weeks. If the samples were held in vacuum, which would be the case in an XPS (especially during transfer which can require extended time periods), it would be unlikely that the healed sulfur vacancies would stay healed. This experiment would have to be carefully planned, preferably in a system that can take low gas pressures (near ambient pressure XPS).

The number of available semiconducting metal sulfides is vast. While PbS seemed not very promising in terms of stability and strength of sensor response, Bi_2S_3 showed promising results. First experiments with SnS_2 (neither shown in this Thesis nor published) indicated a very interesting behavior as it was found that the type of response changed based on the temperature. This means while at room temperature the response showed p-type behavior, it switched to n-type behavior when increasing the temperature to 100 °C. Overall, the influence of the temperature on the sensing behavior was not investigated. Considering the results obtained with SnS_2, this should certainly be on the list of future experiments.

8. References

[1] K. Izawa, H. Ulmer, A. Staerz, U. Weimar, N. Barsan, Application of SMOX-based sensors, in: N. Barsan, K. Schierbaum (Eds.), Gas Sensors Based on Conducting Metal Oxides, Elsevier Inc., 2018: pp. 217–251.

[2] W. Irving, O. Tailakov, D. Kruger, D. Williams, CH4 Emissions: Coal Mining and Handling, IPCC Good Practice and Uncertainty Management in National Greenhouse Gas Inventories. (2001) 129–144.

[3] T. Seiyama, A. Kato, K. Fujiishi, M. Nagatani, A New Detector for Gaseous Components Using Semiconductive Thin Films, Anal. Chem. 34 (1962) 1502–1503.

[4] N. Barsan, D. Koziej, U. Weimar, Metal oxide-based gas sensor research: How to?, Sens Actuators B Chem. 121 (2007) 18–35. https://doi.org/10.1016/j.snb.2006.09.047.

[5] N. Taguchi, Gas-Detecting Device, 3,631,436, 1971.

[6] A. Staerz, X. Gao, F. Cetmi, Z. Ming, U. Weimar, T. Zhang, N. Barsan, Dominant Role of Heterojunctions in Gas Sensing with Composite Materials, ACS Appl Mater Interfaces. 12 (2020) 21127–21132. https://doi.org/10.1021/acsami.0c05173.

[7] J.H. Kim, A. Katoch, S.S. Kim, Optimum shell thickness and underlying sensing mechanism in p-n CuO-ZnO core-shell nanowires, Sens Actuators B Chem. 222 (2016) 249–256. https://doi.org/10.1016/j.snb.2015.08.062.

[8] A. Staerz, I. Boehme, D. Degler, M. Bahri, D.E. Doronkin, A. Zimina, H. Brinkmann, S. Herrmann, B. Junker, O. Ersen, J.-D. Grunwaldt, U. Weimar, N. Barsan, Rhodium Oxide Surface-Loaded Gas Sensors, Nanomaterials. 8 (2018) 892. https://doi.org/10.3390/nano8110892.

[9] G. Hui, M. Zhu, X. Yang, J. Liu, G. Pan, Z. Wang, Highly sensitive ethanol gas sensor based on CeO2/ZnO binary heterojunction composite, Mater Lett. 278 (2020). https://doi.org/10.1016/j.matlet.2020.128453.

[10] J. Fang, Y. Zhu, D. Wu, C. Zhang, X. Shaohui, D. Xiong, P. Yang, L. Wang, P.K. Chu, Gas sensing properties of NiO/SnO2 heterojunction thin film, Sens Actuators B Chem. 252 (2017) 1163–1168.

[11] D. Degler, U. Weimar, N. Barsan, Current Understanding of the Fundamental Mechanisms of Doped and Loaded Semiconducting Metal-Oxide-Based Gas Sensing Materials, ACS Sens. 4 (2019) 2228–2249. https://doi.org/10.1021/acssensors.9b00975.

[12] D. Degler, S.A. Müller, D.E. Doronkin, D. Wang, J.D. Grunwaldt, U. Weimar, N. Barsan, Platinum loaded tin dioxide: A model system for unravelling the interplay between heterogeneous catalysis and gas sensing, J Mater Chem A Mater. (2018). https://doi.org/10.1039/c7ta08781k.

[13] G. Korotcenkov, V. Brinzari, L.B. Gulina, B.K. Cho, The influence of gold nanoparticles on the conductivity response of SnO 2 -based thin film gas sensors, Appl Surf Sci. 353 (2015) 793–803. https://doi.org/10.1016/j.apsusc.2015.06.192.

[14] J. Ma, Y. Ren, X. Zhou, L. Liu, Y. Zhu, X. Cheng, P. Xu, X. Li, Y. Deng, D. Zhao, Pt Nanoparticles Sensitized Ordered Mesoporous WO3 Semiconductor: Gas Sensing Performance and Mechanism Study, Adv Funct Mater. 1705268 (2017) 1–12. https://doi.org/10.1002/adfm.201705268.

[15] M. Penza, C. Martucci, G. Cassano, NOx gas sensing characteristics of WO_3 thin films activated by noble metals (Pd, Pt, Au) layers, Sens Actuators B Chem. 50 (1998) 52–59. https://doi.org/10.1016/S0925-4005(98)00156-7.

[16] R. Ionescu, E.H. Espinosa, R. Leghrib, A. Felten, J.J. Pireaux, R. Erni, G. Van Tendeloo, C. Bittencourt, N. Cañellas, E. Llobet, Novel hybrid materials for gas sensing applications made of metal-decorated MWCNTs dispersed on

nano-particle metal oxides, Sens Actuators B Chem. 131 (2008) 174–182. https://doi.org/10.1016/j.snb.2007.11.001.

[17] E.H. Espinosa, R. Ionescu, E. Llobet, A. Felten, C. Bittencourt, E. Sotter, Z. Topalian, P. Heszler, C.G. Granqvist, J.J. Pireaux, X. Correig, Highly Selective NO[sub 2] Gas Sensors Made of MWCNTs and WO[sub 3] Hybrid Layers, J Electrochem Soc. 154 (2007) J141. https://doi.org/10.1149/1.2667855.

[18] M.H. Raza, K. Movlaee, S.G. Leonardi, N. Barsan, G. Neri, N. Pinna, Gas Sensing of NiO-SCCNT Core–Shell Heterostructures: Optimization by Radial Modulation of the Hole-Accumulation Layer, Adv Funct Mater. 30 (2020) 1906874. https://doi.org/10.1002/adfm.201906874.

[19] T. Han, A. Nag, S.C. Mukhapodhyay, Y. Xu, Carbon nanotubes and its gas-sensing applications : A review, Sens Actuators A Phys. 291 (2019) 107–143.

[20] M. Fleischer, S. Kornely, T. Weh, J. Frank, H. Meixner, Selective gas detection with high-temperature operated metal oxides using catalytic filters, Sens Actuators B Chem. 69 (2000) 205–210. https://doi.org/10.1016/S0925-4005(00)00513-X.

[21] J. Rebholz, K. Grossmann, D. Pham, S. Pokhrel, L. Mädler, U. Weimar, N. Barsan, Selectivity enhancement by using double-layer mox-based gas sensors prepared by flame spray pyrolysis (FSP), Sensors (Switzerland). 16 (2016) 1437. https://doi.org/10.3390/s16091437.

[22] T. Sahm, W. Rong, N. Bârsan, L. Mädler, S.K. Friedlander, U. Weimar, Formation of multilayer films for gas sensing by in situ thermophoretic deposition of nanoparticles from aerosol phase, J Mater Res. 22 (2007) 850–857. https://doi.org/10.1557/jmr.2007.0106.

[23] T. Fu, Research on gas-sensing properties of lead sulfide-based sensor for detection of NO2 and NH3 at room temperature, Sens Actuators B Chem. 140 (2009) 116–121. https://doi.org/10.1016/j.snb.2009.03.075.

[24] H. Kan, M. Li, Z. Song, S. Liu, B. Zhang, J. Liu, M.Y. Li, G. Zhang, S.L. Jiang, H. Liu, Highly sensitive response of solution-processed bismuth sulfide nanobelts for room-temperature nitrogen dioxide detection, J Colloid Interface Sci. 506 (2017) 102–110. https://doi.org/10.1016/j.jcis.2017.07.012.

[25] V. Guidi, B. Fabbri, A. Gaiardo, S. Gherardi, A. Giberti, C. Malagù, G. Zonta, P. Bellutti, Metal sulfides as a new class of sensing materials, Procedia Eng. 120 (2015) 138–141. https://doi.org/10.1016/j.proeng.2015.08.586.

[26] S.Z. and Z.W. F.Tan, S. Qu, J. Wu, K. Liu, Preparation of SnS2 colloidal quantum dots and their application in organic/inorganic hybrid solar cells, Tan et al. Nanoscale Research Letters. Vol.298 (2011) No.6 ,p.p. 1-8.

[27] H. Liu, M. Li, O. Voznyy, L. Hu, Q. Fu, D. Zhou, Z. Xia, E.H. Sargent, J. Tang, Physically Flexible, Rapid-Response Gas Sensor Based on Colloidal Quantum Dot Solids, Advanced Materials. 26 (2014) 2718–2724. https://doi.org/10.1002/adma.201304366.

[28] A. Mosahebfard, H.D. Jahromi, M.H. Sheikhi, Highly Sensitive, Room Temperature Methane Gas Sensor Based on Lead Sulfide Colloidal Nanocrystals, IEEE Sens J. 16 (2016) 4174–4179. https://doi.org/10.1109/JSEN.2016.2546966.

[29] M. Li, W. Zhang, G. Shao, H. Kan, Z. Song, S. Xu, H. Yu, S. Jiang, H. Liu, Sensitive NO2 gas sensors employing spray-coated colloidal quantum dots, Thin Solid Films. 618 (2016) 6–11. https://doi.org/10.1016/j.tsf.2016.08.023.

[30] R.D. Ladhe, P.K. Baviskar, W.W. Tan, J.B. Zhang, C.D. Lokhande, B.R. Sankapal, LPG sensor based on complete inorganic n-Bi2S 3-p-CuSCN heterojunction synthesized by a simple chemical route, J Phys D Appl Phys. 43 (2010) 245302. https://doi.org/10.1088/0022-3727/43/24/245302.

[31] K.W. Kolasinski, Chemisorption, Physisorption and Dynamics, in: Surface Science: Foundations of Catalysis and Nanoscience, 3rd ed., 2012: pp. 115–183. https://doi.org/10.1002/9781119941798.ch3.

[32] K. Hauffe, S.R. Morrision, Adsorption - Eine Einführung in die Probleme der Adsorption, Walter de Gruyter, Berlin - New York, 1974. https://doi.org/10.1515/9783110842395.

[33] N. Barsan, D. Degler, U. Guth, A. Hemeryck, K. Izawa, J.-H. Lee, A. Oprea, J. Rebholz, K. Schierbaum, A. Staerz, H. Ulmer, U. Weimar, H.-D. Wiemhöfer, Gas Sensors Based on Conducting Metal Oxides - Basic Understanding, Technology and Application, 2019.

[34] P. Atkins, J.D.E. Paula, Physical Chemistry, 8th ed., Oxford University Press, 2006.

[35] M. Anpo, N. Barsan, E. Bordes-Richard, L.E. Briand, G. Busca, G. Centi, M. Cherian, P. Courtine, G. Deo, D.P. Dissanayake, S. Dohshi, J.L.G. Fierro, A. Gurlo, Y. Hu, Y. Inoue, J.T.S. Irvine, S. Ishihara, Y.-I. Kim, M. Kitano, A. Kruth, I.S. Metcalfe, H. Mizoguchi, J.C. Mol, R.M. Navarro, E.K. Novakova, B. Pawelec, M.A. Pena, S. Perathoner, T.V.M. Rao, B.M. Reddy, S.A. Schunk, F. Schüth, M.W. Stoltzfus, S. Tao, A. Thursfield, J.C. Védrine, I.E. Wachs, Z.L. Wang, U. Weimar, M.S. Wong, P.M. Woodward, Metal Oxides - Chemistry and Applications, 1st ed., Taylor & Francis, 2006.

[36] N. Bârsan, Transduction in semiconducting metal oxide based gas sensors - implications of the conduction mechanism, Procedia Eng. 25 (2011) 100–103. https://doi.org/10.1016/j.proeng.2011.12.025.

[37] N. Barsan, U. Weimar, Conduction model of metal oxide gas sensors, J Electroceram. 7 (2001) 143–167. https://doi.org/10.1023/A:1014405811371.

[38] N. Barsan, D. Koziej, U. Weimar, Metal oxide-based gas sensor research : How to?, Sens Actuators B Chem. 121 (2007) 18–35. https://doi.org/10.1016/j.snb.2006.09.047.

[39] N. Yamazoe, Y. Kurokawa, T. Seiyama, Effects of additives on semiconductor gas sensors, Sensors and Actuators. (1983). https://doi.org/10.1016/0250-6874(83)85034-3.

[40] S. Matsushima, Y. Teraoka, N. Miura, N. Yamazoe, Electronic Interaction between Metal Additives and Tin Dioxide in Tin Dioxide-Based Gas Sensors, Jpn J Appl Phys. 27 (1988) 1798–1802. https://doi.org/10.1143/JJAP.27.1798.

[41] K. Großmann, S. Wicker, U. Weimar, N. Barsan, Impact of Pt additives on the surface reactions between SnO2, water vapour, CO and H2; an operando investigation, Physical Chemistry Chemical Physics. 15 (2013) 19151. https://doi.org/10.1039/c3cp52782d.

[42] K. Großmann, J. Rebholz, R. Pavelko, N. Barsan, U. Weimar, Influence of Pd and Pt doping concerning the sensing mechanism, in: IMCS - The 14th International Meeting on Chemical Sensors, 2012: pp. 465–467. https://doi.org/10.5162/IMCS2012/5.3.4.

[43] M. Hübner, D. Koziej, J.-D. Grunwaldt, U. Weimar, N. Barsan, An Au clusters related spill-over sensitization mechanism in SnO2-based gas sensors identified by operando HERFD-XAS, work function changes, DC resistance and catalytic conversion studies., Phys Chem Chem Phys. 14 (2012) 13249–13254. https://doi.org/10.1039/c2cp41349c.

[44] F. Wang, C. Di Valentin, G. Pacchioni, Electronic and Structural Properties of WO_3: A Systematic Hybrid DFT Study, The Journal of Physical Chemistry C. 115 (2011) 8345–8353. https://doi.org/10.1021/jp201057m.

[45] M. Weil, Wolf.D. Schubert, The beautiful colours of tungsten oxides, ITIA Newsletter. (2013) 1–12.

[46] A. Staerz, S. Somacescu, M. Epifani, T. Kida, U. Weimar, N. Barsan, WO3-Based Gas Sensors: Identifying Inherent Qualities and Understanding the Sensing Mechanism, ACS Sens. 5 (2020) 1624–1633. https://doi.org/10.1021/acssensors.0c00113.

[47] T. Samerjai, N. Tamaekong, C. Liewhiran, A. Wisitsoraat, A. Tuantranont, S. Phanichphant, Selectivity towards H2 gas by flame-made Pt-loaded WO3 sensing films, Sens Actuators B Chem. 157 (2011) 290–297. https://doi.org/10.1016/j.snb.2011.03.065.

[48] T. Samerjai, N. Tamaekong, C. Liewhiran, a Wisitsoraat, S. Phanichphant, N. Program, C. Mai, C. Mai, C. Mai, M. Science, C. Mai, Pt-loaded WO 3 Thick Films for NO 2 Gas sensing, (2012) 754–757. https://doi.org/10.5162/IMCS2012/P1.0.3.

[49] J. Wang, Z. Wang, C.-J. Liu, Enhanced Activity for CO Oxidation over WO3 Nanolamella Supported Pt Catalyst, ACS Appl Mater Interfaces. 6 (2014) 12860–12867. https://doi.org/10.1021/am502807b.

[50] H.G. Moon, Y.R. Choi, Y.S. Shim, K. Il Choi, J.H. Lee, J.S. Kim, S.J. Yoon, H.H. Park, C.Y. Kang, H.W. Jang, Extremely sensitive and selective NO probe based on villi-like WO3nanostructures for application to exhaled breath analyzers, ACS Appl Mater Interfaces. 5 (2013) 10591–10596. https://doi.org/10.1021/am402456s.

[51] S.J. Choi, I. Lee, B.H. Jang, D.Y. Youn, W.H. Ryu, C.O. Park, I.D. Kim, Selective diagnosis of diabetes using Pt-functionalized WO3 hemitube networks as a sensing layer of acetone in exhaled breath, Anal Chem. 85 (2013) 1792–1796. https://doi.org/10.1021/ac303148a.

[52] M. Horprathum, T. Srichaiyaperk, B. Samransuksamer, A. Wisitsoraat, P. Eiamchai, S. Limwichean, C. Chananonnawathorn, K. Aiempanakit, N. Nuntawong, V. Patthanasettakul, C. Oros, S. Porntheeraphat, P. Songsiriritthigul, H. Nakajima, A. Tuantranont, P. Chindaudom, Ultrasensitive

hydrogen sensor based on Pt-decorated WO3 nanorods prepared by glancing-angle dc magnetron sputtering, ACS Appl Mater Interfaces. 6 (2014) 22051–22060. https://doi.org/10.1021/am505127g.

[53] P.J. Shaver, Activated Tungsten Oxide Gas Detectors, Appl Phys Lett. 11 (1967) 255–257.

[54] S. Park, H. Kim, C. Jin, S.-W. Choi, S.S. Kim, C. Lee, Enhanced CO gas sensing properties of Pt-functionalized WO3 nanorods, Thermochim Acta. 542 (2012) 69–73. https://doi.org/10.1016/j.tca.2011.12.002.

[55] Y. Wang, J. Liu, X. Cui, Y. Gao, J. Ma, Y. Sun, P. Sun, F. Liu, X. Liang, T. Zhang, G. Lu, NH3 gas sensing performance enhanced by Pt-loaded on mesoporous WO3, Sens Actuators B Chem. 238 (2017) 473–481. https://doi.org/10.1016/j.snb.2016.07.085.

[56] J. Zhang, X. Liu, M. Xu, X. Guo, S. Wu, S. Zhang, S. Wang, Pt clusters supported on WO3 for ethanol detection, Sens Actuators B Chem. 147 (2010) 185–190. https://doi.org/10.1016/j.snb.2010.03.017.

[57] Y. Shen, B. Zhang, X. Cao, D. Wei, J. Ma, L. Jia, S. Gao, B. Cui, Y. Jin, Microstructre and enhanced H2S sensing properties of Pt-loaded WO3 thin films, Sens Actuators B Chem. 193 (2014) 273–279. http://dx.doi.org/10.1016/j.snb.2014.12.010.

[58] T. Li, Y. Shen, X. Zhong, S. Zhao, G. Li, B. Cui, D. Wei, K. Wei, Effect of noble metal element on microstructure and NO2 sensing properties of WO3 nanoplates prepared from a low-grade scheelite concentrate, J Alloys Compd. 818 (2020) 152927. https://doi.org/10.1016/j.jallcom.2019.152927.

[59] T. Ruß, Low Temperature Operated Tungsten Trioxide Based Gas Sensors Loaded With Platinum, Eberhard Karls University of Tuebingen, Germany, 2018.

[60] J. Jamin, Supercritical Fluid Reactive Deposition (SFRD) of platinum particles on metal oxide support materials and application in gas sensing, Karlsruhe Institute of Technology and Eberhard Karls University Tuebingen, 2018.

[61] E.H. Putley, J.B. Arthur, Lead sulphide - An intrinsic semiconductor, Proceedings of the Physical Society. Section B. 64 (1951) 616–618. https://doi.org/10.1088/0370-1301/64/7/110.

[62] P. Nowak, K. Laajalehto, I. Kartio, A flotation related X-ray photoelectron spectroscopy study of the oxidation of galena surface, Colloids Surf A Physicochem Eng Asp. 161 (2000) 447–460. https://doi.org/10.1016/S0927-7757(99)00214-9.

[63] K.C. Pillai, V.Y. Young, J.O.M. Bockris, XPS studies of xanthate adsorption on galena surfaces, Applications of Surface Science. 16 (1983) 322–344. https://doi.org/10.1016/0378-5963(83)90077-6.

[64] S.R. Grano, C.A. Prestidge, J. Ralston, Sulphite modification of galena surfaces and its effect on galena flotation and xanthate adsorption, Int J Miner Process. 52 (1997) 1–29. https://doi.org/10.1016/s0301-7516(97)00066-5.

[65] D. Fornasiero, F. Li, J. Ralston, R.S.C. Smart, Oxidation of Galena Surfaces, J Colloid Interface Sci. 164 (1994) 333–344.

[66] Minerals. net-T.M.& G. Kingdom, The Mineral Galena, (2022). https://www.minerals.net/mineral/galena.aspx.

[67] W.W. Scanlon, Recent Advances in the Optical and Electronic Properties of PbS, PbSe, PbTe and their Alloys, Journal of Physics and Chemistry of Solids. 8 (1959) 423–428. https://doi.org/10.1016/0022-3697(59)90379-8.

[68] R. Sakthi Sudar Saravanan, M. Meena, D. Pukazhselvan, C.K. Mahadevan, Structural, optical and electrical characterization of Mn2+ and Cd2+

doped/co-doped PbS nanocrystals, J Alloys Compd. 627 (2015) 69–77. https://doi.org/10.1016/j.jallcom.2014.12.008.

[69] S.I. Sadovnikov, A.I. Gusev, Structure and properties of PbS films, J Alloys Compd. 573 (2013) 65–75. https://doi.org/10.1016/j.jallcom.2013.03.290.

[70] R. Kumar, R. Das, M. Gupta, V. Ganesan, Preparation of nanocrystalline Sb doped PbS thin films and their structural, optical, and electrical characterization, Superlattices Microstruct. 75 (2014) 601–612. https://doi.org/10.1016/j.spmi.2014.08.019.

[71] J. Tang, L. Brzozowski, D.A.R. Barkhouse, X. Wang, R. Debnath, R. Wolowiec, E. Palmiano, L. Levina, A.G. Pattantyus-Abraham, D. Jamakosmanovic, Quantum Dot Photovoltaics in the Extreme Quantum Confinement Regime: The Surface-Chemical Origins of Exceptional Air- and Light-Stability, ACS Nano. 4 (2010) 869–878. https://doi.org/10.1021/nn901564q.

[72] S.I. Sadovnikov, A.A. Rempel, A.I. Gusev, Nanostructured Lead , Cadmium , and Silver Sulfides - Structure, Nonstoichiometry and Properties, 2018. https://doi.org/10.1007/978-3-319-56387-9.

[73] S.A. Mcdonald, G. Konstantatos, S. Zhang, P.W. Cyr, E.J.D. Klem, L. Levina, E.H. Sargent, Solution-processed PbS quantum dot infrared photodetectors and photovoltaics, Nat Mater. 4 (2005) 138–142. https://doi.org/10.1038/nmat1299.

[74] T. Blachowicz, A. Ehrmann, Recent Developments of Solar Cells from PbS Colloidal Quantum Dots, Applied Sciences (Switzerland). 10 (2020) 1743. https://doi.org/10.3390/app10051743.

[75] H. Tavakoli Dastjerdi, P. Qi, Z. Fan, M.M. Tavakoli, Cost-Effective and Semi-Transparent PbS Quantum Dot Solar Cells Using Copper Electrodes, ACS Appl Mater Interfaces. 12 (2020) 818–825. https://doi.org/10.1021/acsami.9b18487.

[76] S. Zheng, J. Chen, E.M.J. Johansson, X. Zhang, PbS Colloidal Quantum Dot Inks for Infrared Solar Cells, IScience. 23 (2020) 1–19. https://doi.org/10.1016/j.isci.2020.101753.

[77] A. De Iacovo, L. Colace, L. Scopa, S. Foglia, Near infrared photodetectors based on PbS colloidal quantum dots, Proc. of SPIE. 9899 (2016) 989908. https://doi.org/10.1117/12.2224958.

[78] A. De Iacovo, C. Venettacci, L. Colace, L. Scopa, S. Foglia, PbS Colloidal Quantum Dot Photodetectors operating in the Near Infrared, Sci Rep. 6 (2016) 37913. https://doi.org/10.1038/srep37913.

[79] G. Konstantatos, I. Howard, A. Fischer, S. Hoogland, J. Clifford, E. Klem, L. Levina, E.H. Sargent, Ultrasensitive solution-cast quantum dot photodetectors, Nature Letters. 442 (2006) 180–183. https://doi.org/10.1038/nature04855.

[80] S.T. Navale, D.K. Bandgar, M.A. Chougule, V.B. Patil, Facile method of preparation of PbS films for NO2 detection, RSC Adv. 5 (2015) 6518–6527. https://doi.org/10.1039/C4RA15644G.

[81] N.B.B. Sonawane, P.K.K. Baviskar, R.R.R. Ahire, B.R.R. Sankapal, CdO necklace like nanobeads decorated with PbS nanoparticles: Room temperature LPG sensor, Mater Chem Phys. 191 (2017) 168–172. https://doi.org/10.1016/j.matchemphys.2017.01.011.

[82] H. Liu, M. Li, G. Shao, W. Zhang, W. Wang, H. Song, H. Cao, W. Ma, J. Tang, Enhancement of hydrogen sulfide gas sensing of PbS colloidal quantum dots by remote doping through ligand exchange, Sens Actuators B Chem. 212 (2015) 434–439. https://doi.org/10.1016/j.snb.2015.02.047.

[83] Y. Liu, L. Wang, H. Wang, M. Xiong, T. Yang, G.S. Zakharova, Highly sensitive and selective ammonia gas sensors based on PbS quantum dots/TiO2 nanotube arrays at room temperature, Sens Actuators B Chem. 236 (2016) 529–536. https://doi.org/10.1016/j.snb.2016.06.037.

[84] S. Kaci, A. Keffous, S. Hakoum, A. Mansri, Hydrogen sensitivity of the sensors based on nanostructured lead sulfide thin films deposited on a-SiC:H and p-Si(100) substrates, Vacuum. 116 (2015) 27–30. https://doi.org/10.1016/j.vacuum.2015.02.024.

[85] M. Li, D. Zhou, J. Zhao, Z. Zheng, J. He, L. Hu, Z. Xia, J. Tang, H. Liu, Resistive gas sensors based on colloidal quantum dot (CQD) solids for hydrogen sulfide detection, Sens Actuators B Chem. 217 (2015) 198–201. https://doi.org/10.1016/j.snb.2014.07.058.

[86] P. Atkins, J. de Paula, Atkins' Physical Chemistry, 10th ed., Oxford University Press, 2014.

[87] E. Pineda, M.E. Nicho, P.K. Nair, H. Hu, Optoelectronic properties of chemically deposited Bi2S3 thin films and the photovoltaic performance of Bi2S3/P3OT solar cells, Solar Energy. 86 (2012) 1017–1022. https://doi.org/10.1016/j.solener.2011.06.015.

[88] N.C. Miller, M. Bernechea, Research Update: Bismuth based materials for photovoltaics, APL Mater. 6 (2018) 084503. https://doi.org/10.1063/1.5026541.

[89] J. Arumugam, A. George, A.D. Raj, A.A. Irudayaraj, R.L. Josephine, S.J. Sundaram, T. Saad Algarni, A.M. Al-Mohaimeed, B. Balasubramanian, K. Kaviyarasu, Improved Ag doped Bi2S3 nanowire-based photodiode: Fabrication and performance, Mater Lett. 302 (2021) 130403. https://doi.org/10.1016/j.matlet.2021.130403.

[90] M.S. Kumar, S.P. Madhusudanan, K. Mohanta, S.K. Batabyal, Development and characterization of photodiode from p-Cu2CdSnS4/n-Bi2S3 heterojunction, Mater Res Express. 7 (2020) 015909. https://doi.org/10.1088/2053-1591/ab65e1.

[91] I. Uddin, A. Ahmad, E.A. Siddiqui, Sk.H. Rahaman, S. Gambhir, Biosynthesis of Fluorescent Bi2S3 Nanoparticles and their Application as Dual-Function

SPECT-CT Probe for Animal Imaging, Curr Top Med Chem. 16 (2016) 2019–2025. https://doi.org/10.2174/1568026616666160215155347.

[92] Y. Zu, Y. Yong, X. Zhang, J. Yu, X. Dong, W. Yin, L. Yan, F. Zhao, Z. Gu, Y. Zhao, Protein-directed synthesis of Bi2S3 nanoparticles as an efficient contrast agent for visualizing the gastrointestinal tract, RSC Adv. 7 (2017) 17505–17513. https://doi.org/10.1039/c7ra01526g.

[93] K. Yao, W.W. Gong, Y.F. Hu, X.L. Liang, Q. Chen, L.-M. Peng, Individual Bi2S3 Nanowire-Based Room-Temperature H2 Sensor, Journal of Physical Chemistry C. 112 (2008) 8721–8724. https://doi.org/10.1021/jp8022293.

[94] X. Yang, S. Tian, R. Li, W. Wang, S. Zhou, Use of single-crystalline Bi2S3 nanowires as room temperature ethanol sensor synthesized by hydrothermal approach, Sens Actuators B Chem. 241 (2017) 210–216. https://doi.org/10.1016/j.snb.2016.10.074.

[95] T.-X. Fu, Gas sensor based on three dimensional Bi2S3 nanowires network for ammonia detection at room temperature, Mater Res Bull. 99 (2018) 460–465. https://doi.org/10.1016/j.materresbull.2017.11.038.

[96] S. Wicker, M. Guiltat, U. Weimar, A. Hémeryck, N. Barsan, Ambient Humidity Influence on CO Detection with SnO2 Gas Sensing Materials. A Combined DRIFTS/DFT Investigation, Journal of Physical Chemistry C. 121 (2017) 25064–25073. https://doi.org/10.1021/acs.jpcc.7b06253.

[97] B. Junker, M. Favaro, D.E. Starr, M. Hävecker, U. Weimar, N. Barsan, NAP-XPS as a new tool for in-situ studies of SMOX gas sensors, J Phys D Appl Phys. 55 (2022) 064002. https://doi.org/10.1088/1361-6463/ac3283.

[98] B.C. Smith, Fundamentals of Fourier Transform Infrared Spectroscopy, 2nd Editio, Boca Raton, 2011. https://doi.org/https://doi.org/10.1201/b10777.

[99] G. Agostini, G. Aquilanti, G. Artioli, A. Balerna, A. Baraldi, J. Baruchel, M. Benfatto, C.M. Bertoni, M. Bolognesi, F. Bonino, F. Boscherini, J.-Y. Buffiere,

F. Capotondi, G. De Giudici, M. Dell'Angela, D. Eichert, P. Fornasini, E. Gallo, L. Gelisio, F. Giannici, D. Gianolio, A. Goldoni, E. Groppo, C. Lamberti, P. Lattanzi, A. Locatelli, A. Longo, S. Lupi, M. Malvestuto, G. Margaritondo, C. Mariani, A. Martorana, D. Medas, C. Meneghini, T.O. Mentes, L. Mino, S. Mobilio, G. Monaco, M. Nadrini, L. Paolasini, F. Parmigiani, S. Pascarelli, A. Percchi, A. Piovano, J.R. Plaisier, S. Polizzi, C. Prestipino, S. Quartieri, G. Rossi, P. Scardi, F. Spinozzi, G. Stefani, G. Tromba, L. Vaccari, D. Viterbo, G. Zanotti, Synchrotron Radiation - Basics, Methods and Applications, Springer, 2015. https://doi.org/https://doi.org/10.1007/978-3-642-55315-8.

[100] B. Ravel, Introduction to X-ray Absorption Spectroscopy, 2015. https://www.bnl.gov/nsls2/userguide/lectures/lecture-4-ravel.pdf (accessed March 16, 2022).

[101] F. Boscherini, G. Ciatto, F. D'Acapito, A. Di Cicco, A. Filipponi, P. Fornasini, A.A. Guda, R. Gunnella, S.M. Heald, M. Katsikini, A. V. Kolobov, K. Lawniczak-Jablonska, M.C. Ridgway, C.S. Schnohr, T.-K. Sham, A. V. Soldatov, M.A. Soldatov, X. Sun, X-Ray Absorption Spectroscopy of Semiconductors, Springer, 2015. https://doi.org/https://doi.org/10.1007/978-3-662-44362-0.

[102] P. V. Evstigneeva, A.L. Trigub, D.A. Chareev, M.S. Nickolsky, B.R. Tagirov, The Charge State of Pt in Binary Compounds and Synthetic Minerals Determined by X-ray Absorption Spectroscopy and Quantum Chemical Calculations, Minerals. 11 (2021) 79. https://doi.org/10.3390/min11010079.

[103] J.F. Watts, J. Wolstenholme, An Introduction to Surface Analysis by XPS and AES, 2019. https://doi.org/10.1002/9781119417651.

[104] J.F. Moulder, W.F. Stickle, P.E. Sobol, K.D. Bomben, Handbook of X-ray Photoelectron Spectroscopy (XPS), 1991. https://doi.org/10.1002/0470014229.ch22.

[105] A. Oprea, N. Bârsan, U. Weimar, Work function changes in gas sensitive materials: Fundamentals and applications, Sens Actuators B Chem. 142 (2009) 470–493. https://doi.org/10.1016/j.snb.2009.06.043.

[106] M. Rohwerder, Passivity of Metals and the Kelvin Probe Technique, in: Encyclopedia of Interfacial Chemistry: Surface Science and Electrochemistry, Elsevier, 2018: pp. 414–422. https://doi.org/10.1016/B978-0-12-409547-2.13405-5.

[107] N. Barsan, J. Rebholz, U. Weimar, Conduction mechanism switch for SnO2 based sensors during operation in application relevant conditions; implications for modeling of sensing, Sens Actuators B Chem. 207 (2015) 455–459. https://doi.org/10.1016/j.snb.2014.10.016.

[108] J. Rebholz, U. Weimar, N. Barsan, Influence of Conduction Mechanism Changes on the Sensor Performance of SMOX Based Gas Sensors, Procedia Eng. 87 (2014) 20–23. https://doi.org/10.1016/j.proeng.2014.11.256.

[109] J. Rebholz, B. Junker, Kelvin Probe Measurement Experimental instruction, (2017).

[110] T. Russ, Z. Hu, B. Junker, H. Liu, U. Weimar, N. Barsan, Operando Investigation of the Aging Mechanism of Lead Sulfide Colloidal Quantum Dots in an Oxidizing Background, The Journal of Physical Chemistry C. 125 (2021) 19847–19857. https://doi.org/10.1021/acs.jpcc.1c04045.

[111] H. Jin, H. Zhou, Y. Zhang, Insight into the Mechanism of CO Oxidation on WO3(001) Surfaces for Gas Sensing: A DFT Study, Sensors (Switzerland). 17 (2017) 1898. https://doi.org/10.3390/s17081898.

[112] A. Staerz, M. Bahri, U. Geyik, H. Brinkmann, U. Weimar, O. Ersen, N. Barsan, Direct Microscopic Proof of the Fermi Level Pinning Gas-Sensing Mechanism: The Case of Platinum-Loaded WO3, Journal of Physical Chemistry Letters. 11 (2020) 166–171. https://doi.org/10.1021/acs.jpclett.9b03114.

[113] P.J. Larkin, Infrared and Raman Spectroscopy, 2nd ed., Elsevier Inc., 2018. https://doi.org/https://doi.org/10.1016/C2015-0-00806-1.

[114] N.B. Colthup, Infrared Spectroscopy, in: R.A. Meyers (Ed.), Encyclopedia of Physical Science and Technolog, 3rd ed., Elsevier Science Ltd., 2001: pp. 793–816. https://doi.org/10.1007/978-0-387-26308-3_40.

[115] A. Davydov, Molecular Spectroscopy of Oxide Catalyst Surfaces, John Wiley & Sons, Ltd., 2003.

[116] S. Roso, D. Degler, E. Llobet, N. Barsan, A. Urakawa, Temperature-Dependent NO2 Sensing Mechanisms over Indium Oxide, ACS Sens. 2 (2017) 1272–1277. https://doi.org/10.1021/acssensors.7b00504.

[117] M. Kantcheva, FT-IR spectroscopic investigation of the reactivity of NOx species adsorbed on Cu2+/ZrO2 and CuSo4/ZrO2 catalysts toward decane, Appl Catal B. 42 (2003) 89–109. https://doi.org/10.1016/S0926-3373(02)00218-7.

[118] D.S. Zingg, D.M. Hercules, Electron spectroscopy for chemical analysis studies of lead sulfide oxidation, Journal of Physical Chemistry. 82 (1978) 1992–1995. https://doi.org/10.1021/j100507a008.

[119] G.L.J. Trettenhahn, G.E. Nauer, A. Neckel, Vibrational spectroscopy on the PbO-PbSO4, and some related compounds; Part1. Fundamentals, infrared and Raman spectroscopy, Vib Spectrosc. 5 (1993) 85–100.

[120] D.J. Last, J.J. Nájera, R. Wamsley, G. Hilton, M. McGillen, C.J. Percival, A.B. Horn, Ozonolysis of organic compounds and mixtures in solution. Part I: Oleic, maleic, nonanoic and benzoic acids, Physical Chemistry Chemical Physics. 11 (2009) 1427–1440. https://doi.org/10.1039/b815425b.

[121] K. Jain, A. Siddam, A. Marathi, U. Roy, J.R. Falck, M. Balazy, The mechanism of oleic acid nitration by •NO2, Free Radic Biol Med. 45 (2008) 269–283. https://doi.org/10.1016/j.freeradbiomed.2008.04.015.

[122] S. Koppireddi, J.H. Seo, E.Y. Jeon, P.S. Chowdhury, H.Y. Jang, J.B. Park, Y.U. Kwon, Combined Biocatalytic and Chemical Transformations of Oleic Acid to ω-Hydroxynonanoic Acid and α,ω-Nonanedioic Acid, Adv Synth Catal. 358 (2016) 3084–3092. https://doi.org/10.1002/adsc.201600216.

[123] H.M. Hung, Y. Katrib, S.T. Martin, Products and Mechanisms of the Reaction of Oleic Acid with Ozone and Nitrate Radical, Journal of Physical Chemistry A. 109 (2005) 4517–4530. https://doi.org/10.1021/jp0500900.

[124] K. Laajalehto, R.S.C. Smart, J. Ralston, E. Suoninen, STM and XPS investigation of reaction of galena in air, Appl Surf Sci. 64 (1993) 29–39. https://doi.org/10.1016/0169-4332(93)90019-8.

[125] J.A. Taylor, D.L. Perry, An x-ray photoelectron and electron energy loss study of the oxidation of lead, Journal of Vacuum Science & Technology A. 2 (1984) 771–774. https://doi.org/10.1116/1.572569.

[126] P. Nowak, K. Laajalehto, On the interpretation of the XPS spectra of adsorbed layers of flotation collectors - ethyl xanthate on metallic lead, Physicochemical Problems of Mineral Processing. 41 (2007) 107–116.

[127] W.E. Morgan, J.R. Van Wazer, Binding energy shifts in the X-ray photoelectron spectra of a series of related group IV-a compounds, Journal of Physical Chemistry. 77 (1973) 964–969. https://doi.org/10.1021/j100626a023.

[128] J.A. Taylor, G.M. Lancaster, J.W. Rabalais, Chemical Reactions of N2+ Ion Beams with Group IV Elements and their oxides, J Electron Spectros Relat Phenomena. 13 (1978) 435–444.

[129] R.B. Shalvoy, G.B. Fisher, P.J. Stiles, Bond ionicity and structural stability of some average-valence-five materials studied by x-ray photoemission, Phys Rev B. 15 (1977) 1680–1697. https://doi.org/10.1103/PhysRevB.15.1680.

[130] L.R. Pederson, Two-dimensional chemical-state plot for lead using XPS, J Electron Spectros Relat Phenomena. 28 (1982) 203–209. https://doi.org/10.1016/0368-2048(82)85043-3.

[131] C. Cozza, V. Di Castro, G. Polzonetti, A.M. Marabini, An X-ray photoelectron spectroscopy (XPS) study of the interaction of mercapto-benzo-thiazole with cerussite, Int J Miner Process. 34 (1992) 23–32. https://doi.org/10.1016/0301-7516(92)90013-M.

[132] K.S. Kim, T.J. O'Leary, N. Winograd, X-Ray Photoelectron Spectra of Lead Oxides, Anal Chem. 45 (1973) 2214–2218. https://doi.org/10.1021/ac60335a009.

[133] J.Z. Fan, N.T. Andersen, M. Biondi, P. Todorovic, B. Sun, O. Ouellette, J. Abed, L.K. Sagar, M. Choi, S. Hoogland, , et al., Mixed Lead Halide Passivation of Quantum Dots, Advanced Materials. 31 (2019) 1904304. https://doi.org/10.1002/adma.201904304.

[134] H. Beygi, S.A. Sajjadi, A. Babakhani, J.F. Young, F.C.J.M. van Veggel, Surface chemistry of as-synthesized and air-oxidized PbS quantum dots, Appl Surf Sci. 457 (2018) 1–10. https://doi.org/10.1016/j.apsusc.2018.06.152.

[135] F.A. Miller, C.H. Wilkins, Infrared Spectra and Characteristic Frequencies of Inorganic Ions, Anal Chem. 24 (1952) 1253–1294. https://doi.org/10.1021/ac60068a007.

[136] H. Cao, G. Wang, S. Zhang, X. Zhang, Growth and photoluminescence properties of PbS nanocubes, Nanotechnology. 17 (2006) 3280–3287. https://doi.org/10.1088/0957-4484/17/13/034.

[137] G. FIZ Karlsruhe, Inorganic Crystal Structure Database, (n.d.). https://icsd.fiz-karlsruhe.de/search/basic.xhtml;jsessionid=7C2F6EACCEF2914EF031A6633CCC86D9 (accessed November 18, 2022).

[138] T. Russ, Z. Hu, L. Li, L. Zhou, H. Liu, U. Weimar, N. Barsan, In-operando Investigation of the Concentration Dependent NO2 sensing mechanism of Bi2S3 nanorods at Low Temperatures, ACS Sens. 7 (2022) 3023–3031.

[139] J.M. Rebholz, Influence of Conduction Mechanism Changes and Related Effects on the Sensing Performance of Metal Oxide Based Gas Sensors, Eberhard Karls University of Tübingen, 2016.

[140] J. Rebholz, P. Bonanati, U. Weimar, Grain shape influence on semiconducting metal oxide based gas sensor performance : modeling versus experiment, (2014) 3977–3983. https://doi.org/10.1007/s00216-013-7502-0.

[141] F. Schipani, A. Oprea, U. Weimar, A. Papadogianni, O. Bierwagen, Work Function Measurements in Single-Crystalline In2O3 for Conduction Modelling, Proc West Mark Ed Assoc Conf. 14 (2019) 54. https://doi.org/10.3390/proceedings2019014054.

[142] A. Gurlo, M. Sahm, A. Oprea, N. Barsan, U. Weimar, A p- to n-transition on alpha-Fe2O3 -based thick film sensors studied by conductance and work function change measurements, Sens Actuators B Chem. 102 (2004) 291–298. https://doi.org/10.1016/j.snb.2004.04.075.

[143] D. Degler, S. Wicker, U. Weimar, N. Barsan, Identifying the Active Oxygen Species in SnO2 Based Gas Sensing Materials: An Operando IR Spectrsocopy Study, The Journal of Physical Chemistry C. 119 (2015) 11792–11799. https://doi.org/10.1021/acs.jpcc.5b04082.

[144] D. Ayodhya, G. Veerabhadra, Microwave-assisted fabrication of g-C3N4 nanosheets sustained Bi2S3 heterojunction composites for the catalytic reduction of 4-nitrophenol, Environ Technol. 42 (2019) 826–841. https://doi.org/10.1080/09593330.2019.1646323.

[145] J. Cao, B. Xu, H. Lin, B. Luo, S. Chen, Novel heterostructured Bi2S3/BiOI photocatalyst: Facile preparation, characterization and visible light

photocatalytic performance, Dalton Transactions. 41 (2012) 11482–11490. https://doi.org/10.1039/c2dt30883e.

[146] J. Arumugam, A. Dhayal Raj, A.. Albert Irudayaraj, T. Pazhanivel, Temperature based investigation on structure and optical properties of Bi2S3 nanoflowers by slvothermal approach, Mechanics, Materials Science and Engineering. 9 (2017) 1–8. https://doi.org/10.2412/mmse.73.16.231.

[147] E. Fenelon, D.P. Bui, H.H. Tran, S.J. You, Y.F. Wang, T.M. Cao, V. Van Pham, Straightforward synthesis of SnO2/Bi2S3/BiOCl-Bi24O31Cl10 composites for drastically enhancing rhodamine b photocatalytic degradation under visible light, ACS Omega. 5 (2020) 20438–20449. https://doi.org/10.1021/acsomega.0c02461.

[148] P. Larkin, Chapter 2 - Basic Principles, in: J. Fedor, K. Morrissey, A.M. Clark, V. Bharath, G. Harris (Eds.), Infrared and Raman Spectroscopy, 2nd editio, Elsevier Inc., 2018: pp. 7–28. https://doi.org/10.1017/9781316677056.004.

[149] S. Mourdikoudis, L.M. Liz-Marzán, Oleylamine in nanoparticle synthesis, Chemistry of Materials. 25 (2013) 1465–1476. https://doi.org/10.1021/cm4000476.

[150] A.H. Hammad, M.A. Marzouk, H.A. ElBatal, The Effects of Bi2O3 on Optical, FTIR and Thermal Properties of SrO-B2O3 Glasses, Silicon. 8 (2016) 123–131. https://doi.org/10.1007/s12633-015-9283-x.

[151] A. Barbe, S. Mikhailenko, E. Starikova, V. Tyuterev, High Resolution Infrared Spectroscopy in Support of Ozone Atmospheric Monitoring and Validation of the Potential Energy Function, Molecules. 27 (2022) 911. https://doi.org/10.3390/molecules27030911.

[152] F. Maugé, J. Lamotte, N.S. Nesterenko, O. Manoilova, A.A. Tsyganenko, FT-IR study of surface properties of unsupported MoS2, Catal Today. 70 (2001) 271–284.

[153] K.M. Bulanin, J.C. Lavalley, A.A. Tsyganenko, IR spectra of adsorbed ozone, Colloids Surf A Physicochem Eng Asp. 101 (1995) 153–158.

[154] J.-M. Flaud, C. Camy-Peyret, C.P. Rinsland, M.A.H. Smith, Line Parameters for 16O3 Bands in the 7-µm Region, J Mol Spectrosc. 134 (1989) 106–112.

9. Publications

Articles in peer reviewed journals as first author:

- T. Russ et al., In-Operando Investigation of the Concentration Dependent NO_2 Sensing Mechanism of Bi_2S_3 Nanorods at Low Temperatures and the Interference of O_3, *ACS Sensors*, **2022**, 7, 3023 – 3031.
- T. Russ et al., Operando Investigation of the Aging Mechanism of Lead Sulfide Colloidal Quantum Dots in an Oxidizing Background, *Journal of Physical Chemistry C*, **2021**, 125, 36, 19847 – 19857.

Articles in peer reviewed journals as co-author:

- K. Raimayan et al., Electrochemical Sensors for the Hydrogen Economy, *ECS Sensors Plus*, **2023**, 2, 045601.
- M. Amati et al., Near ambient pressure photoelectron spectro-microscopy: from gas-solid interface to operando devices, *Journal of Physics D Applied Physics*, **2021**, 54, 204004.
- A. Staerz et al., Thermal Water Splitting on the WO_3 Surface: Experimental Proof, *ACS Applied Electronic Materials*, **2020**, 2, 10, 3254 – 3262.
- A. Staerz et al., Understanding the Sensing Mechanism of WO_3 based Gas Sensors, *2019 IEEE International Symposium on Olfaction and Electronic Nose (ISOEN)*, **2019**, 13972306.
- A. Staerz et al., WO_3 Based Gas Sensors, *Proceedings*, **2018**, 2, 13, 826.
- A. Ulfkjær et al., A gold-nanoparticle stoppered [2]rotaxane, *Nanoscale*, **2018**, 10, 9133 – 9140.
- A. Staerz et al., The Oxidizing Effect of Humidity on WO_3 based Sensors, *Sensors and Actuators B*, **2016**, 237, 54 – 58.

Book Chapters:

- T. Russ et al., Chapter 7 - Fabrication of metal oxide heterostructures for the application in chemo resistive gas sensors, *Metal oxide-based heterostructures*, **2023**, 1st edition, editors Naveen Kumar, Bernabe Soucase, Elsevier.

Poster Presentations at Conferences:

- J.R. Stetter et al., Electrochemical Sensors for Impact Monitoring of Wildfire Smoke on Air Quality, *Sensor and Measurement Science International*, **2023**, Nürnberg, Germany.
- D. Rentsch et al., Nachweis von Cyanid im Blut mittels GC-MS nach Derivatisierung mit Phthalaldehyd und 1-Adamantylamin und Verwendung von $^{13}C^{15}N^-$ als internen Standard, *95. Jahrestagung der Deutschen Gesellschaft für Rechtsmedizin*, **2016**, Heidelberg, Germany.

Presentations at Conferences:

- T. Russ et al., RTILs as Electrolytes in Electrochemical Gas Sensors for O_2 and Other Gases, *ECS Spring*, **2023**, Boston, MA, USA.
- T. Russ et al., Hydrogen Sensors for Energy Applications, *Sensor and Measurement Science International*, **2023**, Nürnberg, Germany.
- T. Russ et al., Low-Cost Air Quality (AQ) Sensors for Monitoring Wildfire Emissions to Protect Communities, *ACS Spring*, **2023**, Indianapolis, IN, USA.